Classe di Scienze

Tesi di Perfezionamento in Fisica

Closing the Window on WIMP Dark Matter

Candidato:
Salvatore Bottaro

Relatore:
Prof. Roberto Contino

Relatore interno:
Prof. Enrico Trincherini

Anno Accademico 2021/2022

Contents

Chapter 1

Introduction

1.1 The theoretical motivation of WIMP DM

The mystery of the nature of Dark Matter (DM) is one of the longest standing problems in physics and cosmology nowadays. Since the measure of velocity dispersion of galaxies in the Coma cluster by Zwicky in 1933, the indirect evidence of the existence of DM has piled up. Observations, ranging from the velocity curves of galaxies to the Cosmic Microwave Background (CMB) and structure formation, are all compatible with the existence of a new, non-baryonic, cold (*i.e.* non-relativistic at matter radiation equality), electrically neutral component of matter, which makes up $\approx 27\%$ of the energy density budget of the Universe. However, besides the remarkable observation of the galaxy cluster merging known as "Bullet Cluster", which showed that DM must be basically collisionless, so far we have no insight on the DM dynamics, nor constraints on its mass, which can range over 80 orders of magnitude. This spectacular indeterminacy has triggered over the years an intense research program, both theoretical and experimental.

Among the plethora of DM models that have been proposed so far, the so-called Weakly Interacting Massive Particles (WIMP) paradigm stands out because of its both theoretical and phenomenological appeal. The attractiveness of the WIMP scenario mostly relies on its simplicity and predictivity and, historically, also to its connection to the hierarchy problem in the Standard Model (SM). The basic ingredient in the WIMP paradigm is the existence of a cosmologically stable new particle, which plays the role of DM, with strong enough interactions with the SM in order to enforce thermal equilibrium at some large temperature in the early Universe. In particular, WIMP can be produced by the SM thermal bath and then annihilate back into SM particles. The balance between these two processes sets the DM abundance whose evolution is described by the Boltzmann equation:

$$z\frac{\mathrm{d}Y}{\mathrm{d}z} = \frac{s\langle\sigma v_{\mathrm{rel}}\rangle}{H}\left(\frac{Y^2}{Y_{\mathrm{eq}}^2} - 1\right), \tag{1.1}$$

where $Y = n_{\mathrm{DM}}/s$ is the DM yield, defined as the DM number density n_{DM} divided

by the entropy density s, H is the Hubble parameter, $\langle\sigma v_{\rm rel}\rangle$ the thermally averaged annihilation cross-section of DM into SM, and $z = M/T$ with M the DM mass and T the temperature. When the annihilation rate $\Gamma = n^{\rm eq}_{\rm DM}\langle\sigma v_{\rm rel}\rangle > H$, the DM is in chemical equilibrium with the thermal bath and $Y = Y_{\rm eq}$. When, instead, $\Gamma < H$, which occurs roughly for $z = z_{\rm f.o.} \approx 25 - 30$, the DM yield freezes out and $Y = Y_{\rm f.o.}$=const. The yield at freeze-out determines the DM present-day abundance $\Omega_{\rm DM}h^2 \equiv M n_{\rm DM}/\rho_0$, where $\rho_0 = 3H_0^2/8\pi G$ is the critical energy density and H_0 the Hubble constant today, and can be estimated as:

$$\Omega_{\rm DM}h^2 \simeq 0.12 \left(\frac{z_{\rm f.o.}}{25}\right) \frac{(23\ \ {\rm TeV})^2}{\langle\sigma v_{\rm rel}\rangle}, \tag{1.2}$$

which must be compared with the abundance measured by Planck $\Omega_{\rm DM}h^2 = 0.11933 \pm 0.00091$ [1]. This relation between $\Omega_{\rm DM}$ and $\langle\sigma v_{\rm rel}\rangle$ is what made WIMP historically one of the most compelling DM paradigms. Indeed, it was realized that if the DM interacts with the SM with a strength of order of the Electro-Weak (EW) interactions, with a cross-section scaling as $\langle\sigma v_{\rm rel}\rangle \sim g^4/M^2$, the correct DM abundance is reproduced if $M \approx \mathcal{O}(100)$ GeV. This observation, since it predicts new physics at the EW scale which could explain DM and at the same time solve the hierarchy problem in the SM, was dubbed "the WIMP miracle".

Conversely, many WIMP DM candidates emerged within models originally introduced to solve the hierarchy problem. For example, in Little Higgs models [2–9] the hierarchy problem is solved by assuming the Higgs to be a Goldstone boson of a global symmetry spontaneously broken at some UV scale. The partial gauging of the global symmetry makes the Higgs a pseudo-Goldstone boson, whose mass however arises only at two-loop level. This allows the Higgs mass to be radiatively stable up to the cutoff of the model, around 10 TeV. The introduction of an additional discrete symmetry acting on all fields but the SM model ones, the so-called *T-parity* [10–12], ensures the stability of the lightest partner of the Higgs boson, which then plays the role of DM. Similarly, supersymmetric (SUSY) extensions of the SM have also been proposed as a solution to the hierarchy problem. In this framework, the neutral superpartners of the Higgs and EW gauge bosons, the higgsino and the gauginos, typically decay fast into SM particles. However, assuming an additional discrete symmetry acting on the superpartners, the *R-parity*, makes the lightest supersymmetric particle (LSP) or neutralino, coming from a combination of the EW gauginos and higgsino, stable and thus a viable DM candidate [13–15].
The list of models postulating a WIMP DM candidate in connection to the hierarchy problem is much longer and includes other theoretically successful paradigms, like extra-dimensions [16, 17] or Twin-Higgs models [18–22]. In all these proposals, the abundance of DM, whose stability is usually enforced by some symmetry put by hand, is set by freeze-out and leads to a DM mass in the TeV ballpark. This prediction was particularly compelling at the time when these models were proposed, since it was in the discovery reach of the LHC.
In summary, the simplicity of the cosmological evolution, the incidental link to the hierarchy problem and the existence of many compelling frameworks realizing it, as

well as the possibility of being tested at experimental facilities like the LHC, represent the main reasons for the early (theoretical) success of the WIMP paradigm.

1.2 Minimal DM and Beyond.

At present, however, despite the heavy experimental effort, no evidence of new physics at the TeV scale has been found at current colliders, nor at any other DM experiment. As a consequence, many models seeking to link DM and the hierarchy problem, like the simplest realizations of SUSY, have been heavily constrained, if not ruled out, or require large fine tunings to be viable. An alternative and more minimalistic approach to DM would be to abandon the hierarchy problem as a guiding principle and retain the good properties of the WIMP paradigm by looking for the most minimal extension of the SM with a viable WIMP DM candidate. This approach was realized in [23–25] with the so-called Minimal DM (MDM) models where the SM is increased with a single multiplet χ, which can be either scalar or fermionic, with hypercharge Y satisfying the following requests:

- the lightest component of the multiplet must be electrically neutral and without strong interactions;
- the only renormalizable interactions of χ with the SM are gauge interactions;
- not excluded by current experiments;
- DM stable on cosmological scales;
- no sub-Planckian Landau poles.

The first condition implies that the DM must be embedded in an EW n-plet. Besides, DM neutrality requires that one component of the n-plet satisfies $Q = T_3 + Y = 0$, where $T_3 = \text{diag}\left(\frac{n+1}{2} - i\right)$, with $i = 1, \ldots, n$, is the diagonal generator of $\text{SU}(2)_L$. At this level, we can distinguish between two classes of EW multiplets: i) real EW representations with $Y = 0$ and odd n; ii) complex EW representations with arbitrary n and $Y = \pm\left(\frac{n+1}{2} - i\right)$ for $i = 1, \ldots, n$. Because of the large EW annihilation cross-section, DM is in chemical equilibrium at large temperatures and its present day abundance is set by its density at freeze-out. This implies that the only free parameter left in MDM models, the DM mass, can be determined from gauge interactions alone, making this framework very predictive. Finally, despite the apparently large number of possibilities, there is only one candidate satisfying the last two MDM conditions: the Majorana 5-plet with $Y = 0$ with mass $M_\chi \approx 14$ TeV [26]. Larger multiplets lead to sub-Planckian Landau poles, while for smaller ones and for all the scalar candidates DM decays too fast into SM [27]. In fact, conversely to the models mentioned in the previous Section, the DM candidate corresponding to the Majorana 5-plet is accidentally stable up to the Planck scale.

The last two MDM conditions turn out to be the most stringent ones and other interesting and theoretically motivated multiplets can in principle be considered by relaxing them, like the fermionic 2-plet with $Y = 1/2$ (higgsino) or 3-plet with $Y = 0$

(wino), both present in SUSY, and their scalar counterparts [25]. Such conditions implicitly assume than no UV physics exists that could ameliorate the UV behavior of the MDM model, either by enforcing DM stability or improving the gauge coupling perturbativity. For this reason, in this Thesis we decided to go beyond the MDM approach by further minimizing the theory assumptions. In practice, we replace the last two MDM conditions with the less stringent requirement of the perturbative unitarity of each partial wave of the total annihilation cross-section [28], which we re-analyze here for EW n-plets. This condition selects the models for which more robust predictions on the DM mass and phenomenology can be made. Issues like DM stability or gauge coupling perturbativity, which, with the notable exception of the Majorana 5-plet, are in general present, are assumed to be solved by some unknown UV dynamics and with respect to which we remain agnostics.

Over the years, phenomenological signatures of MDM as well as of more general EW WIMP multiplets at LHC [27, 29, 30] and in direct (DD) [31–33] and indirect (ID) [34, 35] detection experiments have been extensively studied. At the same time, a better understanding of the freeze-out dynamics has been achieved, in particular with the inclusion non-perturbative effects like bound state formation (BSF) which can heavily affect the prediction of the DM mass [26, 36, 37]. Despite such wide and intense activity on the subject, a systematic study of the EW WIMP paradigm is still lacking and no clear definition of the landscape of the viable EW WIMP parameter space is available. The first main goal of this Thesis is precisely to fill this gap and fully classify all the *calculable* EW WIMP. The motivation behind this endeavour is not only theoretical, albeit important on its own, but also phenomenological. In fact, within the EW WIMP framework we find that the range of DM masses goes from ≈ 1 TeV to hundreds of TeV, so that the EW WIMP candidates are still out of reach of present experiments and thus not excluded. First of all, DD constraints are automatically evaded by real candidates due to the naturally vanishing coupling to the Z-boson, while complex multiplets with non-zero hypercharge require a minimal deformation of the renormalizable Lagrangian. Finally, their production at the LHC is kinematically closed or at least highly suppressed. Such scenario, however, may change in the future, thanks to the forthcoming progress in collider physics and DM detection experiments. In particular: *i*) suggestions have been put forward for a very high energy lepton colliders that could reach up to 30 TeV center of mass energy [38, 39]; *ii*) next generation direct detection experiments like DARWIN [40, 41] can reach hundreds of tons/year of exposure ; *iii*) high-energy γ-ray telescopes like CTA [42–45] are designed to observe gamma-rays of tens of TeV. EW WIMP represent the ideal target for all these future experiments and it is therefore crucial to determine which multiplets can be actually probed. This is the second and most important goal of this Thesis. In the rest of the Chapter we will describe in greater detail the current experimental status as well as the expected improvement brought by future experiments to DM searches.

1.3 EW WIMP at Future Experiments

1.3.1 Direct Detection

The idea of directly detecting DM from the galactic halo by its scattering on target nuclei dates back to the 80' [46–49]. The search for WIMP, in particular, has been the main motivation for current liquid Xenon experiments. Liquid noble gases, in fact, are particularly clean environments where radiation emitted by recoiled nuclei hit by DM can be detected. The typical detector employed today consists in a dual-phase xenon time projection chambers (TPC), formed by a layer of gaseous xenon on top of a tank of several tons of liquid xenon, as shown in Figure 1.1. Any recoiling event produces both scintillation photons as well as free electrons in the liquid. The photons (S1) are immediately detected by photon sensors located on the top and at the bottom of the chamber, while the slower electrons are drifted by an electric field towards the gaseous layer, where they produce additional scintillations (S2). The time delay between the signals S1 and S2 allows for a 3D reconstruction of the event, which is relevant for background suppression.

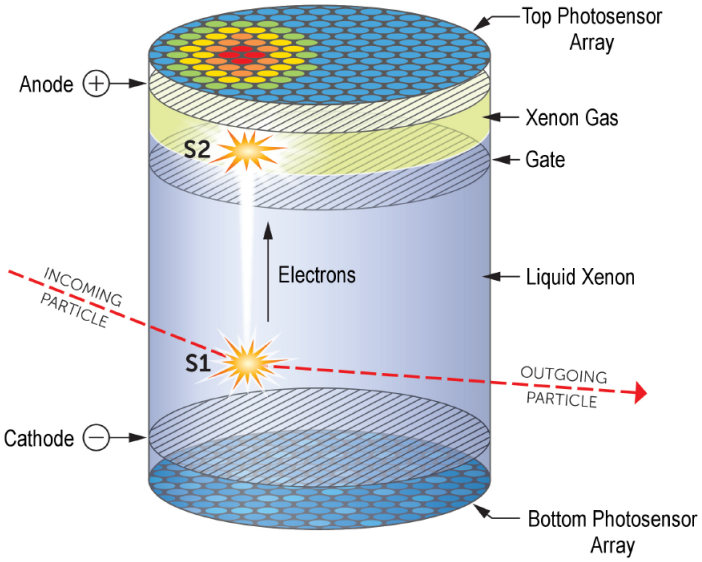

Figure 1.1: *Schematic representation of a dual-phase projection chamber (TPC) [50].*

Since ZEPLIN-II [51], the first experiment based on a TPC, the evolution of liquid xenon experiments progressed through successively larger, cleaner, and thus more sensitive detectors. Up to today, no recoil event signal has been detected, so that DD experiments only provide upper limit on the scattering cross-section of DM on nuclei. The most severe bounds are currently provided by XENON1T [52] and PandaX-4T [53]. The up-coming LZ [54] and XENONnT [55] experiments, instead, are expected to improve these bounds by one order of magnitude thanks to their larger exposure. Finally, next-generation detectors like DARWIN [41] and DARWIN/G3 [50], with a further increase of exposure, should be able to make a decisive step further in sensitivity and close the window above the neutrino floor [56], as can be seen in Figure 1.2 for the spin-independent (SI) cross-section (σ_{SI}).

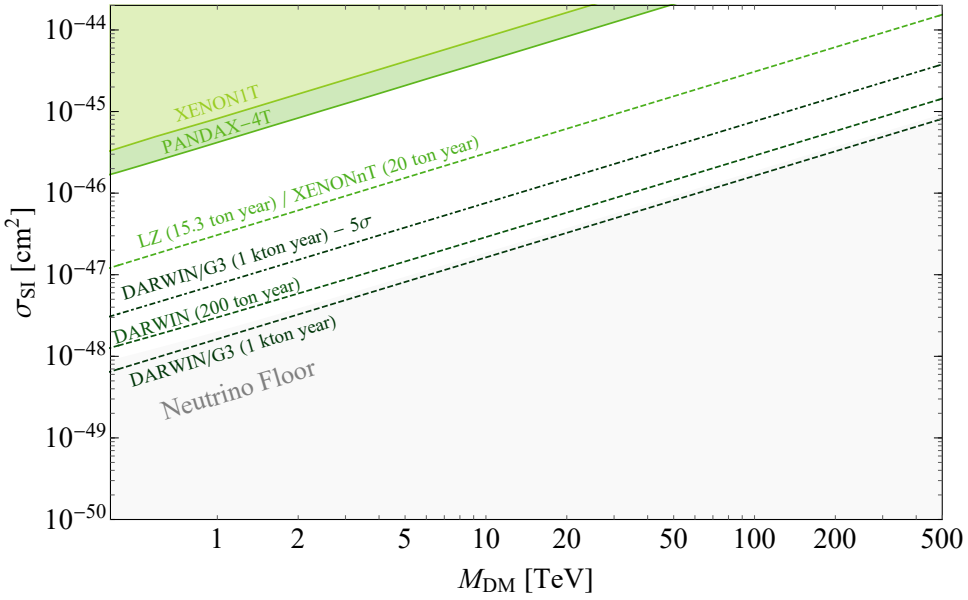

Figure 1.2: *The* **light green** *shaded region is excluded by the present experimental constraints from XENON-1T [52] and PandaX-4T [53], the* **green dashed** *lines shows the expected 95% CL reach of LZ/Xenon-nT [54, 55] and DARWIN [41, 50]. The light gray region show the neutrino floor for 200 ton/year exposure derived in Ref. [56].*

The DARWIN and DARWIN/G3 experiments are particularly relevant for the EW WIMP introduced here. In fact, as we shall discuss in Chapters 2 and 3, the SI independent cross-section scales like $\sigma_{\rm SI} \approx 10^{-47}(n/2)^4$ cm^2, while the projected bound from DARWIN/G3 scales like $\sigma_{\rm SI} \approx 10^{-48}(M/1\text{ TeV})^4$ cm^2 $\approx 10^{-48}(n/2)^{5/2}$ cm^2, where the last equality approximately holds for thermal masses. The simple estimates above show that next-generation will be in the position to detect signals from EW WIMP or otherwise exclude them. This represents the main message from the DD analysis of this Thesis.

1.3.2 Muon Collider

Despite the great success with the discovery of the Higgs boson in 2012, the LHC has so far failed to answer some of the most urgent questions still pending within the SM and beyond, like the mechanism of the Electroweak Symmetry Breaking (EWSB), baryon asymmetry in the Universe or the nature of DM. The need to shed light on these issues is paving the way to the future era of collider physics, which is currently under scrutiny by the collider physics community. The first step in this direction is represented by the high-luminosity upgrade of LHC (HL-LHC) [57], which is under construction and scheduled to deliver collisions at a center-of-mass (COM) energy $\sqrt{s} = 14$ TeV and luminosity larger than a factor 5-7 with respect to LHC by 2027. There is still debate, instead, on which kind of machine the next, brand-new collider should be. Current projects involve both new e^+e^- and pp colliders. The advantage of a lepton machine, heavily exploited by LEP, relies on the elementary nature of electrons, which allows for collision events where the COM energy is known precisely. On the contrary, electrons are notoriously difficult to accelerate and it is difficult to

reach large energies. Current proposals are represented by the circular accelerators FCC-ee [58] at CERN and CEPC [59] in China and the linear CLIC [60, 61] at CERN and ILC [62, 63] in Japan. Instead, pp machines have opposite pros and cons with respect to electrons: being heavier than electrons, protons can be accelerated to way higher energies, while their composite nature forbids a precise determination of the COM energy of the collision, occurring at the parton level. The pp machine so far proposed would reuse the tunnels built for pre-existing e^+e^- machines, like FCC-hh [64] (from FCC-ee) or SppC [59] from CEPC.

A third option currently on the table is represented by a muon collider, which would retain the benefits of both e^+e^- and pp collides. In fact, the energy loss due to synchroton radiation by muons, which are 200 times heavier than electrons, is a factor 100 million less then that lost to produce an e^+e^- collision at the same energy. Besides, like electrons, muons are elementary particles and the COM energy of the beam is entirely available in the collision, so that a muon collider with a given COM energy is equivalent with a way more energetic pp collider. This last statement is made quantitative in Figure 1.3, which displays the COM energy $\sqrt{s_p}$ that a proton collider must possess to be "equivalent" to a muon collider of a given energy $\sqrt{s_\mu}$. Equivalence is defined [38, 65, 66] in terms of the pair production cross-section for heavy particles, with mass close to the muon collider kinematical threshold of $\sqrt{s_\mu}/2$. As we can see, a $\sqrt{s_\mu} = 14$ TeV would be sufficient to perform like a 100 TeV pp collider.

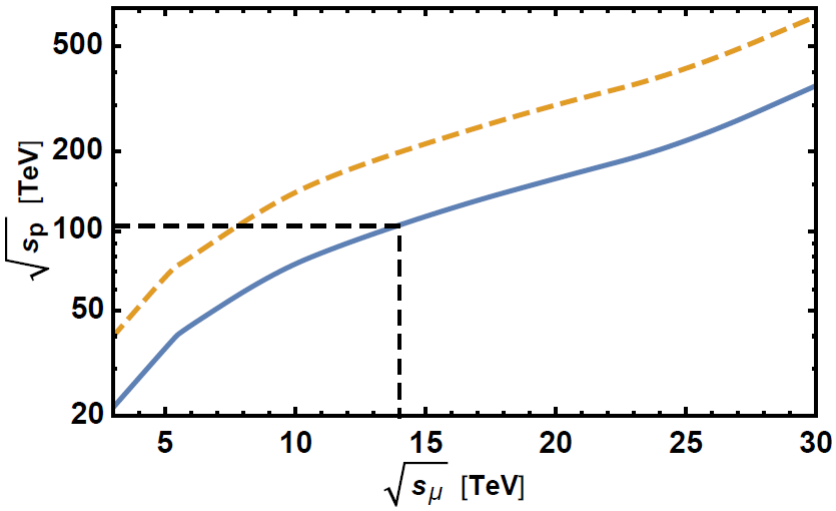

Figure 1.3: *Equivalent proton collider energy under the assumption that qq and gg partonic initial states both contribute to the production [67]*

Hence, a muon collider offers the unique possibility of combining high energy with precision measurements. In addition to this, it would be the perfect environment to study current tensions related to muons, like the $(g-2)$ and lepton-flavor universality anomalies. But, most importantly, it would also be the most suitable machine to hunt for the EW WIMPs, due to its large COM energy, relatively clean collision environment, and the capability of pair producing weakly interacting particles up to

kinematical threshold. This is evident from Figure 1.4, where the expected 2σ and 5σ discovery reach for two of the most motivated EW WIMP candidates, the Higgsino and the Wino, are compared among the different colliders. Consistently with Figure 1.3, a 10 TeV muon collider would be sufficient to discover these candidates, while FCC-hh running at 100 TeV is barely enough.

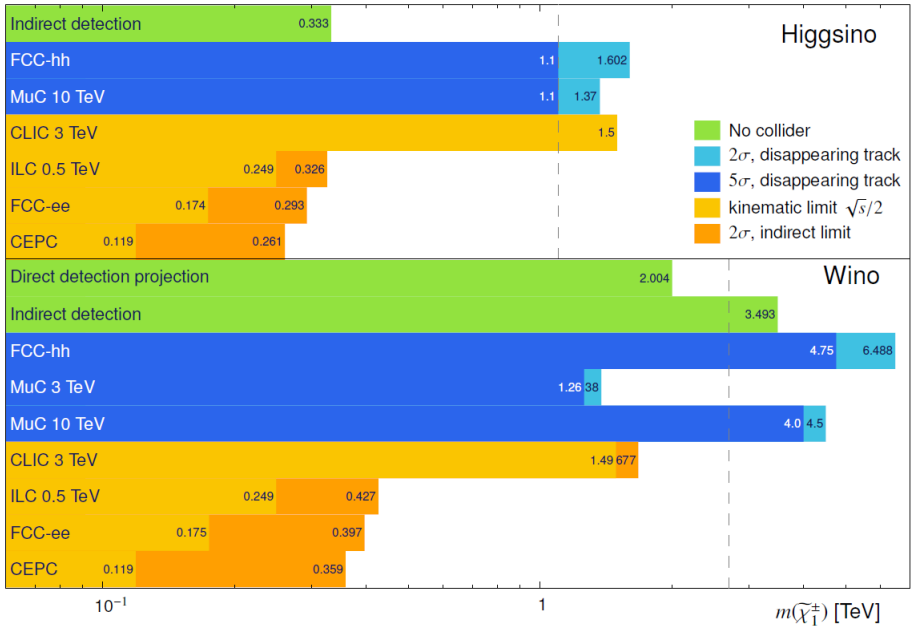

Figure 1.4: *Exclusion and discovery mass reach on Higgsino and Wino Dark Matter candidates at muon colliders from disappearing tracks, and at other facilities [67, 68]. In this Thesis, we shall revisit the muon collider reaches for both candidates.*

EW WIMP can be studied at muon colliders in several channels. In Chapters 2 and 3 we shall study in detail mono-X searches (such as monophoton and mono-W), where a pair of WIMP is produced in association with a SM state X, which is then detected, and disappearing tracks produced by a charged particle in the WIMP multiplet before it decays to DM. Additionally, in Chapter 2 we shall also investigate the possibility of resonantly producing WIMP bound states which later annihilate into SM. With a muon collider of the proper energy, bound state production would be the dominant discovery channel.

1.3.3 Indirect Detection

The last fundamental strategy for DM searches is Indirect Detection (ID), that is the detection of gamma-rays from annihilation products of DM particles from galactic or extra-galactic sources. The typical gamma-ray spectrum is characterized at very high energy by lines, peaking at the DM mass $E_\gamma \simeq M_{\rm DM}$, from the loop-induced annihilations into $\gamma\gamma$ and γZ and a continuum from the showering, hadronization and decays of the electroweak gauge bosons [69].

Since the EW WIMP masses range from 1 to hundreds of TeV, a significant fraction of the gamma-ray spectrum is characterized by very high-energy (VHE) photons (i.e.

$E_\gamma \gtrsim 100$ GeV), for which the sensitivities of space-based telescopes like PAMELA [70], AMS-02 [71] and Fermi [72] are limited by their size. Instead, working and upcoming ground-based Cherenkov telescopes are in a very good position to probe heavy EW WIMP thanks to their large effective areas. Indeed, they are specifically designed to detect VHE gamma-rays coming from different astrophysical objects and are therefore best suited for signals from the annihilation of EW n-plets. Currently H.E.S.S. [73], MAGIC [74] and VERITAS [75] telescopes are operating. However, their performances are expected to be outclassed by the CTA, whose data-taking is scheduled to start in 2025.

The two best studied astrophysical targets are the Galactic Center (GC) [42, 76] and the Milky Way's dwarf Spheroidal galaxies (dSphs) [42]. Concerning the GC, projected sensitivities show that CTA will improve bounds on DM annihilation cross-section by one order of magnitude with respect to H.E.S.S. for DM masses in the range $\approx 0.5 - 20$ TeV. Besides, CTA will provide bounds on DM masses up to 300 TeV, which is close to the boundary set by the perturbative unitarity on the mass of EW WIMP. But, most importantly, CTA will for the first time take data from recently discovered dSphs like Draco or Triangulum. In fact, dSphs stand out as very clean environments to search for high energy γ-lines only residually affected by systematics related to the determination of their astrophysical parameters in the presence of limited stellar tracers [77, 78]. On the contrary, in the GC, the uncertainties are dominated by the importance of the baryonic physics in the inner most region of the Milky Way which comes together with the poor knowledge of the DM distribution at the center of the Milky Way [79–82]. In fact, assuming different plausible density profile like the so-called NFW and Einasto profile can change the bounds on the DM annihilation cross-section by two orders of magnitude.
In this Thesis, we shall discuss ID prospects from CTA only in Chapter 2 and leave a more detailed analysis of ID constraints for a future work. In fact, the shape of the spectrum and, especially, the intensity of the peak at the DM mass strongly depend on the DM mass, which must be determined precisely. However, since large multiplets have large $\mathrm{SU}(2)_L$ charges and thus stronger interactions, next-to-leading order (NLO) corrections (*e.g.* loop corrections) introduce too large uncertainties in the computation of the DM mass as well as of the annihilation cross-section. Despite this, due to the large potential of future ID searches, particularly in the large mass regime, it is important to push the theoretical prediction to a greater precision. This goes beyond the scope of this Thesis.

This Thesis is structured in two parts. In Chapter 2, based on [83, 84], we classify and discuss the phenomenology, including prospects from future experiment, of real EW WIMP candidates. In Chapter 3, based on [85] we extend the analysis to Complex EW WIMP, highlighting the differences with respect to the real case, mainly due to the introduction of UV generated mass splittings. Finally, in Chapter 4 we summarize the conclusions of the Thesis.

Chapter 2

The Real EW WIMP Window

In this Chapter, we take a first step in our systematic classification of EW WIMP by considering *real* EW representations. We first determine the freeze-out predictions and then assess if and how the future experimental program will be able to fully test this scenario. We assume the DM to be the lightest neutral component of one fermionic or scalar n-plet of SU(2) with odd n and zero hypercharge. This choice of quantum numbers automatically avoid strong constraints from direct detection searches because the DM does not couple to the Z-boson at tree level, and will be taken here as a minimal realization of the EW WIMP scenario.
The lightest particle in any such representation can be made stable by enforcing a symmetry acting on the DM only. For multiplets with $n \geq 5$ such a symmetry arises accidentally in the renormalizable Lagrangian. However, we shall see that DM stability for $n > 5$ requires additional assumptions about the UV completion of the theory.

For any given n-plet, computing the EW annihilation cross-section in the early Universe allows to infer the WIMP cosmological abundance. By requiring it to match the measured value of the DM abundance today, $\Omega_{\rm DM}h^2 = 0.11933 \pm 0.00091$ [1], the mass of the n-plet can be univocally determined. In contrast to previous papers on the subject [23–25, 86], our approach here is to minimize the theory assumptions and fully classify the *calculable* freeze-out predictions. Because of its infrared-dominated nature, the calculability of freeze-out depends purely on the partial wave unitarity of the total annihilation cross-section [28]. All in all, demanding perturbative unitarity requires $n \leq 13$ for both bosonic and fermionic DM. Stronger constraints on n can be imposed by demanding the EW interactions to remain perturbative up to scales well above the thermal DM mass.

The effects of Sommerfeld enhancement (SE) and of bound state formation (BSF) are known to significantly affect the freeze-out predictions and need to be included. The first effect has long been recognized to lead to an enhancement of the annihilation cross-section at small relative velocities [87–90]. The effects of BSF for WIMP freeze-out have been first computed in Ref. [26] for the $n = 5$ fermionic multiplet (see Ref.s [37, 91] for earlier computations in other contexts). Here we extend their treatment to fermionic and scalar representations of arbitrary high n, up to the

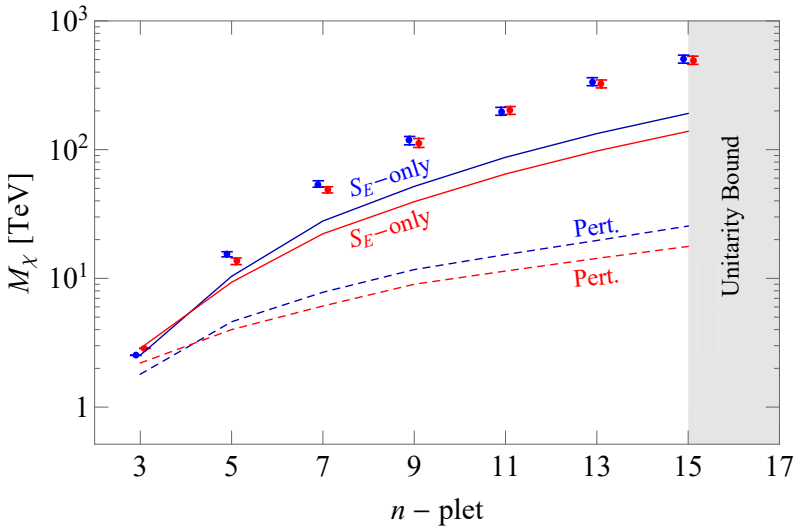

Figure 2.1: *Summary of the thermal masses for Majorana fermion (red) and real scalar WIMPs (blue) including both Sommerfeld enhancement (SE) and bound state formation (BSF). The solid lines are the thermal masses with SE. The dashed lines are the thermal masses for the hard annhilation cross-section. The gray shaded region is excluded by s-wave perturbative unitarity including BSF.*

break-down of perturbative unitarity. At growing n, we find that bound states (BS) are more tightly bound, with their ionization rate being exponentially suppressed. At the same time, the multiplicity of accessible BS channels grows significantly.

The freeze-out mass predictions are summarized in Table 2.1 and Fig. 2.1 for the real n-plets considered here. With masses ranging from several TeV to tens or hundreds of TeV, most of the EW WIMP candidates are still out of reach of present experiments, but could be tested in the future, thanks to the forthcoming progress in collider physics and DM detection experiments, as outlined in Chapter 1. With the mass predictions at hand, we thus perform a systematic survey of the WIMP phenomenology. We first examine the reach of a hypothetical future muon collider, studying in detail for which values of center-of-mass energy and integrated luminosity the EW 3-plets and 5-plets can be fully probed through direct production. We instead find direct production of the EW multiplets with $n > 5$ to be beyond the reach of any realistic future machine (this is in contrast with the results of the recent study [92] due to the increase of the thermal mass of the 7-plet with the inclusion of BSF effects). These larger n-plets are possibly within the reach of large exposure direct detection experiments, and will probably be tested more easily with future high energy γ-ray telescopes. A careful study of the expected signals in indirect detection is left for a future work [93].

This Chapter is organized as follows. In Sec. 2.1 we summarize the real EW WIMP paradigm, in Sec. 2.2 we illustrate the main features of our freeze-out computation, and in Sec. 2.3 we discuss the unitarity bound assessing the theory uncertainties. These three sections provide a full explanation on the results of Table 2.1 and Fig. 2.1. In Sec. 2.4 we discuss the implications of our study for a future muon col-

DM spin	n_Y	M_χ (TeV)	$(\sigma v)^{J=0}_{\rm tot}/(\sigma v)^{J=0}_{\rm max}$	$\Lambda_{\rm Landau}/M_{\rm DM}$	$\Lambda_{\rm UV}/M_{\rm DM}$
Real scalar	3	2.53 ± 0.01	–	2.4×10^{37}	4×10^{24}*
	5	15.4 ± 0.7	0.002	7×10^{36}	3×10^{24}
	7	54.2 ± 3.1	0.022	7.8×10^{16}	2×10^{24}
	9	117.8 ± 8.8	0.088	3×10^{4}	2×10^{24}
	11	199 ± 14	0.25	62	1×10^{24}
	13	338 ± 24	0.6	7.2	2×10^{24}
Majorana fermion	3	2.86 ± 0.01	–	2.4×10^{37}	2×10^{12}*
	5	13.6 ± 0.8	0.003	5.5×10^{17}	3×10^{12}
	7	48.8 ± 2.7	0.019	1.2×10^{4}	1×10^{8}
	9	113 ± 9	0.07	41	1×10^{8}
	11	202 ± 14	0.2	6	1×10^{8}
	13	324.6 ± 23	0.5	2.6	1×10^{8}

Table 2.1: *Freeze-out mass predictions for WIMP DM in real EW multiplets with $Y = 0$. The annihilation cross-section includes both the contribution of SE and BSF. We provide a measure of how close the DM annihilation cross-section is to the unitarity bound for s-wave annihilation $(\sigma v)^{J=0}_{max} = 4\pi/M^2_{DM} v$. Approaching the unitarity bound, the error on the WIMP mass grows proportionally to the enhancement of the next-to-leading order (NLO) contributions estimated in Eq. (2.24). We derive the scale where EW gauge coupling will develop a Landau pole by integrating-in the WIMP multiplet at its freeze-out mass. The stability of both scalar and fermionic DM can always be enforced by requiring a $\mathbb{Z}_2$ symmetry in the DM sector to forbid DM decays. This symmetry forbids the scalar and fermionic 3-plets decay at renormalizable level as indicated by the *. The value of the UV cut-off Λ_{UV} gives an idea of the required* quality *for this symmetry to make DM stable and avoid stringent bounds on decaying DM ($\tau_{DM} > 10^{28} sec$) [94]: a new physics scale lower than Λ_{UV} would require a $\mathbb{Z}_2$ to explain DM stability, while a cut-off higher than Λ_{UV} would make DM stability purely accidental.*

lider, focusing on the fermionic case, while leaving the results and comments on the scalar case to Appendix F. In Sec. 2.5 we briefly re-examine the reach of direct and indirect detection experiments in light of our findings. In Appendix A we discuss the nature of next-to-leading order corrections while in Appendix B we detail the BS dynamics for the 7-plet. In Appendix C we provide further details on the direct production of bound states at future colliders.

2.1 Which Real WIMP?

We summarize here the logic of our WIMP classification very much inspired by previous papers on the subject [23–25, 35, 86] and applied to the real WIMP case.

We take the DM to be the neutral component of an EW n-plet with odd n and $Y = 0$,

so that at the renormalizable level it is described by the following Lagrangians:

$$\mathscr{L}_{\rm s} = \frac{1}{2}\left(D_\mu \chi\right)^2 - \frac{1}{2}M_\chi^2 \chi^2 - \frac{\lambda_H}{2}\chi^2|H|^2 - \frac{\lambda_\chi}{4}\chi^4\,, \tag{2.1}$$

$$\mathscr{L}_{\rm f} = \frac{1}{2}\chi\left(i\bar{\sigma}^\mu D_\mu - M_\chi\right)\chi\,, \tag{2.2}$$

for scalars and fermions, respectively, where $D_\mu = \partial_\mu - ig_2 W_\mu^a T_\chi^a$ is the covariant derivative, and T_χ^a are generators in the n-th representation of SU(2). The Lagrangian for the real scalar in Eq. (2.1) also admits quartic self-coupling and Higgs-portal interactions at the renormalizable level. The latter is bounded from above by direct detection constraints (see Fig. 2.11 right) and gives a negligible contribution to the annihilation cross-section.[1]

The neutral component and the component with charge Q of the EW multiplet are splitted by radiative contributions from gauge boson loops. In the limit $m_W \ll M_{\rm DM}$ these contributions are non-zero and independent on M_χ. This fact can be understood by computing the Coulomb energy of a charged state at distance $r \gtrsim 1/m_W$ or the IR mismatch (regulated by m_W) between the self-energies of the charged and neutral states. The latter can be easily computed at 1-loop [95–97],

$$M_Q - M_0 \simeq \frac{Q^2 \alpha_{\rm em} m_W}{2(1+\cos\theta_W)} = Q^2 \times (167 \pm 4)\ \text{MeV}\,, \tag{2.3}$$

with the uncertainty dominated by 2-loop contributions proportional to $\alpha_2^2 m_t/16\pi$. These have been explicitly computed in Ref.s [98, 99] giving a precise prediction for the lifetime of the singly-charged component, which decays to the neutral one mainly by emitting a charged pion with

$$c\tau_{\chi^+} \simeq \frac{120\ \text{mm}}{T(T+1)}\,, \tag{2.4}$$

where $2T+1 = n$. The suppression of the lifetime with the size of the EW multiplet can be understood in the $M_\chi \gg m_W$ limit where the mass splitting between the charged and neutral components is independent of n while the coupling to W is controlled by $\sqrt{T(T+1)/2}$. As we will discuss in Sec. 2.4.2, the production of a singly charged DM component at colliders gives the unique opportunity of probing EW multiplets with $n = 3$ and $n = 5$ through disappearing tracks [23, 68, 92, 100, 101].

Interestingly, the IR generated splitting from gauge boson loops is not modified substantially by UV contributions. The latter are generated only by dimension 7 (dimension 6) operators if the DM is a Majorana fermion (real scalar) and can be written as

$$\Delta\mathscr{L}_I \supset \frac{c_I}{\Lambda_{\rm UV}^{n_I}} \chi^a \chi^b (H^\dagger T^a H)(H^\dagger T^b H)\,, \tag{2.5}$$

with $n_I = 3, 2$ for $I = f, s$. This corresponds to a splitting $\Delta M_I \simeq c_I v^4/\Lambda_{\rm UV}^{n_I} M_\chi^{3-n_I}$ which is always negligible with respect to the residual error on the 2-loop splitting for $\Lambda_{\rm UV} \gtrsim 100$ TeV and $c_I \sim \mathcal{O}(1)$.

[1] No other quartic coupling is allowed since $\chi T_\chi^a \chi$ identically vanishes. Indeed, $(T_\chi^a)_{ij}$ is antisymmetric in i, j, being the adjoint combination of two real representations, while $\chi_i \chi_j$ is symmetric.

We now move to discuss DM stability. In the case of the EW 3-plet, the renormalizable operators $\chi H^\dagger H$ and $\chi H L$, for scalars and fermions, respectively, can induce fast DM decay. We assume these operators to be forbidden by a symmetry (e.g. a discrete $\mathbb{Z}_2$-symmetry) acting only on the DM sector. For all the other n-plets with $n \geq 5$, instead, $\mathbb{Z}_2$-odd operators are accidentally absent at renormalizable level.

Higher dimensional operators that break the $\mathbb{Z}_2$-symmetry are in general expected to be generated at the ultraviolet cut-off scale $\Lambda_{\rm UV}$. We sketch here the operators of lowest dimension that can induce the decay of scalar and fermionic WIMPs for generic n:

$$\begin{aligned}\mathscr{L}_{\rm s} \supset & \frac{C_1^{(s)}}{\Lambda_{\rm UV}^{n-4}}\chi(H^\dagger H)^{\frac{n-1}{2}} + \frac{C_2^{(s)}}{\Lambda_{\rm UV}^{n-4}}\chi W_{\mu\nu}W^{\mu\nu}(H^\dagger H)^{\frac{n-5}{2}} + \cdots \\ & + \frac{C_w^{(s)}}{\Lambda_{\rm UV}^{n-4}}\chi(W_{\mu\nu}W^{\mu\nu})^{\frac{n-1}{4}} + \frac{C_{3\chi}^{(s)}}{\Lambda_{\rm UV}}\chi^3 H^\dagger H, \qquad (2.6)\\ \mathscr{L}_{\rm f} \supset & \frac{C_1^{(f)}}{\Lambda_{\rm UV}^{n-3}}(\chi H L)(H^\dagger H)^{\frac{n-3}{2}} + \frac{C_2^{(f)}}{\Lambda_{\rm UV}^{n-3}}(\chi\sigma^{\mu\nu}H L)W_{\mu\nu}(H^\dagger H)^{\frac{n-5}{2}} + \cdots \\ & + \frac{C_w^{(f)}}{\Lambda_{\rm UV}^{n-3}}(\chi H L)(W_{\mu\nu}W^{\mu\nu})^{\frac{n-3}{4}} + \frac{C_{3\chi}^{(f)}}{\Lambda_{\rm UV}^{3}}\chi^3 H L, \qquad (2.7)\end{aligned}$$

where SU(2) contractions are implicit, and the dots indicate operators of the same dimension with different combinations of W and H fields.[2] Higher-dimension operators with additional SM fields or derivatives are of course also possible. The first operators in the two equations above are just the renormalizable operators of the 3-plet case "dressed" with extra Higgs insertions. The dominant contribution to the decay width at tree-level always comes from the operator with the highest number of W insertions (namely $(n-3)/2$ for fermions and $2\lfloor(n-1)/4\rfloor$ for scalars). Notice that for fermionic DM, dipole-like operators with an odd number of W fields can always be constructed. In the last operator in both Eq. (2.6) and Eq. (2.7), χ^3 is the unique isospin triplet constructed out of three SU(2) irreducible representations of odd isospin [27, 35]. These operators contribute to the WIMP decay at one-loop as

$$\Gamma_{\rm s,f} \sim \frac{M_\chi}{2048\pi^5}\left(\frac{\alpha_2(n^2-1)}{4\pi}\right)^{\frac{n-3}{2}}\left[C_{3\chi}^{(s,f)}\left(\frac{M_\chi}{\Lambda_{\rm UV}}\right)^q\right]^2, \qquad (2.8)$$

where the exponent $q = 1$ (3) holds for scalars (fermions). For both scalar and fermionic WIMPs these are the dominant contributions for multiplets with $n > 5$. More precise results for specific n-plets have been computed in Ref.s [27, 35] but do not modify our conclusions. For *all* the scalar n-plets, DM decay is induced by a dimension 5 operator, and the required scale for stability is well above $M_{\rm Pl}$. As a consequence, the stability of scalar WIMPs can be determined only by understanding

[2] If $(n-1)/4$ is not integer, the operator with the highest number of W fields in Eq. (2.6) is $\chi(H^\dagger H)(W_{\mu\nu}W^{\mu\nu})^{\frac{n-3}{4}}$. Similarly, for the fermions in Eq. (2.7) it is $(\chi\sigma_{\mu\nu}HL)W^{\mu\nu}(W_{\rho\sigma}W^{\rho\sigma})^{\frac{n-5}{4}}$.

the subtle issues related to the fate of discrete symmetries in quantum gravity [102]. For fermionic representations, DM decay is instead induced by dimension 6 operators for $n \leq 5$, and dimension 7 operators for $n > 5$, and the DM stability can be determined within quantum field theory.

A lower bound on $\Lambda_{\rm UV}$ is obtained by requiring the DM lifetime to be long enough to circumvent cosmological bounds [103, 104] ($\tau_{\rm DM} \gtrsim 10^{19}$ sec) or astrophysical bounds on the decay products of decaying DM [94, 105, 106] ($\tau_{\rm DM} \gtrsim 10^{28}$ sec). We can then quantitatively measure the required *quality* of the $\mathbb{Z}_2$-symmetry by considering the ratio between the minimal $\Lambda_{\rm UV}$ allowed by the constraints and the WIMP freeze-out mass. A naive dimensional analysis (NDA) estimate of $\Lambda_{\rm UV}$, assuming all the Wilson coefficients to be $\mathcal{O}(1)$, is given in Table 2.1 for all the relevant n-plets.

Requiring perturbativity of the EW gauge coupling above the WIMP thermal mass can provide an upper bound on the dimension of the SU(2) representation. Indeed, large SU(2) n-plets will make the EW gauge coupling run faster in the UV, eventually leading to a Landau pole. In Table 2.1 we provide the value of the scale $\Lambda_{\rm Landau}$ such that $g_2(\Lambda_{\rm Landau}) = 4\pi$. We integrate the RGE equations for the SM gauge couplings at 2-loops and integrate-in the n-plet at the WIMP thermal mass.[3] Comparing $\Lambda_{\rm Landau}$ and $\Lambda_{\rm UV}$, we see that the stability of the fermionic n-plets with $n \leq 5$ only depends on physics in a regime where the EW coupling is still perturbative. Instead, the stability of n-plets with $n > 5$ requires specifying a UV completion for the EW gauge group that does not give rise to the dangerous operators of Eq. (2.6) and Eq. (2.7). In this sense, the Majorana 5-plet studied in Ref. [23] is special, because it can be made accidentally stable by raising the scale $\Lambda_{\rm UV}$, without any further assumption on the nature of the UV completion at $\Lambda_{\rm Landau}$.

Requiring $\Lambda_{\rm UV}/M_\chi \gtrsim 10$ to ensure perturbativity of the theory up to well above the WIMP mass would select $n \leq 9$ for fermions, and $n \leq 11$ for scalars. However, requiring a large hierarchy between $\Lambda_{\rm Landau}$ and M_χ is not necessary to ensure the calculability of thermal freeze-out, which depends only on EW processes at energies much below the DM mass. A more robust upper bound on the dimension of the SU(2) n-plets will be derived in Sec. 2.3, analyzing the s-wave unitarity of the annihilation cross-section. This bound will require $n \leq 13$ for both fermionic and scalar WIMPs.

2.2 WIMP cosmology

The determination of the DM thermal mass hinges on a careful computation of the DM annihilation cross-section in the non-relativistic regime. In particular, the potential generated by EW gauge boson exchange between DM pairs is attractive for isospins $I \lesssim \sqrt{2}n$ resulting into Bound State Formation (BSF) through the emission of an EW gauge boson in the final state. The energy of the emitted gauge boson is of the order of the Bound State (BS) binding energy $E_{B_I} \simeq \frac{\alpha_{\rm eff}^2 M_\chi}{4n_B^2} - \alpha_{\rm eff} m_W$, where n_B is the BS energy level, $\alpha_{\rm eff}$ is the effective weak coupling defined in Eq. (2.17),

[3] Our results are compatible with the ones found in Ref. [27] (where χ is integrated-in at M_Z) given that $\Lambda_{\rm Landau}/M_{\rm DM}$ is approximately independent on $M_{\rm DM}$.

and we neglected corrections of order m_W^2/M_χ^2. In the non-relativistic limit, and at leading order in gauge boson emission, the BSF process

$$\chi_i + \chi_j \to \mathrm{BS}_{i'j'} + V^a \tag{2.9}$$

is encoded in the effective dipole Hamiltonian described in Ref. [26, 36] which dictates the BS dynamics and it is written for completeness in Appendix A.

The BS dynamics relevant for DM freeze-out is well described by the unbroken phase of SU(2) so that the configuration of the DM pair can be decomposed into eigenstates of the isospin I of the pair

$$|\chi\chi\rangle_{II_z} = \mathcal{C}(II_z|ij)|\chi_i\chi_j\rangle, \quad I_z \in \left[-\frac{I-1}{2}, \frac{I-1}{2}\right], \tag{2.10}$$

where $\mathcal{C}(II_z|ij)$ are the Clebsch-Gordan coefficients and I is the dimension of the isospin representation. Denoting with L and S the total angular momentum and the spin, the isospin-Lorentz structure of the dipole Hamiltonian enforces the following selection rules: *i)* $\Delta S = 0$ because the dipole Hamiltonian is spin-independent; *ii)* $|\Delta L| = 1$ because the dipole operator transform as a vector under rotations; *iii)* $|\Delta I| = 2$ because a single, G-parity odd weak boson is emitted.

Since we are dealing with real representations, spin-statistics imposes further restrictions on the allowed quantum numbers, depending on the fermionic or scalar nature of the wave function. In particular we have

$$(-1)^{L+S+\frac{I-1}{2}} = 1 \ , \tag{2.11}$$

which implies that for scalars $n_B s$ ($n_B p$) bound states, *i.e.* with $L = 0$ ($L = 1$), can exist only with even (odd) $\frac{I-1}{2}$, while for fermions odd (even) $\frac{I-1}{2}$ states with $L = 0$ are forced to have $S = 1$ ($S = 0$).

We are now ready to describe the system of coupled Boltzmann equations for the evolution of the number densities of DM and BS. Following [26], we will discuss how this coupled system can be reduced to a single equation for the DM number density with an effective annihilation cross-section. The Boltzmann equations for DM and BS read

$$z\frac{\mathrm{d}Y_{\mathrm{DM}}}{\mathrm{d}z} = -\frac{2s}{H}\langle\sigma_{\mathrm{ann}}v_{\mathrm{rel}}\rangle\left[Y_{\mathrm{DM}}^2 - (Y_{\mathrm{DM}}^{\mathrm{eq}})^2\right] - \frac{2s}{Hz}\sum_{B_I}\langle\sigma_{B_I}v_{\mathrm{rel}}\rangle\left[Y_{\mathrm{DM}}^2 - (Y_{\mathrm{DM}}^{\mathrm{eq}})^2\frac{Y_{B_I}}{Y_{B_I}^{\mathrm{eq}}}\right] \ , \tag{2.12a}$$

$$\begin{aligned} z\frac{\mathrm{d}Y_{B_I}}{\mathrm{d}z} =& Y_{B_I}^{\mathrm{eq}}\left\{\frac{\langle\Gamma_{B_I,\mathrm{break}}\rangle}{H}\left[\frac{Y_{\mathrm{DM}}^2}{(Y_{\mathrm{DM}}^{\mathrm{eq}})^2} - \frac{Y_{B_I}}{Y_{B_I}^{\mathrm{eq}}}\right] + \frac{\langle\Gamma_{B_I,\mathrm{ann}}\rangle}{H}\left[1 - \frac{Y_{B_I}}{Y_{B_I}^{\mathrm{eq}}}\right]\right. \\ &\left. + \sum_{B_J}\frac{\langle\Gamma_{B_I\to B_J}\rangle}{H}\left[\frac{Y_{B_J}}{Y_{B_J}^{\mathrm{eq}}} - \frac{Y_{B_I}}{Y_{B_I}^{\mathrm{eq}}}\right]\right\} \ , \end{aligned} \tag{2.12b}$$

where $B_{I,J,\ldots}$ labels the different bound states, $z = \frac{M_\chi}{T}$, s is the entropy density and $Y = \frac{n}{s}$ is the number density per co-moving volume.

The dynamics of a given BS B_I in the plasma is described by Eq. (2.12b) and depends on: *i*) its ionization rate $\langle\Gamma_{B_I,\text{break}}\rangle$; *ii*) its annihilation rate into SM states $\langle\Gamma_{B_I,\text{ann}}\rangle$; *iii*) its decay width into other bound states $\langle\Gamma_{B_I\to B_J}\rangle$. The ionization rate $\langle\Gamma_{B_I,\text{break}}\rangle \equiv n_\gamma\langle\sigma_{I,\text{break}}v_\text{rel}\rangle$ encodes the probability of a photons from the plasma to break the BS B_I. Assuming thermal equilibrium, detailed balance relates the cross-section for the BS breaking $\langle\sigma_{I,\text{break}}v_\text{rel}\rangle$ to the BSF cross-section $\langle\sigma_{B_I}v_\text{rel}\rangle$

$$\langle\Gamma_{B_I,\text{break}}\rangle = \frac{g_\chi^2}{g_{B_I}}\frac{(M_\chi T)^{\frac{3}{2}}}{16\pi^{\frac{3}{2}}}e^{-\frac{E_{B_I}}{T}}\langle\sigma_{B_I}v_\text{rel}\rangle \ , \tag{2.13}$$

where g_{B_I} and g_χ count the number of degrees of freedom of the bound state B_I and of the DM multiplet, respectively. If either the BS decay or the annihilation rate satisfies $\Gamma \gg H$, we can neglect the LHS in Eq. (2.12b), obtaining algebraic relations between the DM and the BS yields.

Plugging these relations into Eq. (2.12a), we arrive at the final form of the DM Boltzmann equation

$$\frac{\mathrm{d}Y_\text{DM}}{\mathrm{d}z} = -\frac{\langle\sigma_\text{eff}v_\text{rel}\rangle s}{Hz}(Y_\text{DM}^2 - Y_\text{DM}^{\text{eq},2}) \ , \tag{2.14}$$

where

$$\langle\sigma_\text{eff}v_\text{rel}\rangle \equiv S_\text{ann}(z) + \sum_{B_J} S_{B_J}(z), \tag{2.15}$$

and we defined the effective cross-section as the sum of the direct annihilation processes, S_ann, and the ones which go through BSF, S_{B_J}. In particular, the dominant contribution to S_ann comes from s-wave processes and can be written as

$$S_\text{ann} = \sum_I \langle S_E^I \sigma_\text{ann}^I v_\text{rel}\rangle \ , \tag{2.16}$$

where σ_ann^I is the hard cross-section for a given isospin channel I, S_E^I is the Sommerfeld enhancement (SE) of the Born cross-section, and v_rel is the relative velocity of the two DM particles. In the limit of small relative velocity between the DM particles (but larger than m_W/M_χ), the SE factor can be approximated as

$$S_E^I \approx \frac{2\pi\alpha_\text{eff}}{v_\text{rel}} \ , \quad \text{where} \quad \alpha_\text{eff} \equiv \frac{I^2+1-2n^2}{8}\alpha_2 \ . \tag{2.17}$$

We include the correction due to partial waves higher than the s-wave in the estimate of the theoretical uncertainty. In particular, we estimate the correction to $(S_E^I\sigma_\text{ann}^I v_\text{rel})$ as

$$\frac{(S_E^I\sigma_\text{ann}^I v_\text{rel})_\text{p-wave}}{(S_E^I\sigma_\text{ann}^I v_\text{rel})_\text{s-wave}} \simeq v_\text{rel}^2 + \alpha_\text{eff}^2 \ . \tag{2.18}$$

The finite mass effects modify the behavior of the SE at $v_\text{rel} \lesssim m_W/M_\chi$ and are included in our full computation (see Ref. [90] for explicit formulas). However, Eq. (2.17) will be enough to estimate the behavior of the SE at the temperatures most relevant for freeze-out.

Analogously we can factorize the BSF processes as

$$S_{B_J} = \sum_{I,l} \langle S_E^I S_{B_J}^{I,l} \rangle R_{B_J} \ , \tag{2.19}$$

where $S_{B_J}^{I,l}$ is the "hard" BSF cross-section of the state B_J starting from a free state with angular momentum l and isospin I multiplied by the SE factor of that particular isospin channel as defined in Eq. (2.17). Explicit expressions for this can be found in Ref. [26, 36]. R_{B_J} gives instead the effective annihilation branching ratio into SM states which depends on the detailed BS dynamics (*i.e.* annihilation, ionization and decay). In particular, R_{B_J} approaches 1 once the temperature of the plasma drops below the binding energies of the bound states involved in the decay chains. In the case of a single BS, R_{B_J} takes a rather intuitive form

$$R_{B_J} = \frac{\langle \Gamma_{\rm ann} \rangle}{\langle \Gamma_{\rm ann} \rangle + \langle \Gamma_{\rm break} \rangle} \ , \tag{2.20}$$

which applies to $1s_I$ and $2s_I$ BS with $I \leq 5$. The latter, once formed, annihilate directly into pairs of SM vectors and fermions, with rates $\Gamma_{\rm ann} \simeq \alpha_{\rm eff}^5 / n_B^2 M_\chi$. These BS together make up for more of the 50% of the BSF cross-section. More complicated examples of BS dynamics will be illustrated in Appendix B where we detail the case of the EW 7-plet.

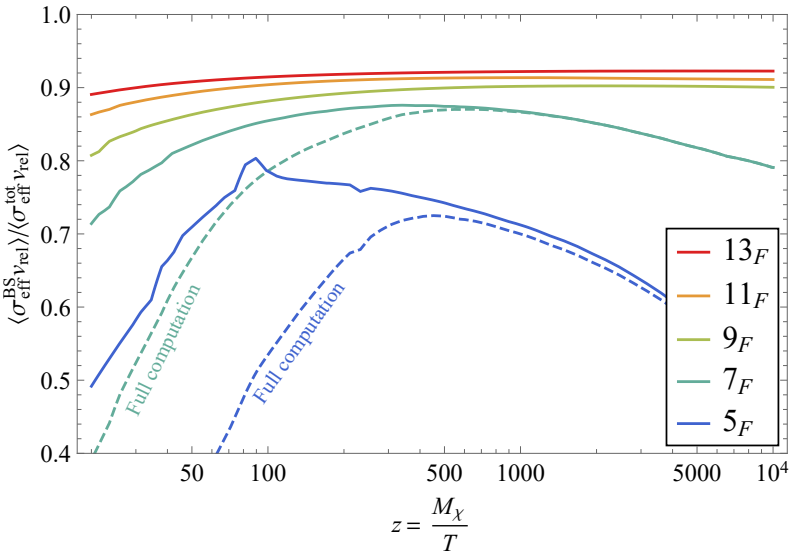

Figure 2.2: *Effective cross-section for BSF normalized over the total annihilation cross-section as a function of $z = M_\chi/T$ assuming vanishing ionization rates, i.e. $R_{BS} = 1$ (see Eq. (2.19) and below). The dashed lines for the fermionic 5-plet (dark blue) and 7-plet (cyan) show the deviation of the real bound state dynamics from the approximation of vanishing ionization rates. For $n > 5$ the error due to the $R_{BS} = 1$ is subdominant compared to the virtual and real effects at NLO in gauge boson emission.*

While the effect of BSF has already been computed for the fermionic 5-plet in Ref. [26], here we include it for the first time for all the real WIMP candidates with

$n \geq 7$. For larger EW multiplets, we find the relative effect of BS dynamics on the total cross-section increases, as can be seen from Fig. 2.2.

This is the consequence of two effects: *i*) the binding energy grows at large n, suppressing the ionization rate with respect to the annihilation one; *ii*) at larger n the number of attractive channels increases and thus the BS multiplicity per energy level grows linearly with n. For example, for $n = 5$ the attractive channels have $I = 1, 3, 5$, for $n = 7$ BS with $I = 7, 9$ can also form. The relevance of these higher isospin channels was not recognized in [107], where only the $I = 1, 3$ channels were included, significantly underestimating the thermal mass already for $n = 7$. In Appendix B we show explicitly the relative contributions coming from the different isospin channels for the 7-plet. The 7-plet thermal mass was computed including all the BS up to $3s$ and $2p$ but we checked that the contribution from $4s$ and $3p$ BS is negligible.

As we increase the dimension of the multiplet, the bound states become more tightly bounded and the effect of the ionization rate becomes smaller. This can be explicitly seen from Eq. (2.13) where the binding energy controls the Boltzmann suppression of the ionization rate. For this reason, we only account for the detailed BS dynamics for $n \leq 7$ while for $n > 7$ we set the annihilation branching ratios to 1. We assume, as explicitly checked for the 7-plet, that the formation cross sections for $4s$ and $3p$ BS are negligible. In fact, the cross sections of BS differring only for their principal quantum number have the same parametric dependence on n, so that the hierarchy between different energy levels is independent on n. Close to the unitarity bound limit, excited states with larger angular momentum can become important. However, their long lifetimes and small binding energies limit their contributions to the thermal mass. Moreover, since the typical velocity inside the bound state is α_{eff}/n_B, relativistic corrections can also be important. We leave the discussion of these contributions to a future work.

In Appendix B we estimate the error on the WIMP mass due to this approximation by comparing its effect on the thermal masses of 5-plet and the 7-plet against the full computation. We find a shift in mass $\Delta M_{DM} \simeq 5$ TeV for both $n = 5$ and $n = 7$ resulting in a smaller relative error for $n = 7$, as expected. We keep 5 TeV as an estimate of the error induced by this approximation for the larger multiplets.

Finally, we comment on the theory uncertainty on the mass prediction for the 5-plet. This is dominated by the approximate treatment of EW symmetry breaking effects in computation of the BSF cross-sections. The SU(2)-symmetric approximation fails once the DM de Broglie wavelength becomes of the order of m_W (i.e. for $z \simeq 10^4$ for $n \geq 5$). After the EW phase transition, Coulomb and Yukawa potentials appear at the same time so that employing either the Coulomb or the Yukawa centrifugal correction to the SE (see Ref. [90]) overestimate and underestimate, respectively, the freeze out cross-section. This gives us a rough way of determining the theory uncertainty: *i*) to set the lower bound on the freeze-out mass we include BSF in σ_{eff} until $z = 10^4$ with the centrifugal correction coming from the Yukawa; *ii*) to set the upper bound we push the effect of BSF, neglecting the vector masses in the centrifugal correction, to arbitrary large values of z. We observe that the abundance

saturates already for $z \approx 10^5$. This procedure gives the uncertainty for the 5-plet in Table 2.1 which is different than the one quoted in Ref. [26], where the BS contribution was switched off at $z = 10^4$, underestimating the effect of BSF.

2.3 The WIMP Unitarity Bound

We now analyze the constraint of perturbative unitarity on the annihilation cross-section, including bound state formation. The perturbative unitarity of the S-matrix sets an upper bound on the size of each partial wave contribution to the total annihilation cross-section [4]

$$(\sigma_{\rm eff} v_{\rm rel})^J \leq \frac{4\pi(2J+1)}{M_\chi^2 v_{\rm rel}} \,, \tag{2.21}$$

where $\vec{J} = \vec{L} + \vec{S}$ is the total angular momentum. The stronger inequality comes from the s-wave channel (i.e. $J = 0$) which can be written as

$$(\sigma_{\rm ann} v_{\rm rel}) + \sum_{B_J} f^0_{B_J} (\sigma_{B_J} v_{\rm rel}) \leq \frac{4\pi}{M_\chi^2 v_{\rm rel}} \,, \tag{2.22}$$

where $f^0_{B_i}$ selects the BS contributions that can be formed by $J = 0$ initial wave, which are limited by the selection rules discussed in the previous Section.

For a scalar WIMP selecting the s-wave implies $L = 0$, and only BS in p-orbitals can contribute to the s-wave cross-section with $f^0_{\rm BS} = 1$. The spin statistics of the wave function in Eq. (2.11) forces these BS to have odd $(I-1)/2$. In practice, the s-wave unitarity bound for scalars is determined solely by the SE. For fermionic WIMP selecting the s-wave implies the same selection rules of the scalar when $S = 0$. Additional contributions arise from $S = 1$ s-orbital states, whose isospin must be odd due to Fermi statistics. In this case, the projection onto the $J = 0$ wave gives $f^0_{\rm BS} = \frac{1}{9}$.

Solving the constraint in Eq. (2.22) we find that s-wave unitarity is violated for $n \geq 15$ for both fermion and scalar WIMPs. In both cases the s-wave cross-section is largely dominate by the SE. We checked that a similar constraint can be obtained by looking at the $p-$wave unitarity, where the cross-section is instead dominated by the formation of $1s$ BS.

The selection rules that regulates the BS dynamics derive from the dipole Hamiltonian which is written for completeness in Eq. (A.1). These selection rules are only broken by NLO contributions in gauge boson emission which can be estimated as

$$\frac{\Delta\sigma^{\rm NLO}_{\rm BSF}}{\sigma^{\rm LO}_{\rm BSF}} \sim \frac{\alpha^3_{\rm eff}}{64\pi} \,, \tag{2.23}$$

where the extra $\alpha^2_{\rm eff}$ correctly accounts for the phase space suppression in the limit of small velocities as detailed in Appendix A. As a result, the LO selection rules apply all the way till the breaking of perturbative unitarity.

[4] This constraint was derived for e^+e^- annihilations in [108, 109] and then used for the first time in the DM context in [28]. It can be checked that this constraints is not modified in the presence of long range interactions [110].

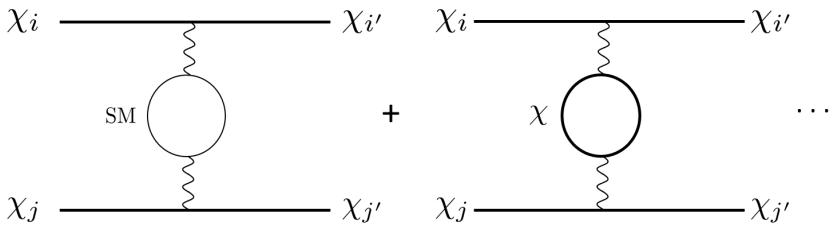

Figure 2.3: *Examples of Feynman diagrams contributing at NLO to the non-relativistic potentials as estimated in Eq. (2.24) (left) and Eq. (2.25) (right).*

Interestingly, the upper bound on n from perturbative unitarity derived from Eq. (2.22) is significantly stronger than the one derived from the perturbative unitarity of the Born cross-section which is violated for $n \geq 38$ (i.e. $\alpha_{\rm eff} \geq 4\pi$). This is a consequence of including the leading order SE to the hard annihilation cross section. One can ask if next-to-leading (NLO) corrections to the SE would significantly modify the annihilation cross section.[5] Estimating the NLO corrections to the potential controlling the SE we have two contributions: i) the ones with the SM fields running in the loops schematically showed in Fig. 2.3 left where first computed in Ref. [112] for the triplet and generalized in Ref. [113] for n-plets ii) the ones with the heavy fields running in the loops generating new contact terms (delta functions and their derivatives) in the non relativistic potential. The expected size of this corrections with respect to the LO potential can be estimated as

$$\frac{\Delta V_{\rm NLO}^{\rm light}}{V_{\rm LO}} \sim \frac{\alpha_2 b_2^{\rm SM}}{2\pi} \log\left(\frac{M_\chi v}{M_{\rm W}}\right) , \tag{2.24}$$

$$\frac{\Delta V_{\rm NLO}^{\rm heavy}}{V_{\rm LO}} \sim \frac{\alpha_{\rm eff}}{8\pi} v^2 \log v , \tag{2.25}$$

where the corrections from the SM fields are controlled by the SM gauge coupling at the EW scale, log-enhanced by the large ration between the DM mass and the EW scale. The UV contributions are instead controlled by $\alpha_{\rm eff}$ which is much larger than α_2 for large n-plets but are velocity suppressed essentially because the long range behavior of the LO potential dominates for $v \ll 1$.

Putting together the estimates in Eq. (2.23) and above, we showed that the LO SE and BSF remain the leading effects up to the WIMP unitarity bound. We estimate the theory uncertainty coming from these effects to be dominated by the SM running in Eq. (2.24), while the other NLO effects account for less than 1% because of the large coupling or velocity suppression.

Finally, we compare our results to the ones obtained in Ref. [107]. Numerically, the upper bound on the WIMP mass corresponding to the saturation of the unitarity

[5] This discussion was updated after the analysis of Ref. [111] was completed.

bound is roughly 500 ± 40 TeV, which is the expected thermal mass for $n = 15$ as can be seen from Fig. 2.1. The unitarity boundary was set instead to 150 TeV for $n = 13$ in Ref. [107] without a quoted theory uncertainty. Beside the numerical differences, our computation differ from the one in Ref. [107] in two crucial instances: *i*) at large n we find that large isospin channels enhance significantly the BSF cross-section making the WIMP DM mass *heavier* than in Ref. [107] at fixed n; *ii*) we find that including BSF does not accelerate by much the saturation of the unitarity bound because of the selection rules of the dipole Hamiltonian at LO. As we discussed above, the LO selection rules are not lifted by NLO corrections until the boundary of perturbative unitarity is reached. These two effects together push the heaviest calculable WIMP mass very close to the PeV scale appreciably enlarging the EW WIMP scenarios beyond the reach of any realistic future collider.

2.4 WIMP at high energy lepton colliders

We now look at the possible detection strategies for direct production of WIMPs at collider experiments. From the results in Table 2.1 one can immediately see that DM masses $\gtrsim 50$ TeV are required to achieve thermal freeze-out for EW multiplets with $n > 5$. Pair-production of these states would require center-of-mass energies exceeding 100 TeV, which are unlikely to be attained at any realistic future facility. On the other hand, multiplets with $n \leq 5$ have thermal masses in the few TeV range, potentially within the reach of present and future colliders.

Direct reach on these dark matter candidates at hadron colliders is limited by the absence of QCD interactions for the DM candidates, which can be produced only via electro-weak interactions. As such the limits at the LHC (see e.g. [29]) are rather far from the interesting thermal mass targets and only a future pp collider may have the reach for some low-n candidates if collisions around 100 TeV can be attained [101, 114, 115]. Lepton colliders tend to have reach mainly through indirect effects, e.g. the modification of the angular distributions in simple $f\bar{f}$ production at center of mass energies below the threshold to produce the DM pair. The reach in this case is up to masses a factor a few above the center of mass energy [30, 116].

A very-high-energy lepton collider, such as a muon collider, would be the perfect machine to hunt for these WIMPs, due to its large center-of-mass energy, relatively clean collision environment, and the capability of pair-producing weakly interacting particles *up to kinematical threshold*. Here we consider in particular a future muon collider with center-of-mass energy of 10 TeV or more and the baseline integrated luminosity of [38]

$$\mathcal{L} \simeq 10 \text{ ab}^{-1} \cdot \left(\frac{\sqrt{s}}{10 \text{ TeV}} \right)^2 . \tag{2.26}$$

While such a machine is currently not feasible, various efforts to overcome the technological challenges are ongoing. Early developments on machine performances [117, 118] found the luminosity Eq. (2.26) to be achievable for $\sqrt{s} \lesssim 6$ TeV, and further development to push it to larger energies is currently in progress [119].

We consider various search channels for EW 3-plets and 5-plets, and determine the

minimal center-of-mass energy and luminosity required to directly probe the freeze-out predictions. First, we detail in Sec. 2.4.1 the prospects for the observation of DM as undetected carrier of momentum recoiling against one or more SM objects. We systematically study all the "mono-V" channels, where DM is recoiling against a SM gauge boson $V = \gamma, Z, W$. We also investigate double vector boson production, that we dub "di-V" channels, where requiring a second SM gauge boson in the final state could help ameliorating the sensitivity. Second, in Sec. 2.4.2 we study the reach of disappearing track searches – which are robust predictions of WIMPs in real EW representations as discussed in Sec. 2.1 – recasting the results of [68]. Finally, in Sec. 2.4.3 we consider the direct production of WIMP BS. BS with the same quantum numbers of EW vectors can be resonantly produced by the leptons in the beam and then quickly decay to SM fermions. When the center-of-mass energy of the collider is close to the BS mass, this channel represents the most promising among the different WIMP collider signatures. Notice that our study is in principle applicable both to high-energy $\mu^+\mu^-$ and e^+e^- colliders, even though soft QED radiation, beam-strahlung, and the presence of beam-induced backgrounds could affect the results in different ways.

The projections for direct production derived here have to be contrasted with similar studies in the context of future high energy proton machines [100, 101] (which are limited by the partial reconstruction of the collision kinematics) or electron-positron machines [120, 121] (which are limited by the moderate center-of-mass energy and hence more effective to hunt for lighter DM candidates) .

Complementary studies have also considered indirect probes of WIMPs at future high energy lepton colliders, focusing on the modifications of Drell-Yan processes [30]. Given the freeze-out masses of Table 2.1, EW n-plets with $n > 5$ are beyond the reach of any realistic future collider both *directly* and *indirectly*, even though a definitive statement about indirect observables would require further studies.

2.4.1 WIMPs as missing momentum

We perform a full study of the different channels to observe DM as undetected carrier of momentum. The generic strategy is to measure a hard SM particle or a set of particles X recoiling against a pair of invisible objects,

$$\ell^+\ell^- \to \chi^i\chi^j + X\,. \tag{2.27}$$

Notice that we treat all the components χ^i of the EW multiplet as invisible, assuming the soft decay products of the charged states to be undetected. Additional soft SM radiation is also implicit in Eq. (2.27). The prospects for the "mono-photon" topology at a future muon collider have been already studied in [92]. Here, we want to extend this analysis by enlarging the set of SM objects recoiling against the invisible DM multiplets.

Mono-V. We start by considering "mono-V" scattering processes where $V = \gamma, Z, W$ is a generic EW gauge boson that accompanies the production of χ states from the n-plet,

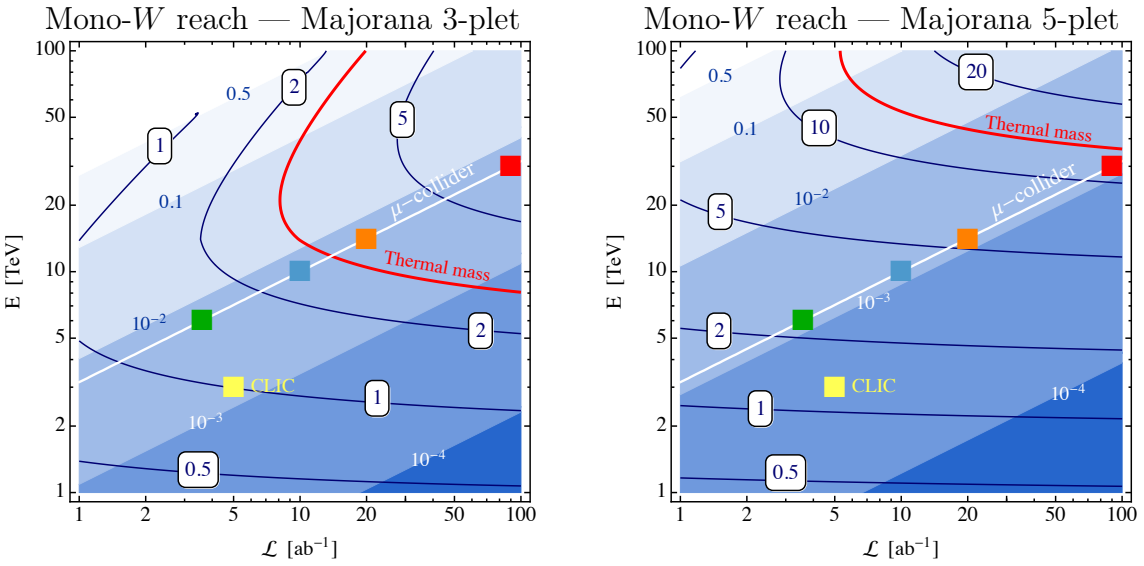

Figure 2.4: *Reach from mono-W searches at a muon collider, as a function of collider center-of-mass energy $\sqrt{s}$ and integrated luminosity $\mathcal{L}$. The blue contours show the 95% C.L. reach on the WIMP mass; the prediction from thermal freeze-out is shown as a red line. The precision of the measurement is shown by the blue shadings. Systematic uncertainties are assumed to be negligible. The white line corresponds to the luminosity scaling Eq. (2.26), with various collider benchmarks shown as colored squares: $\sqrt{s} = 6$ TeV green, $\sqrt{s} = 10$ TeV blue, $\sqrt{s} = 14$ TeV orange and $\sqrt{s} = 30$ TeV red. The yellow square corresponds to the 3 TeV CLIC [122].* **Left:** *Majorana 3-plet.* **Right:** *Majorana 5-plet.*

$$\text{mono-}\gamma\text{:} \qquad \ell^+\ell^- \to \chi^i\chi^{-i} + \gamma\,, \tag{2.28}$$

$$\text{mono-}Z\text{:} \qquad \ell^+\ell^- \to \chi^i\chi^{-i} + Z\,, \tag{2.29}$$

$$\text{mono-}W\text{:} \qquad \ell^+\ell^- \to \chi^i\chi^{-i\mp1} + W^\pm\,. \tag{2.30}$$

The main contribution to all these processes comes from initial- and final-state radiation of a vector boson, which have sizeable rates because of the large weak charge of the DM multiplet and the weak charge of the beams.[6] We sum over all components of the multiplet χ^i, but the dominant signal corresponds to the production of the state with largest electric charge ($i = \pm n$), subsequently decaying into DM plus soft SM particles.

For each of these signals, the corresponding SM background is dominated by a single process,

$$\text{mono-}\gamma\text{ bkg:} \qquad \ell^+\ell^- \to \gamma\nu\bar{\nu}\,, \tag{2.31}$$

$$\text{mono-}Z\text{ bkg:} \qquad \ell^+\ell^- \to Z\nu\bar{\nu}\,, \tag{2.32}$$

$$\text{mono-}W\text{ bkg:} \qquad \ell^+\ell^- \to W^\mp\nu \;+\; \ell^\pm(\text{lost})\,, \tag{2.33}$$

[6] The mono-Higgs signal has a much lower cross-section due to the suppression of initial- and final-state radiation. Furthermore, final-state radiation is model-dependent for scalar DM.

where the missing transverse momentum is carried by neutrinos; the mono-W background also requires a lost charge along the beam.

We simulate signal and background events with MadGraph5_aMC@NLO [123, 124], for different DM mass hypotheses and different collider energies. The W and Z bosons are assumed to be reconstructed from all their visible decay products and are treated as single objects. We impose basic acceptance cuts on the rapidity and transverse momentum of the vectors, requiring $|\eta_V| < 2.5$ and $p_{\mathrm{T},V} > 10$ GeV. Other detector effects are neglected.

We then perform a cut-and-count analysis, estimating the significance of the signal as

$$\text{significance} = \frac{S}{\sqrt{S + B + \epsilon_{\text{sys}}^2 \left(S^2 + B^2\right)}} \,, \tag{2.34}$$

where S, B are the numbers of physical signal and background events, and ϵ_{sys} parametrizes the systematic uncertainties. The signal is isolated from the background employing the kinematics of the visible object, parametrized in terms of its transverse momentum $p_{\mathrm{T},V}$, its pseudo-rapidity η_V, and the missing invariant mass (MIM) which is a function of the energy of the visible particle itself

$$\text{MIM} = \left(s + m_V^2 - 2\sqrt{s} E_V\right)^{1/2} \,. \tag{2.35}$$

We select events with MIM $\geq 2M_\chi$, $p_{\mathrm{T},V} \geq p_{\mathrm{T},V}^{\text{cut}}$, $|\eta_V| \leq \eta_V^{\text{cut}}$, where the p_{T} and η selection cuts are chosen to maximize the significance for each value of M_χ.

The background rates for mono-γ and mono-Z are very similar, with fiducial cross-sections of around 3 pb that depend weakly on the collider energy. As already pointed out in [92] for the mono-γ case, the optimal reach on M_χ is obtained for low signal-to-noise ratios – in other words, systematic uncertainties could be important. For this reason, we present results for different values of $\epsilon_{\text{sys}} = 0, 1‰, 1\%$.

The mono-W differs from the other two channels. The SM background is dominated by vector boson fusion (VBF) processes, that lead to forward leptons (lost along the beam pipe) and W bosons. The signal is instead made of events where the W is radiated from the initial or final states, leading to a more central distribution. The cut on $p_{\mathrm{T},W}$ can efficiently suppress the VBF background, with a lesser impact on the signal compared to the mono-γ or mono-Z cases. As a consequence, we find that the mono-W search has the best sensitivity among the various mono-X channels. The 95% C.L. exclusion reach on M_χ for a Majorana 3-plet and 5-plet is shown in Fig. 2.4 as a function of collider center-of-mass energy $\sqrt{s}$ and luminosity $\mathcal{L}$. We also show the expected values of S/B for the excluded signal in absence of systematic errors, which are rather low also for the mono-W search.

Due to the presence of initial-state radiation, the W boson of the signal has a preference for being emitted in the forward (backward) direction, measured with respect to the flight direction of the ℓ^- beam, if its charge is negative (positive). Since the charge of the W boson is potentially observable for leptonic decays, we can envisage a strategy to isolate the signal from the background using the full distribution in η_W (instead of its absolute value). We thus also perform an analysis

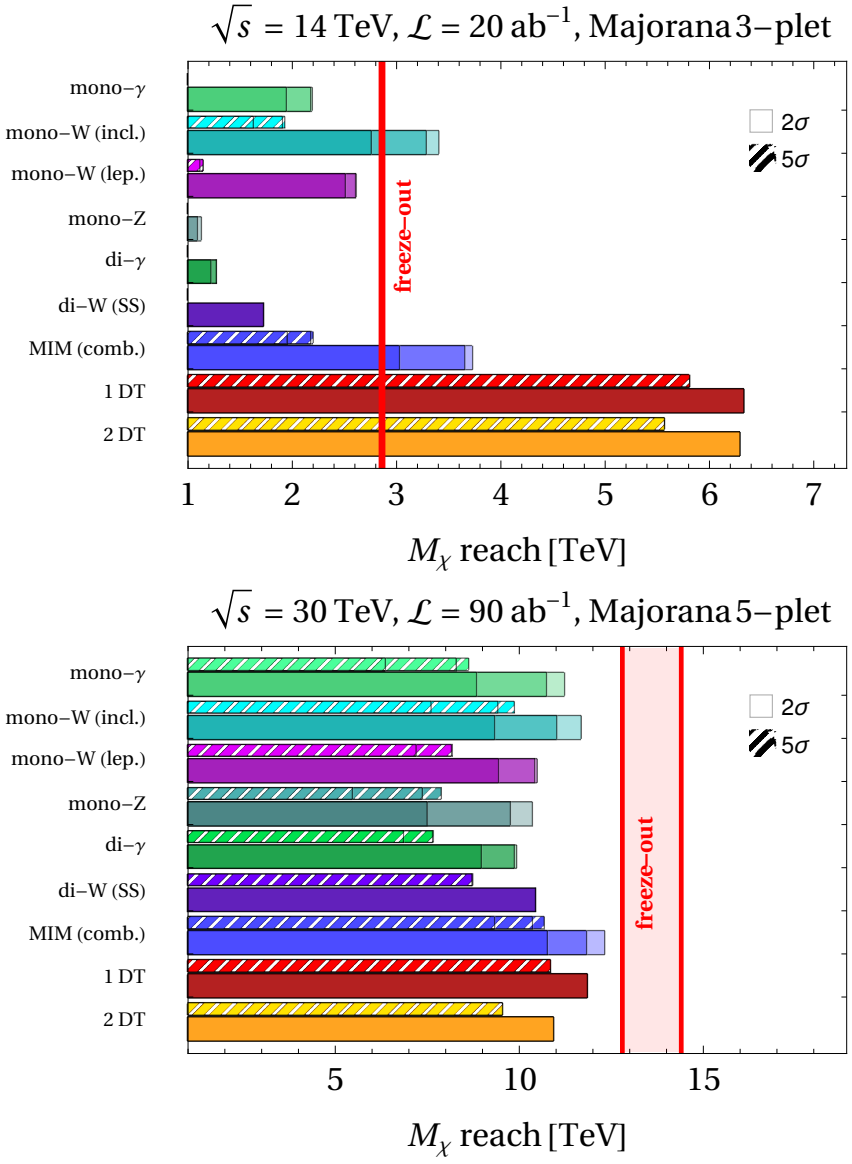

Figure 2.5: *Different bars show the* 2σ *(solid wide) and* 5σ *(hatched thin) reach on the WIMP mass at a muon collider for different search channels. The first seven bars show the channels discussed in Sec. 2.4.1 where DM would appear as missing invariant mass (MIM) recoiling against one or more SM objects: mono-gamma, inclusive mono-W, leptonic mono-W, mono-Z, di-gamma, same sign di-W, and the combination of all these MIM channels (blue). The last two bars show the reach of disappearing tracks as discussed in Sec. 2.4.2, requiring at least 1 disappearing track (red), or at least 2 tracks (orange). All the results are shown assuming systematic uncertainties to be 0 (light), 1‰(medium), or 1% (dark). The vertical red bands show the freeze-out prediction.* **Above:** *Majorana 3-plet for* $\sqrt{s} = 14\,\text{TeV}$ *and* $\mathcal{L} = 20\,\text{ab}^{-1}$. **Below:** *Majorana 5-plet for* $\sqrt{s} = 30\,\text{TeV}$ *and* $\mathcal{L} = 90\,\text{ab}^{-1}$.

of leptonic mono-W events, where we impose the additional cut $\eta_{W^\pm} \lessgtr 0$. We find the reach of this search to be weaker than the one of the inclusive mono-W because of the small leptonic branching ratio. However, the leptonic mono-W search possesses signal-free regions of the η_W distribution which would allow for an *in situ* calibration of the background from the data itself, leading to possible reduction of the systematic uncertainties.

Di-V. We now consider scattering processes with multiple emission of vector bosons. While generally being suppressed by higher powers of the gauge coupling constant, these processes can be enhanced for large center-of-mass energies, and for multiplets with large weak charge. They can therefore provide very useful handles to probe WIMPs in the regimes where the mono-V searches have very low signal-to-noise ratios. Of course, a too large rate for multiple boson radiation would indicate the breakdown of the perturbative expansion, requiring the resummation of large logarithms. We have checked that for the EW 3-plet and 5-plet, and for the energies under consideration here, the fixed-order computations are still accurate.

First, we consider the di-photon process

$$\ell^+\ell^- \to \chi^i\chi^{-i} + \gamma\gamma\,. \tag{2.36}$$

We apply the same acceptance cuts of the mono-γ analysis, and in addition we require a separation $\Delta R_{\gamma\gamma} > 0.4$ between the two photons. We employ the same event selection strategy of the mono-γ case, using as variables η_X, $p_{\mathrm{T},X}$, where X is the compound $\gamma\gamma$ system. Moreover, we require each photon to be as central as the $\gamma\gamma$ system itself. For the 5-plet, we find that the di-γ search can be stronger than the mono-γ in presence of large systematic uncertainties, where suppressing the SM background is more important. For the 3-plet, which has a smaller EW charge, the signal yield is too much affected by the requirement of a second emission to be competitive with the mono-V. In both cases, the values of S/B for the excluded di-γ signal are much larger than for the mono-γ signal, and systematic errors thus have a smaller impact.

Second, we consider the double W emission

$$\ell^+\ell^- \to \chi^i\chi^{-i\mp 2} + W^\pm W^\pm\,, \tag{2.37}$$

which holds a potentially very clean signature due to the two same-sign W bosons. We focus on leptonically decaying W bosons to ensure that their charge can be accurately tracked. A potential SM background consists in events with two lost charged particles, with the leading contribution being

$$\ell^+\ell^- \to W^-W^-W^+W^+\,, \tag{2.38}$$

where two W bosons of same sign are lost. This background is however negligible, as pairs of W bosons with opposite charge tend to be radiated from the same external leg and to be collinear: requiring only one of two collinear W bosons to be within detector acceptance reduces the rate to negligible levels. The other possible

background is given by events with a misidentified charge,

$$\ell^+\ell^- \to W^-W^+(\text{mistag})\ \nu\bar{\nu}\ , \tag{2.39a}$$
$$\ell^+\ell^- \to W^-W^+(\text{mistag})\ \ell^+\ell^-\ , \tag{2.39b}$$

where in the second case the charged final-state leptons are lost along the beam line. Requiring $p_{\mathrm{T},WW} \gtrsim \sqrt{s}/10$ makes the process in Eq. (2.39b) subdominant with respect to the $\nu\bar{\nu}$ background Eq. (2.39a). On top of this p_T cut, we do not apply further selection cuts, and simply require the two W bosons to be within the geometrical acceptance of the detector, $|\eta_W| < 2.5$. As an estimate for the charge misidentification probability we take $\epsilon_{\text{misid}} = 10^{-3}$.

Due to the negligible background contamination, the same-sign di-W signal has a much higher signal-to-noise ratio than the mono-V channels and even than the di-photon signal, reaching up to $S/B \sim \mathcal{O}(1)$. This makes this channel very robust against systematic uncertainties, and particularly effective for large n-plets $n \geq 5$ at higher energies due to their large EW charge. This signature may be one of the most robust and convincing signal of $n = 5$ multiplets at colliders. Further sources of background and a proper characterization of the missing (transverse) momentum in this reaction depend on detector performances, as well as on the knowledge of the initial state of the collision to be used in the computation of kinematic variables. We leave a careful evaluation of these aspects to future work.

We summarize the results of all the mono-V and di-V signatures discussed above in Fig. 2.5, where we show the 95% C.L. exclusion on M_χ for real fermion 3-plets and 5-plets, together with the 5σ discovery potential, at two benchmark muon colliders. We also show the combined reach from all these missing mass channels. The bands with different shadings correspond to different systematic uncertainties. One can see that the inclusive mono-W yields the strongest exclusion for both the 3-plet and the 5-plet. The main effect of di-V searches is to reduce the impact of systematic uncertainties. A 14 TeV muon collider with the benchmark luminosity of Eq. (2.26) would be able to probe a thermally-produced Majorana 3-plet WIMP, while a center-of-mass energy of slightly above 30 TeV is needed to probe the thermal freeze-out mass with missing energy searches in the case of the 5-plet.

Scalar WIMPs have lower production cross-sections. Missing mass searches do not allow to put stringent constraints on their mass, nor to probe the masses required for thermal freeze-out. We provide more details on the collider signatures, and results for real scalars in Appendix F.

2.4.2 Disappearing tracks

A second handle to tag the production of EW WIMPs at colliders is the detection of tracks from the charged states in the n-plet. As discussed in Sec. 2.1, the decay of $\chi^\pm \to \chi^0\pi^\pm$ has a lifetime of roughly $c\tau_{\chi^+} \simeq 48\ \text{cm}/(n^2-1)$, which is sufficiently long-lived to give rise to reconstructed tracks of length $\mathcal{O}(\text{cm})$ for $n = 3, 5$ that can be observable at colliders. The resulting tracks from these processes are somewhat too short for regular track reconstruction to work efficiently and they will show up as

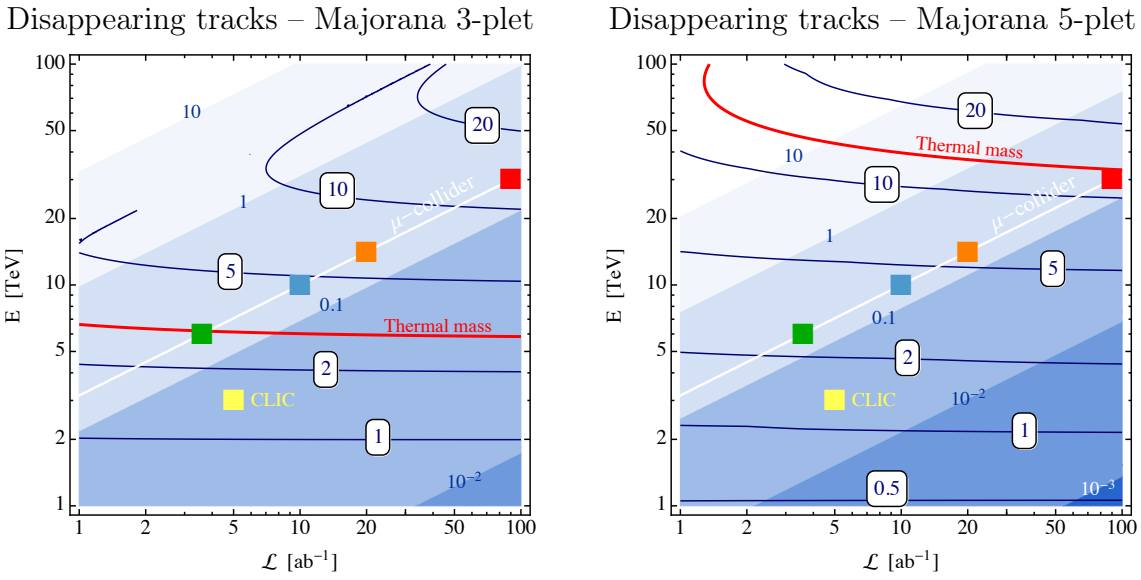

Figure 2.6: *Same as Fig. 2.4, but for disappearing track searches in mono-γ events.* **Left:** *Majorana 3-plet.* **Right:** *Majorana 5-plet.*

disappearing tracks (DTs), with missing hits in the outermost layers of the tracker and with little or no activity in the calorimeter and the muon chamber. States with higher electric charge in larger multiplets decay promptly to $\chi^{\pm}$, and eventually contribute to the number of disappearing tracks.

A full-detector level study has shown that a high energy lepton collider like CLIC at $\sqrt{s} = 3$ TeV can reconstruct them sufficiently well to separate them from other sources of look-alike short tracks [125, 126]. A recent study [68] has attempted a first evaluation of the performance of this type of search at a multi-TeV muon collider. A main source of worry and a main difference with respect to e^+e^- machines is the abundant number of tracker hits from underlying event activity due to the muon beam decay and to the resulting secondary particles from the interactions with the machine and detector materials. These hits can accidentally become a potentially severe source of background for searches aimed at highlighting the presence of short tracks of BSM origin. We do not enter in the details of these issues here, and simply follow the analysis of [68], which is based on a simulation of beam-induced background at 1.5 TeV, and recast their results for the EW 3-plet and the 5-plet. We remind that the background from decaying muons is expected to decrease at higher energies, making our estimate conservative in this sense.

We consider mono-photon events with disappearing tracks, and search for events compatible with a WIMP signal. Following [68], we distinguish two event-selection strategies to hunt for disappearing tracks: i) events with at least a disappearing track with $p_{\rm T} > 300$ GeV and a hard photon with $E_\gamma > 25$ GeV; ii) events with a hard photon, and two disappearing tracks originating from the same point along the beam axis. To estimate the reach we work in the cut-and-count scheme as in Eq. (2.34), and ignore systematic uncertainties.

The result of our recast is shown in the last two columns of Fig. 2.5 for Majorana

3-plets and 5-plets at two benchmark colliders, and in Fig. 2.6 as a function of collider energy and luminosity. One can see that DTs are especially powerful in the case of the 3-plet, where the reach goes almost up to the kinematical threshold. In particular, an EW 3-plet WIMP of mass as predicted by thermal freeze-out can be discovered already at a 6 TeV muon collider as suggested in [68, 92]. For higher n-plets DT substantially loose exclusion power because the lifetimes of the $\chi^{\pm} \to \chi^0 \pi^{\pm}$ decay become shorter. For the 5-plet the DT reach is comparable to the combined reach of the MIM searches.

As discussed in more detail in Appendix F, DT searches are particularly important to probe scalar WIMPs, since the lower production cross-sections have no significant impact on these almost background-free searches. Disappearing tracks might be the only direct signature of scalar WIMPs at collider experiments.

We recast the two search strategies discussed in Ref. [68] that exploit the presence of a single short reconstructed disappearing track or a two-track analysis that require at least one of them to be a short disappearing track, in addition to a trigger photon. The requirements are summarized in Table 2.2 from Ref. [68].

	Single track (1T)	Double track (2T)
E_γ	> 25 GeV	> 25 GeV
$p_{\rm T}$ leading track	> 300 GeV	> 20 GeV
$p_{\rm T}$ subleading track	/	> 10 GeV
θ leading track	$\frac{2\pi}{9} < \theta < \frac{7\pi}{9}$	$\frac{2\pi}{9} < \theta < \frac{7\pi}{9}$
Δz tracks	/	< 0.1 mm

Table 2.2: *Event selections in the two signal regions considered in the original work [68].*

Single-track search. For the single-track analysis we take the background cross-section quoted in [68]. This rate is mainly determined by the combinatorial of track reconstruction induced by beam-induced backgrounds.[7] To determine the rate of the single-track events, we compute the mono-photon cross-section doubly differential in the polar angles of the charged particles χ_1, χ_2. This $d\sigma/d\theta_1 d\theta_2$ is obtained at LO in perturbation theory with MadGraph5_aMC@NLO and is further reweighted to take into account angular and distance sensitivity to stub-tracks reported in Ref. [68]. Let $P(\theta_1)$ be the probability that the particle χ_1 is reconstructed as a track:

$$P(\theta, r_{\rm min}, r_{\rm max}) = \int_{r_{\rm min}}^{r_{\rm max}} \frac{{\rm d}r\, \epsilon_{\rm rec}(r,\theta)}{c\tau\beta\gamma \sin\theta} e^{-r/(c\tau\beta\gamma\sin\theta)}, \tag{2.40}$$

where r is the transverse radius and $\epsilon_{\rm rec}(r,\theta)$ is the probability to reconstruct as a track a particle travelling at an angle θ that decayed at a transverse radius r given in Fig. 11 of Ref. [68]. For single tracks $\epsilon_{\rm rec}(r,\theta)$ is 0 outside the interval $r \in [50\,{\rm mm}, 127\,{\rm mm}]$, and outside $\pi/6 < \theta < 5\pi/6$. The radial condition reflects

[7] As acknowledged in [68], this estimate of the background is quite conservative because it is based on detailed beam dynamics simulation for $\sqrt{s} = 1.5$ TeV. Due to the relativistic dilution of muon decays, we expect smaller background cross-section at higher $\sqrt{s}$.

the fact that tracks can only be reconstructed if the particles make at least 4 hits in the vertex detector, which for the considered geometry means that the particle must travel at least a minimum distance of 50 mm in the detector, while the upper limit stems from the disappearing condition of the track. The latter condition will be relaxed in the 2-tracks search. With the knowledge of ϵ_{rec} the integral in Eq. (2.40) can be performed numerically. As per Table 2.2, the hard cross-section $\sigma_{S,\gamma}$ is subject to trigger requirements: the leading observed track is required to have

$$p_{\text{T}} > 300 \text{ GeV} \tag{2.41}$$

to help discriminate it against fake tracks, and it must lie within the cone

$$\frac{2\pi}{9} < \theta < \frac{7\pi}{9}. \tag{2.42}$$

In our recast, due to lack of a detailed tracking and detector simulation, these cuts are implemented at parton level on the DM particles momenta, which leads us to overestimates the number of events that pass the selection. To account for this effect we assume that only a fraction ϵ_{tran} of the events with parton $p_{\text{T}} > 300$ GeV gives a track whose p_{T} fulfils the same conditions. The transfer factor $\epsilon_{\text{tran}} \approx 0.5$ is estimated from the p_{T} distribution of χ obtained at generator level, and track p_{T} distribution given in Ref. [68]. We assume that tracks with $p_{\text{T}} > 300$ GeV can only come from χ with $p_{\text{T}} > 300$ GeV. To properly avoid over-counting events with two reconstructed tracks, we divide the final state phase space into two non-overlapping regions that require different reconstruction constraints:

i) Both χ fulfil the conditions to be considered as leading track (Eq.s (2.41) and (2.42)). In this case both tracks are subject to the detection and reconstruction efficiencies ϵ_{tran} and $\epsilon_{\text{rec}}(\theta, r)$. These events may give rise to zero, one, or two reconstructed stub-tracks. We count events with at least one stub-track.

ii) Exactly one χ fulfils the conditions to be considered as leading track. Only events in which this track is reconstructed according to detection and reconstruction efficiencies ϵ_{tran} and $\epsilon_{\text{rec}}(\theta, r)$ are counted. The fate of the sub-leading χ (if any) is irrelevant.

The largest contribution to the single-track cross-section comes from events in region i), where both DM particles satisfy the p_{T} and θ requirements to be considered as a leading track. The preference for this configuration reflects the approximate 2-body kinematics of the mono-γ events with small p_{T}. In order to understand the nature of signal we can split it into two further sub-categories with: a) exactly one reconstructed track which fulfils the conditions Eq. (2.41) and Eq. (2.42); b) exactly 2 reconstructed stub-tracks, of which at least one fulfils the same conditions. The respective rates are given by:

$$\frac{\mathrm{d}^2\sigma^{1\text{T}}_{S,\gamma}}{\mathrm{d}\cos\theta_1 \mathrm{d}\cos\theta_2} \cdot \begin{cases} \epsilon_{\text{tran}} 2P(\theta_1)(1 - P(\theta_2)) & 1 \text{ track}, \\ \left(1 - (1 - \epsilon_{\text{tran}})^2\right) P(\theta_1) P(\theta_2) & 2 \text{ tracks}, \end{cases}$$

where the hard cross-section $\sigma^{1\text{T}}_{S,\gamma}$ is restricted to the phase-space region where both χ particles fulfil the requirements of Eq.s (2.41) and (2.42). The boost factor $\beta\gamma$

and the angular distribution are both taken from a MC sample with cuts only on the photon at generator level.

The resulting number of events is used to compute the reach on the DM mass reported in Fig. 2.5, according to Eq. (2.34) with $\epsilon_{\rm sys} = 0$.

Interestingly, the results obtained from the MC sample can also be understood semi-analytically thanks to the simple kinematics of the mono-photon process. Given that the photon tends to be soft, the kinematics of the three body process is not too different from direct production of a pair of oppositely charged DM particles without the photon. Therefore a very good analytic approximation of the above results can be obtained, with the χ boost factor and flight directions approximated by the ones for pair-produced DM particles with energy $\sqrt{s}/2$,

$$\beta\gamma \approx \sqrt{\frac{s}{4M_\chi^2} - 1}\,, \qquad \theta_1 = \pi + \theta_2. \tag{2.43}$$

The angular distribution can also be computed analytically in the 2-body limit,

$$\frac{1}{\sigma_{S,\gamma}}\frac{\mathrm{d}\sigma_{S,\gamma}}{\mathrm{d}\cos\theta} \propto \begin{cases} 1 + 4\frac{M_\chi^2}{s} + \left(1 - 4\frac{M_\chi^2}{s}\right)\cos^2\theta\,, & \text{fermion,} \\ \sin^2\theta\,, & \text{scalar.} \end{cases}$$

Results obtained using the MC 3-body angular distributions are in good agreement with the ones obtained with this analytic two-body approximation.

Double-track search. The signal of the double tracks is computed by requiring both DM particles to be reconstructed as tracks. The rate in this case is

$$\frac{\mathrm{d}^2\sigma^{2\mathrm{T}}_{\mathrm{S},\gamma}}{\mathrm{d}\cos\theta_1 \mathrm{d}\cos\theta_2} P(\theta_1)P(\theta_2)\,. \tag{2.44}$$

We additionally require the two tracks to originate from points that are close to each other along the direction of the beam axis, $\Delta z < 0.1$ mm (see Table 2.2). This effectively reduces the background to negligible levels. In this limit, we use 4 signal events as a conservative estimate of the 95% C.L. exclusion for a Poissonian counting.

The angular cuts on the tracks are the same as in the single track case, while the $p_{\rm T}$ cuts are much milder: $p_{\rm T} > 10, 20$ GeV for the sub-leading and leading tracks, respectively. In this case the mismatch between the $p_{\rm T}$ of the reconstructed track and the $p_{\rm T}$ of the charged χ obtained at generator level is negligible. The additional cuts do not affect significantly the signal events. Note that, following Ref. [68], the disappearing condition is required on at least one track, i.e. this analysis includes in the signal all events in which the second track extends up to a transverse radius of $r = 1153$ mm. Following Ref. [68], we assumed for such long tracks a reconstruction efficiency equal to the tracks decaying between 101 mm $< r <$ 127 mm. Also for double tracks, the result obtained using the MC sample $\beta\gamma$ and θ distributions are in agreement with the ones computed analytically in the 2-body limit.

We remark that for SU(2) triplets the double track analysis has a higher exclusion power than the single track analysis, whereas for $n \geq 5$ it has a lower reach. This is due to the shorter life-time $\tau_\chi \propto 1/n^2$ of larger multiplets, that suppresses the exponential decay factor of Eq. (2.40) twice in the double-track rate.

2.4.3 Bound State Production

BS with the same quantum numbers as electroweak vectors can be produced resonantly with large cross sections at lepton colliders. The only multiplet with such bound states in the spectrum is the Majorana 5-plet. In this case, a muon collider could resolve three such bound states. Besides, production rates are so large that details of DM spectroscopy can be probed with large statistics: we compute the characteristic pattern of single and multiple lines. Here we show that extra signals arise taking into account that such DM forms weak bound states with binding energy $E_B \sim 100\,\text{GeV}$. Such bound states annihilate into SM particles (including $\mu^+\mu^-$, for appropriate bound states with the same quantum numbers of electroweak vectors) with a width, $\Gamma_B \sim \alpha_2^5 M_\chi$, that is small but not much smaller than the expected energy resolution of a muon collider, $\sigma_E \sim 10^{-3}E$. Production and annihilation of DM bound states B thereby results into a large cross section among visible SM particles

$$\sigma(\mu^+\mu^- \to B \to f\bar{f}) \sim \sigma_{\text{peak}} \frac{\Gamma_B}{\sigma_E}, \qquad \text{where} \qquad \sigma_{\text{peak}} \sim \frac{4\pi}{s} \tag{2.45}$$

is the maximal cross section allowed by unitarity.

One needs to run around the peak $\sqrt{s} \approx 2M_\chi$, with $\sqrt{s} \approx 28$ TeV for the 5-plet. The energy resolution of a muon collider can be reduced by at least one order of magnitude, down to $\sigma_E \sim 10^{-4}E$, at the price of proportionally reducing its luminosity. We also consider other bound states and pp colliders, obtaining small cross sections as no resonant production is possible. [8] See Appendix C for further details.

As usual for bound states of two fermions, our states have quantum numbers $C = (-1)^{L+S}$ under charge conjugation and $P = (-1)^{L+1}$ under parity. The resulting 5-plet bound states at constituent mass $M_\chi = 13.7\,\text{TeV}$ are plotted in Fig. 2.7, and Tab. 2.3 lists their main properties.[9] Bound states can decay via annihilation of their constituents with rate Γ_{ann}, or into deeper states with rate Γ_{dec}. Bound states with $J \equiv L \oplus S$ equal to 1 or 5 can annihilate into two $\text{SU}(2)_L$ vectors VV, while vector bound states with $J = 3$ cannot because of the Landau-Yang theorem. We are especially interested in bound states that annihilate into SM fermions, as they

[8] DM bound states of an electroweak triplet have been discussed in [127] at a pp collider, where no resonant production is possible. We here include important non-abelian Coulomb-like potentials. See also [128].

[9] While we agree with the generic formulæ for the rates in [26], we found a missing order one factor in the application to the 5-plet: the decay rates of the $2p$ states differ from eq. (91) in [26] because a α_2 should be α_{eff}. These $2p$ decay rates negligibly affect the cosmological relic abundance computed in [26].

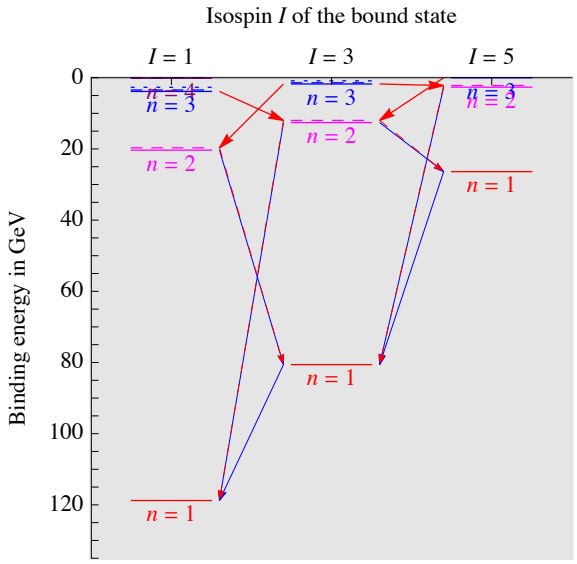

Figure 2.7: *Energy levels of bound states of two Minimal Dark Matter 5-plets with* $M_\chi = 14\,\text{TeV}$. *Continuous lines have* $L = 0$, *dashed lines have* $L = 1$, *dotted lines have* $L = 2$. *The blue (red) arrows indicate some main magnetic (electric) decays.*

can thereby be directly produced in $\mu^+\mu^-$ collisions. Such states are those with the same quantum numbers as the weak vectors W^a_μ, so that such bound states mix and inherit couplings to fermions. These special bound states are the ${}^n_1 s^{--}_3$ vector triplets with $S = 1$, $L = 0$ (the full notation is explained in the first row of table 2.3), which decay into SM fermions with rate $\Gamma_{\text{ann},f} = 625 M_\chi/2n^3 = 0.96\,\Gamma_{\text{ann}}$. The other vector triplet, the ${}^2_1 p^{+-}_3$ bound state with $S = 0$, $L = 1$, has opposite parity and annihilates in VVV rather than in fermions. The bound state ${}^3_J d^{--}_3$ with $L = 2$ has the right quantum numbers, but annihilation rates of bound states with $L > 0$ are suppressed by extra powers of α_2.

Table 2.3 also shows the decay widths among bound states: their computation will be discussed in Appendix C.2, where we discuss the associated collider signals.

All bound states have narrow total width, $\Gamma = \Gamma_{\text{ann}} + \Gamma_{\text{dec}} \ll M_\chi$. Then, their collider phenomenology is well approximated *à la* Breit-Wigner such that their decay widths determine their production rates. The cross section for s-channel production is

$$\sigma(i_1 i_2 \to B \to f) \approx \text{BW}(s)\sigma_{\text{peak}} \tag{2.46}$$

where

$$\text{BW}(s) = \frac{M_B^2 \Gamma_B^2}{(s - M_B^2)^2 + M_B^2 \Gamma_B^2} \simeq \Gamma_B M_B \pi\, \delta(s - M_B^2), \quad \sigma_{\text{peak}} = \frac{16\pi S_B}{M_B^2 S_{i_1} S_{i_2}} \text{BR}_{i_1 i_2} \text{BR}_f \tag{2.47}$$

and S_i is the spin times group multiplicity of the various particles (e.g. 2 for $\mu^\pm$, 3 if B is a vector singlet etc).

The cross section needs to be convoluted with the energy distribution of a muon collider, described by some function $\wp(s)$ normalized as $\int \wp(s) d\sqrt{s} = 1$. Assuming

name	Quantum numbers					Annihilation			Decay	
${}^n_J L_I^{PC}$	n	I	S	L	E_B	$\Gamma_{\rm ann}$		into	$\Gamma_{\rm dec}$	into
${}^1_1 s_1^{-+}$	1	1	0	0	118 GeV	$3240\,\alpha_2^5 M_\chi$	$\approx 1.63\,\text{GeV}$	$V\tilde{V}$	0	—
${}^1_1 s_3^{--}$	1	3	1	0	81 GeV	$15625\,\alpha_2^5 M_\chi/48$	$\approx 0.17\,\text{GeV}$	$f_L\bar{f}_L + HH^*$	$36\,\alpha_2^6\alpha_{\rm em} M_\chi \approx 4.6\,\text{keV}$	${}^1 s_1\gamma$
${}^1_1 s_5^{-+}$	1	5	0	0	26 GeV	$567\,\alpha_2^5 M_\chi/4$	$\approx 0.07\,\text{GeV}$	$V\tilde{V}$	$295\,\alpha_2^6\alpha_{\rm em} M_\chi \approx 38\,\text{keV}$	${}^1 s_3\gamma$
${}^2_1 s_1^{-+}$	2	1	0	0	20.3 GeV	$405\alpha_2^5 M_\chi$	$\approx 0.2\,\text{GeV}$	$V\tilde{V}$	$13\,\alpha_2^6\alpha_{\rm em} M_\chi \approx 1.7\,\text{keV}$	${}^1 s_3\gamma$
${}^2_1 s_3^{--}$	2	3	1	0	13 GeV	$15625\,\alpha_2^5 M_\chi/384$	$\approx 21\,\text{MeV}$	$f_L\bar{f}_L + HH^*$	$(6.9\,\alpha_2 + 0.3\,\alpha_{\rm em})\alpha_2^6 M_\chi \approx 3.7\,\text{keV}$	${}^1 s_{1+5} V$
${}^2_1 s_5^{-+}$	2	5	0	0	2.6 GeV	$567\,\alpha_2^5 M_\chi/32$	$\approx 9\,\text{MeV}$	$V\tilde{V}$	$28.4\,\alpha_2^6\alpha_{\rm em} M_\chi \approx 3.6\,\text{keV}$	${}^1 s_3\gamma$
${}^2_J p_1^{++}$	2	1	1	1	19.7 GeV	$\mathcal{O}(\alpha_2^7 M_\chi)$	$\sim$ keV	VV	$20.4\,\alpha_2^4\alpha_{\rm em} M_\chi \approx 2.5\,\text{MeV}$	${}^1 s_3\gamma$
${}^2_1 p_3^{+-}$	2	3	0	1	12 GeV	$\mathcal{O}(\alpha_2^8 M_\chi)$	$\sim 10\,\text{eV}$	VVV	$(30.2\,\alpha_2 + 0.3\,\alpha_{\rm em})\,\alpha_2^4 M_\chi \approx 15.3\,\text{MeV}$	${}^1 s_{1+5} V$
${}^2_J p_5^{++}$	2	5	1	1	2.2 GeV	$\mathcal{O}(\alpha_2^7 M_\chi)$	$\sim$ keV	VV	$4.7\,\alpha_2^4\alpha_{\rm em} M_\chi \approx 0.6\,\text{MeV}$	${}^1 s_3\gamma$
${}^3_1 s_1^{-+}$	3	1	0	0	3.8 GeV	$120\alpha_2^5 M_\chi$	$\approx 60\,\text{MeV}$	$V\tilde{V}$	$0.34\,\alpha_2^4\alpha_{\rm em} M_\chi \approx 42\,\text{keV}$	${}^2 p_3\gamma$
${}^3_1 s_3^{--}$	3	3	1	0	1.7 GeV	$15625\alpha_2^5 M_\chi/1296$	$\approx 6.0\,\text{MeV}$	$f_L\bar{f}_L + HH^*$	$(0.003 + 0.005)\alpha_2^4\alpha_{\rm em} M_\chi \approx 1\,\text{keV}$	${}^2 p_{1+5}\gamma$
${}^3_1 s_5^{-+}$	3	5	0	0	1.7 MeV	$21\alpha_2^5 M_\chi/4$	$\approx 2.7\,\text{MeV}$	$V\tilde{V}$	$0.3\alpha_2^4\alpha_{\rm em} M_\chi \approx 36\,\text{keV}$	${}^2 p_3\gamma$
${}^3_J d_3^{--}$	3	3	1	2	0.9 GeV	$\mathcal{O}(\alpha_2^9 M_\chi)$	$\sim$ eV	$f_L\bar{f}_L$	$0.4\alpha_2^4\alpha_{\rm em} M_\chi \approx 52\,\text{keV}$	${}^2 p_{1+5}\gamma$

Table 2.3: *Main bound states of fermion weak 5-plets with $M_\chi \approx 14\,\text{TeV}$. The parity $P = (-1)^{L+1}$ and charge conjugation $C = (-1)^{L+S}$ quantum numbers of bound states are broken by chiral weak gauge interactions to SM fermions. Hyper-fine components with different values of J have the same decay rate. Decay rates are not SU(2)$_L$-invariant because W, Z emission is sometimes blocked by phase space; we report decay rates averaged over the weak components of bound states.*

that each beam has a Gaussian energy distribution with standard deviation σ_E one gets a Gaussian distribution

$$\wp(s) = \frac{1}{\sqrt{2\pi}\Delta_E}\exp\left[-\frac{(\sqrt{s} - M_B)^2}{2\Delta_E^2}\right], \qquad \Delta_E = \sqrt{2}\sigma_E. \tag{2.48}$$

The energy resolution of a muon collider is expected to be $\sigma_E \approx 10^{-3}E \sim 14\,\text{GeV}$ [38], larger than the widths of bound states, $\Gamma_B \lesssim$ GeV. Thereby a muon collider cannot sit at the peak of the resonances, where the cross section is as large as allowed by unitarity. In the limit $\sigma_E \gg \Gamma_B$ the convoluted cross section is

$$\sigma(i \to B \to f) \simeq \epsilon\sigma_{\rm peak}, \qquad \epsilon = \frac{\sqrt{\pi}\,\Gamma_B}{4\sigma_E}. \tag{2.49}$$

Thanks to the σ_E at the denominator, bound states that can be directly produced from $i_1 i_2 = \mu^-\mu^+$ collisions can have cross sections comparable or bigger than tree-level SM cross sections, $\sigma \approx 4\pi\alpha_2^2/s$.

We here study states that can be directly produced from $\mu^-\mu^+$ collisions with a resonant s-channel cross section. These are the states with the same quantum numbers as electroweak vectors: $I = 3$, $S = 1$ and $PC = --$, achieved in view of the constituent fermion 5-plets χ. The first such state is ${}^{n=1}_{J=1}s^{--}_{I=3}$ (${}^1 s_3$ for short), that exists for $M_\chi \gtrsim 4.4\,\text{TeV}$. Table 2.3 shows that, for $M_\chi \approx 14$ TeV, ${}^n s_3$ bound states exist for $n = \{1, 2, 3\}$. The leading-order cross section for s-channel production of their neutral component B^0 is given by Eq. (2.49) with

$$\epsilon \approx \frac{1}{192 n^3}\frac{10^{-3}}{\sigma_E/E}, \qquad \sigma_{\rm peak}(\mu^+\mu^- \to B^0_{1s_3} \to f\bar{f}) = \frac{3\pi}{M_\chi^2}\,\text{BR}_\mu\text{BR}_f \approx 30\,\text{fb}\frac{\text{BR}_f}{\text{BR}_L} \tag{2.50}$$

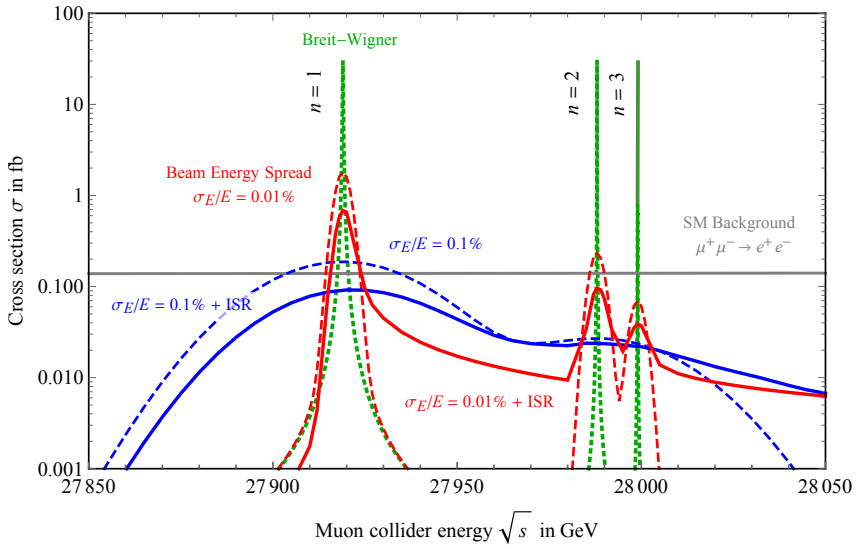

Figure 2.8: *Bound-state signals of a Minimal Dark Matter 5-plet with constituent mass* $M_\chi = 14$ TeV. *The dotted green curves show the signal cross section for production of* ${}^n s_1$ *DM bound states with* $n = \{1, 2, 3\}$, *ignoring the beam energy spread. The dashed curves show the signal cross section, for two different values of the beam energy spread,* $\sigma_E = 10^{-3}E$ *(baseline value) and* $\sigma_E = 10^{-4}E$ *(feasible value). The continuous curves show the signal cross section after also taking into account initial state emission. The gray horizontal curve is the SM* $\mu^+\mu^- \to e^+e^-$ *background.*

where $\mathrm{BR}_\ell = 1/25$ for any lepton flavour, and $\mathrm{BR}_q = 3/25$ for any quark flavour. The denominator is 25 (rather than 24), taking into account the 1/25 branching ratio into the Higgs multiplet. A more precise evaluation includes higher order effects. In particular, the signal cross section gets reduced by about a factor 2 taking into account initial state radiation (ISR) of γ and Z. We perform MonteCarlo simulations by approximating such bound states as vectors $B^a_{n\mu}$ coupled as $g_n B^a_{n\mu}(\bar{f}\gamma_\mu T^a f)_L$ to left-handed SM fermions, and choosing couplings g_n that reproduce the bound-state widths. Then, numerical results from MadGraph5_aMC@NLO show that γ radiation dominates. Such effect is analytically approximated by assigning a parton distribution function to each muon beam, such that the amount of muons with energy equal to the beam energy gets reduced by an order unity factor, analytically given by $\sim (\Gamma/M_\chi)^{4\alpha_{\rm em}\ln(E/m_\mu)/\pi}$ [129]. Precise analytical results [130] agree with numerical results.

Considering, for example, the e^-e^+ final state (so that calorimeters can precisely measure their large energy), the SM background is

$$\sigma_{\rm SM}(\mu^+\mu^- \to e^+e^-) = \frac{4\pi\alpha_{\rm em}^2}{3s} + \frac{2\pi\alpha_{\rm em}\alpha_2}{3c_w^2 s}(g_L+g_R)^2 + \frac{\pi\alpha_2^2}{3c_w^4 s}(g_L^2+g_R^2)^2 \approx 140\,\mathrm{ab}\,\frac{(28\,\mathrm{TeV})^2}{s} \tag{2.51}$$

where $s \gg M_Z^2$, $c_w = M_W/M_Z$, $g_L = 1/2 - c_w^2$, $g_R = 1 - c_w^2$. We see that $\sigma_{\rm peak}$ is 200 times larger than $\sigma_{\rm SM}$ (green dotted curve in Fig. 2.8) and that a design energy spread reduces it by $\epsilon \sim 1/200$ for $n = 1$, providing a DM signal at the level of total

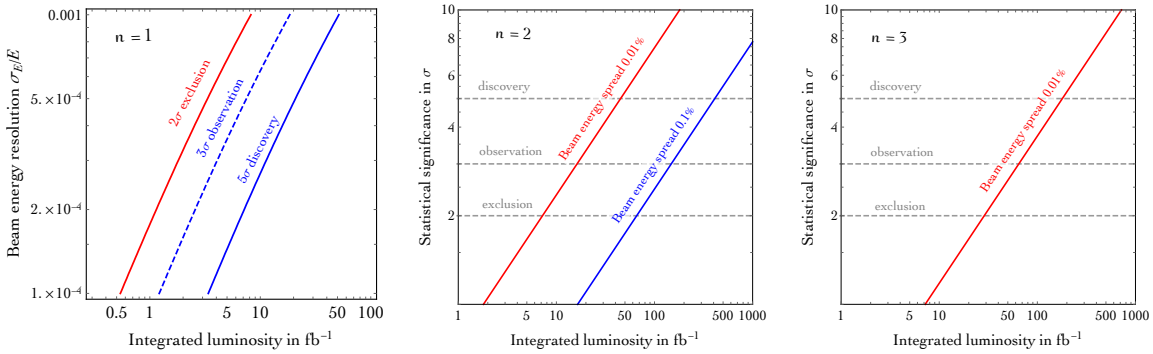

Figure 2.9: *The integrated luminosity needed to see the* ${}^n s_3$ *bound states with mass* $2M = 28\,\text{TeV}$ *of a Minimal DM 5-plet at a muon collider with* $s \approx 4M^2$ *is much smaller than the possible value,* $90/\,\text{ab}$ *at* $\sigma_E/E = 10^{-3}$.

SM backgrounds (dashed blue curve in Fig. 2.8). The $n = 1$ state can be mildly separated from those with $n = \{2, 3\}$, that have rates below the SM background and thereby need some dedicated search.

Fig. 2.9a shows that the integrated luminosity needed to discover such state corresponds to about one day of running, taking into account its annihilation channels into e^+e^- and jets and without performing selection cuts (for simplicity, we do not include annihilations into $\mu^+\mu^-$, which have a larger background due to t-channel vector exchange that can be efficiently reduced by cuts on p_T and other variables). We assumed a 70% efficiency for detecting each electron or jet in the final state. Reducing the beam energy spread reduces the needed integrated luminosity, but by an amount similar to the expected loss in collider luminosity.

With a feasible reduction of σ_E by one order of magnitude, the cross section for producing the ${}^1 s_3$ bound state becomes one order of magnitude larger than SM backgrounds, and the excited bound states with $n = 2, 3$ can be separated and acquire total cross sections at the level of the SM backgrounds (dashed red curve in Fig. 2.8). After taking initial state radiation into account, one obtains the continuous curves in Fig. 2.8, where peaks become asymmetric and larger above the threshold due to the 'radiative return' phenomenon. Fig. 2.9b,c show the integrated luminosity needed to discover such states. The non-resonant loop corrections considered by [127] at $\sqrt{s}$ slightly above the $2M_\chi$ threshold interfere destructively with the SM background leading to a decrease of the SM cross section by up to 8%.

Finally, we mention that the state ${}^3 d_3$ too has the same quantum numbers as electroweak vectors and can thereby be produced directly from $\mu^+\mu^-$ collision; however its annihilation rate (see bottom row of table 2.3) is highly suppressed by α_2^{5+2L} in view of $L = 2$ and we neglect it.

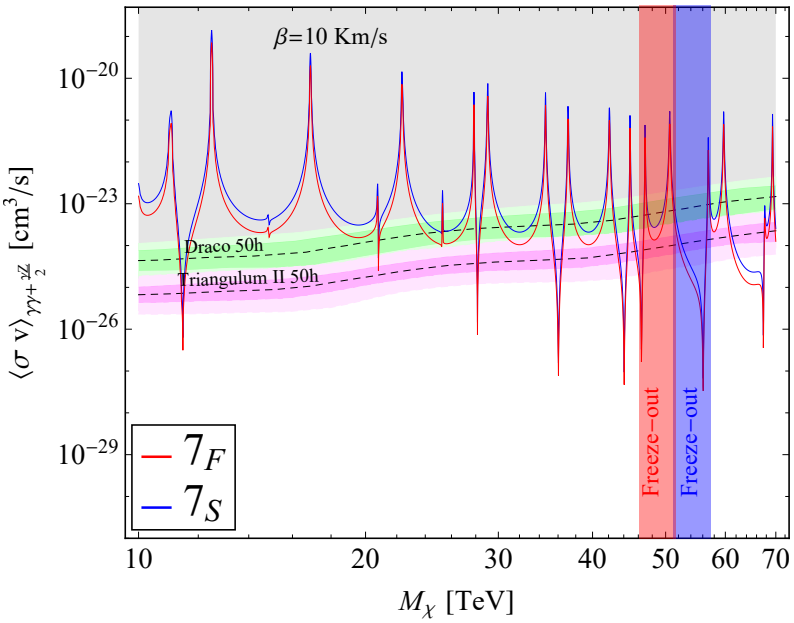

Figure 2.10: *Expected CTA sensitivities (dashed black lines) with 68% and 95% CL intervals derived as in Ref. [42] assuming 50 hours observation time towards Draco (green) and Triangulum II (magenta). We show the SE annihilation cross-section into the channels that contribute to the monocromatic gamma line signal (i.e. $\gamma\gamma$ an γZ) for a scalar 7-plet (blue) and a fermionic 7-plet (red). The vertical bands show the predicted thermal masses for the scalar 7-plet (blue) and the fermionic 7-plet (red), where the theory uncertainty is dominated by the neglected NLO contributions (see Table 2.1).*

2.5 WIMP direct and indirect detection

In this Section we briefly summarize the opportunities of the future experimental program in direct and indirect detection in light of the mass predictions derived in Table 2.1.

2.5.1 Indirect Detection

As anticipated in Chapter 1, the upcoming CTA telescope, thanks to its high sensitivity in the multi-TeV range with respect to current ground-based Cherenkov telescopes, represents a great opportunity to test the EW WIMP paradigm considered here. For this reason, we show a very preliminary analysis of ID signals coming from annihilations of the WIMP 7-plet. We focus on the CTA prospects by considering 50h of observations time towards two dSph targets in the northern hemisphere: the classic dSph Draco and the ultra-faint one Triangulum II. We do not consider the GC due to its large astrophysical uncertainties. Notice that the DM properties of Draco come from hundreds of stellar tracers, while those from Triangulum II are based on just 13 tracers, making the latter more speculative and subject to large systematics in the determination of the geometrical J-factor [131]. Hence, the reach of Draco should be taken as the baseline reach for CTA.

Our analysis is simplified because the signal shape we consider is essentially a single

line at $E_\gamma \simeq M_\chi$. Consistently we take the CTA prospects derived in Ref. [42] for a pure line. We ignore the contributions of the continuum spectrum, the extra features of the spectral shape induced by the resummation of EW radiation and the contribution of the BSF to the photon flux. While neglecting BSF is justified if we focus on very high energy photons, a careful computation of the $\gamma + X$ cross-section, where X is any other final state would be needed to precisely assess the experimental sensitivity [132]. In the last decade, many different groups have investigated the impact of large Sudakov logarithms and large collinear logarithms on the indirect detection reach, focusing mainly on the case of the fermionic 3-plet [133–137, 137]. The inclusion of these effects has been shown to increase the reach of $\sim 20 \div 30\%$ for the 3-plet [42, 76, 138] and it is expected to be even more important for higher DM masses.

In Fig. 2.10 we overlay the SE annihilation cross-section for the 7-plets at $v = 10$ km/sec against the CTA experimental reaches. In order to compute the SE in this velocity regime, we took advantage of the parametrization introduced in [139] and used the full expressions for the SE at leading order, including EW breaking effects. The SE saturate already at $v \simeq 10^{-3} \div 10^{-2}$ far away from the resonances. As we can see, both a 50 hour observation of Triangulum II and of Draco have good chances to detect the high energy γ line in the 7-plet annihilation spectrum.

As we see from Fig. 2.10, given the strong mass-dependence of the features of the SE cross-section, a major source of theoretical uncertainty on the reach of indirect detection is still the determination of the 7-plet thermal mass. Therefore, a full computation of the thermal relic mass including NLO effects is required together with a careful computation of the $\gamma + X$ cross-section along the lines of Ref.s [133–137, 137] to careful assess the indirect detection reach for the 7-plet.

Independently on our current inability of making a conclusive statement because of the large theory uncertainties, it is clear that large n-plets are a perfect target for future Cherenkov telescopes which deserves further theoretical study. A complementary open phenomenological question is if the low energies gamma lines at $E_\gamma \simeq E_B$ associated to BSF can be actually disentangled from the continuum (see [26, 140] for preliminary work in this direction). An analogous question can be asked for monocromatic neutrinos from BS annihilations.

2.5.2 Direct Detection

For $Y = 0$ the elastic scattering of DM with the nuclei is induced by EW loop diagrams first computed in [141, 142]. After EW gauge bosons are integrated out, the structure of the UV effective Lagrangian describing the DM interactions reads

$$\mathscr{L}_{\rm eff}^{\rm SI} = \bar{\chi}\chi \left(f_q m_q \bar{q} q + f_G G_{\mu\nu} G^{\mu\nu} \right) + \frac{g_q}{M_\chi} \bar{\chi} i \partial^\mu \gamma^\nu \chi \mathcal{O}^q_{\mu\nu} \,, \tag{2.52}$$

where we focus on the DM spin independent (SI) interactions with quarks and gluons [143]. The quark twist-2 operator is defined as

$$\mathcal{O}^q_{\mu\nu} \equiv \frac{i}{2} \bar{q} \left(D_\mu \gamma_\nu + D_\nu \gamma_\mu - g_{\mu\nu} \not{D}/2 \right) q.$$

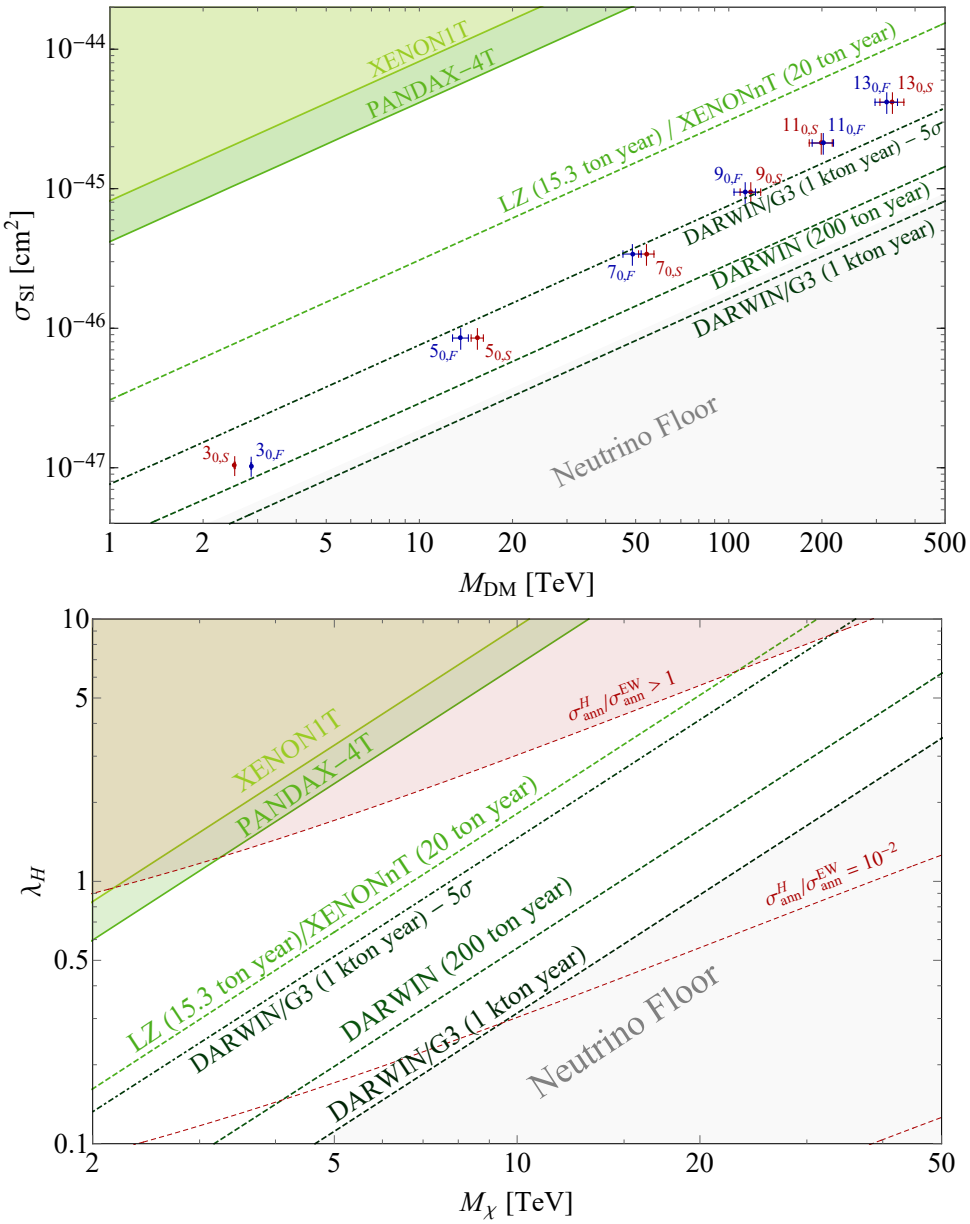

Figure 2.11: *The* **light green** *shaded region is excluded by the present experimental contraints from XENON-1T [52] and PandaX-4T [53], the* **green dashed** *lines shows the expected 95% CL reach of LZ/Xenon-nT [54, 55] and DARWIN [41, 50]. The light gray region show the neutrino floor for 200 ton/year exposure derived in Ref. [56].* **Above:** *Expected spin independent (SI) direct detection cross-section for Majorana n-plets (red) and for real scalar n-plets (blue) (assuming the Higgs portal coupling $\lambda_H = 0$). The vertical error bands correspond to LQCD uncertainties on the elastic cross-section in Eq. (2.56) while the horizontal error band comes from the theory determination of the WIMP freeze out mass.* **Below:** *Current and future reach on the Higgs portal quartic λ_H defined in Eq. (2.1) for scalar DM. In the shaded dark red region the quartic modifies the freeze-out cross-section by $\mathcal{O}(1)$ or more. The dashed red contours indicate smaller ratios of the Higgs-portal and the EW annihilation cross-sections.*

The Wilson coefficients of the operators for general EW n-plets with $Y = 0$ have been computed in Ref. [32] and at the leading order in $M_\chi/m_{W,h} \gg 1$ read

$$f_q^{\rm EW} \simeq \frac{(n^2-1)\pi}{16}\frac{\alpha_2^2}{m_W m_h^2}\,, \tag{2.53}$$

$$f_G^{\rm EW} \simeq -\frac{(n^2-1)}{192}\frac{\alpha_2^2\alpha_s}{m_W}\left(\frac{\sum_q \kappa_q}{m_h^2}+\frac{1}{m_W^2}\right)\,, \tag{2.54}$$

$$g_q^{\rm EW} \simeq -\frac{(n^2-1)\pi}{24}\frac{\alpha_2^2}{m_W^3}\,, \tag{2.55}$$

where $m_h = 125$ GeV is the SM Higgs mass, $q \in (c, b, t)$ and $\kappa_c = 1.32$, $\kappa_b = 1.19$, $\kappa_t = 1$.

Following Ref. [143], starting from the UV DM interactions we derive the IR interaction of DM with the nucleons. All in all, the SI elastic cross-section per nucleon in the limit $M_\chi \gg m_N$ reads

$$\sigma_{\rm SI}^{\rm EW} \simeq \frac{4}{\pi} m_N^4 |k_N^{\rm EW}|^2, \tag{2.56}$$

where m_N is the nucleon mass and $k_N^{\rm EW}$ is defined as

$$k_N^{\rm EW} = \sum_q f_q^{\rm EW} f_{Tq} + \frac{3}{4}(q(2)+\bar{q}(2))g_q^{\rm EW} - \frac{8\pi}{9\alpha_s} f_{TG} f_G^{\rm EW}\,.$$

with the dimensionless nucleon form factors defined as $f_{Tq} = \langle N|m_q\bar{q}q|N\rangle/m_N$, $f_{TG} = 1-\sum_q f_{Tq}$ with $q \in (u, d, s)$ and $\langle N(p)|\mathcal{O}^q_{\mu\nu}|N(p)\rangle = \frac{1}{m_N}(p_\mu p_\nu - \frac{1}{4}m_N^2 g_{\mu\nu})(q(2)+\bar{q}(2))$, where $q(2)$ and $\bar{q}(2)$ are the second moments of the parton distribution functions for a quark or antiquark in the nucleon taken from [32]. Notice that we choose a different set of values for the nucleon form factors with respect to previous studies [31] which explain the difference in our results. In particular, we take the FLAG average of the lattice computations in the case of $N_f = 2+1+1$ dynamical quarks [144–146].

By propagating LQCD uncertainties on the elastic cross-section (2.56), we obtain the vertical uncertainties on the SI cross-section predictions in Fig. 2.11. We find the partial accidental cancellation between the one loop and the two loop contribution to reduce the elastic cross-section up to 30%. The horizontal bars represent the uncertainties coming from the computation of the thermal masses through the relic abundance. As shown in the plot, while all the WIMP cross-sections lie above the Xenon neutrino floor as computed in [56] but only a very large exposure experiment like DARWIN [41] would be able to probe the heavy thermal WIMPs.

Spin dependent (SD) interactions of DM with the nuclei are also induced by EW loops

$$\mathscr{L}_{\rm eff}^{\rm SD} = d_q(\bar{\chi}\gamma^\mu\gamma_5\chi)(\bar{q}\gamma_\mu\gamma_5 q), \quad d_q \simeq -\frac{(n^2-1)\alpha_2^2\pi}{24 m_W M_\chi}, \tag{2.57}$$

where the Wilson coefficient was computed in Ref. [32] and we expanded it at zeroth order in $M_\chi/m_h \gg 1$. The corresponding SD cross-section is too small to be probed even at a very large exposure experiment like DARWIN.

Finally, we comment on the new opportunities for direct detection that arise for scalar DM. Here, a non-zero Higgs portal quartic in Eq. (2.2) leads to a new contribution to the SI DM scattering cross-section with the nuclei, which again in the $M_\chi \gg m_N$ limit reads

$$\sigma_{\rm SI}^{\rm H} = \frac{4}{\pi} m_N^4 |k_N^{\rm H}|^2 \,, \tag{2.58}$$

where

$$k_N^{\rm H} \simeq \frac{\lambda_H f_N}{4 m_h^2 M_\chi} \,, \tag{2.59}$$

with $f_N \simeq 0.31$ obtained from lattice QCD results (see [147] for a more detailed discussion on the scalar triplet). In the right panel of Fig. 2.11 we show the regions of parameter-space where the Higgs-portal interaction can be tested in direct detection. The requirement of not significantly affecting the freeze-out dynamics bounds the annihilation cross-section induced by the Higgs portal to be smaller than the EW cross-section, $\sigma_{\rm ann}^H/\sigma_{\rm ann}^{\rm EW} \lesssim 1$, which results in an upper bound on the quartic coupling λ_H shown by the red shading in Fig. 2.11. An estimate for this bound can be obtained by comparing the hard annihilation cross-sections, and reads $\lambda_H^2 \lesssim (n^2-3)(n^2-1) g_2^4/8$. Interestingly, XENON1T and PANDAX-4T already exclude a large part of the region where the Higgs portal induces $\mathcal{O}(1)$ modifications of the freeze-out predictions, while LZ will completely exclude this possibility.

2.6 Summary

In this Chapter, we computed all the calculable thermal WIMP masses for real EW representations with vanishing hypercharge. We included both Sommerfeld enhancement and bound-state-formation effects at LO in gauge boson exchange and emission. Our results are summarized in Table 2.1.

We found that the largest calculable SU(2) n-plet at LO is the 13-plet, which is as heavy as 350 TeV. Stronger requirements about the perturbativity of the EW sector up at high scales can further lower the number of viable candidates. We consistently assigned a theory error to our predictions by estimating the NLO corrections to the SE. The latter dominates the theory uncertainty for $n \geq 7$, while for $n = 5$ the error is dominated by the approximate treatment of EW symmetry-breaking effects in the computation of the BSF cross-sections.

Given the updated mass predictions from thermal freeze-out, we re-examined various phenomenological probes of WIMP DM.

High energy lepton colliders in the $10-30$ TeV range, such as a future muon collider, can directly produce EW multiplets with $n \leq 5$. In order to probe a Majorana fermion with $n = 3$ ($n = 5$) with missing-mass searches, a collider with at least $\sqrt{s} \sim 12$ TeV ($\sqrt{s} \sim 35$ TeV) and the baseline integrated luminosity of Eq. (2.26)

would be required. The highest mass reach is obtained by means of an inclusive mono-W search.

Interestingly, disappearing tracks originating from the decay of the singly-charged state into the neutral one are robust predictions of real EW multiplets with $Y = 0$, and ameliorate the sensitivity for the 3-plet compared to missing-mass searches. For the 5-plet we find the expected sensitivity of disappearing tracks to be very similar to the one of missing-mass searches due to the shorter average lifetime of the tracks.

We also studied the effects of WIMP bound states at future colliders. We found that bound states with the same quantum numbers as electroweak vectors can be produced resonantly with large cross sections by running lepton colliders at the appropriate $\sqrt{s}$. The first multiplet with such BS in the spectrum is the Majorana 5-plet. Fig. 2.8 shows that, at a muon collider running at $\sqrt{s} \approx 2M_\chi$ and with a beam energy spread $\sigma_E/E = 10^{-3}$ or better, the production rate of the neutral component of the bound-state triplet is so large that one day of running may be enough for discovery, see Fig. 2.9.

Scalar WIMPs can not be probed through missing-mass searches, due to their smaller production cross-section, nor with BS production, since the relevant bound states are absent in the spectrum due to spin-statistics. However, disappearing tracks searches are very powerful tests even for scalar multiplets, thanks to their very low background contamination. This signature is therefore a crucial ingredient to fully explore the parameter space of thermally produced WIMP Dark Matter at future colliders.

Heavy EW WIMPs with $n > 5$ are too heavy to be produced at colliders. However, they are perfect targets for indirect detection at upcoming ground-based Cherenkov telescopes like CTA. More theoretical work is necessary to make a robust forecast both on the determination of the photon spectrum for large n-plets and on improved precision predictions for the freeze-out masses.

Finally, large-exposure liquid Xenon experiments like DARWIN can in principle probe all the relevant EW WIMPs through their weak interaction with nuclei. Scalar WIMPs can further be tested through their Higgs-portal quartic interaction. Interestingly, $\mathcal{O}(1)$ modification of the thermal freeze-out masses due to the Higgs portal are already partially excluded by the XENON1T and PANDAX-4T results, and will be completely excluded by LZ.

Chapter 3

The Complex EW WIMP Window

In this Chapter, we conclude our EW WIMP classification with the study of complex representations with non-zero hypercharge ($Y \neq 0$)[1]. Conversely to their real counterparts, the non-zero hypercharge implies a non-zero coupling of DM to the Z-boson, which is severely excluded experimentally. This problem is tamed by making the DM inelastic, as explained in Section 3.1, so that the Z-mediated scattering between DM and the nucleons is kinematically forbidden.

Similarly to the previous Chapter, our goal here is to precisely determine and fully classify all the *calculable* freeze-out predictions for complex inelastic WIMPs, including Sommerfeld enhancement (SE) and Bound State Formation (BSF). The final purpose is to use these predictions to establish if and how the future experimental program will be able to test all the viable Complex WIMP multiplets. In particular, we will show how future large exposure direct detection experiments together with a future high energy muon collider will probe complementary portions of the complex WIMP parameter space.

Our results are summarized in Table 3.1, whose logic can be explained as follows. Once the DM mass is fixed from the freeze-out predictions, the phenomenology of complex WIMPs depends essentially on two parameters: i) the "inelastic" splitting between the-next-to lightest neutral component and the DM; ii) the "charged" splitting between the charged components and the DM. In our setup these splittings are generated by its (non-renormalizable) interactions with the SM Higgs (generated by unspecified UV dynamics).

The inelastic splitting δm_0 is bounded from below by DD constraints [148, 149] and BBN constraints on the decay of the next to lightest neutral component. Interestingly, this requrement alone selects a limited number of complex WIMPs: i) scalar and fermionic WIMPs with $Y = 1/2$ and even n up to the unitarity bound of the freeze-out annihilation cross section [28]; ii) scalar and fermionic WIMPs with $Y = 1$ and $n = 3, 5$. At the same time, the inelastic splitting is bounded from above by DD

[1] Complex EW representations include also multiplets with $Y = 0$. Some of these were discussed in Ref. [35], their phenomenology is similar to the one discussed in Ref. [83]. For completeness we give the full predictions for the thermal masses up to the limit of perturbative unitarity in Appendix E.1.

DM spin	n_Y	$M_{\rm DM}$ (TeV)	$\Lambda_{\rm Landau}/M_{\rm DM}$	$(\sigma v)^{J=0}_{\rm tot}(\sigma v)^{J=0}_{\rm max}$	δm_0 [MeV]	$\Lambda^{\rm max}_{\rm UV}/M_{\rm DM}$	δm_{Q_M} [MeV]
DC	$2_{\frac{1}{2}}$	1.08 ± 0.02	$> M_{\rm Pl}$	-	0.22 - $2 \cdot 10^4$	10^7	4.8 - 10^4
	3_1	2.85 ± 0.14	$> M_{\rm Pl}$	-	0.22 - 40	60	312 - 1.6 $\cdot 10^4$
	$4_{\frac{1}{2}}$	4.8 ± 0.3	$\simeq M_{\rm Pl}$	0.001	0.21 - $3 \cdot 10^4$	$5 \cdot 10^6$	20 - 1.9 $\cdot 10^4$
	5_1	9.9 ± 0.7	$3 \cdot 10^6$	0.003	0.21 - 3	25	$10^3 - 2 \cdot 10^3$
	$6_{\frac{1}{2}}$	31.8 ± 5.2	$2 \cdot 10^4$	0.01	0.5 - $2 \cdot 10^4$	$4 \cdot 10^5$	100 - $2 \cdot 10^4$
	$8_{\frac{1}{2}}$	82 ± 8	15	0.05	0.84 - 10^4	10^5	440 - 10^4
	$10_{\frac{1}{2}}$	158 ± 12	3	0.16	1.2 - $8 \cdot 10^3$	$6 \cdot 10^4$	1.1 $\cdot 10^3$ - $9 \cdot 10^3$
	$12_{\frac{1}{2}}$	253 ± 20	2	0.45	1.6 - $6 \cdot 10^3$	$4 \cdot 10^4$	2.3 $\cdot 10^3$ - $7 \cdot 10^3$
CS	$2_{\frac{1}{2}}$	0.58 ± 0.01	$> M_{\rm Pl}$	-	4.9 - $1.4 \cdot 10^4$	-	4.2 - $7 \cdot 10^3$
	3_1	2.1 ± 0.1	$> M_{\rm Pl}$	-	3.7 - 500	120	75 - 1.3 $\cdot 10^4$
	$4_{\frac{1}{2}}$	4.98 ± 0.25	$> M_{\rm Pl}$	0.001	4.9 - $3 \cdot 10^4$	-	17 - 2 $\cdot 10^4$
	5_1	11.5 ± 0.8	$> M_{\rm Pl}$	0.004	3.7 - 10	20	650 - 3 $\cdot 10^3$
	$6_{\frac{1}{2}}$	32.7 ± 5.3	$\simeq 6 \cdot 10^{13}$	0.01	4.9 - $8 \cdot 10^4$	-	50 - $5 \cdot 10^4$
	$8_{\frac{1}{2}}$	84 ± 8	$2 \cdot 10^4$	0.05	4.9 - 6 $\cdot 10^4$	-	150 - $6 \cdot 10^4$
	$10_{\frac{1}{2}}$	162 ± 13	20	0.16	4.9 - $4 \cdot 10^4$	-	430 - $4 \cdot 10^4$
	$12_{\frac{1}{2}}$	263 ± 22	4	0.4	4.9 - $3 \cdot 10^4$	-	10^3 - $3 \cdot 10^4$

Table 3.1: *Thermal masses of complex WIMPs with $Y \neq 0$, obtained including Sommerfeld enhancement and BSF. The upper bound on n for even multiplets comes from the perturbative unitarity bound, as can be seen from the $(\sigma v)^{J=0}_{tot}/(\sigma v)^{J=0}_{max}$, where $(\sigma v)^{J=0}_{max}$ is the maximal allowed annihilation cross section [28]. The loss of perturbativity is also signaled by the Landau pole Λ_{Landau} progressively approaching the DM mass. The upper bound on odd n with $Y = 1$ comes from the perturbativity of the higher dimensional operators generating δm_0 . For multiplets with $n > 5$ the largest UV cutoff Λ^{max}_{UV} required to generate the minimal viable splitting is smaller than $10 M_{DM}$. For each candidate we provide the allowed range for the mass splittings. The lower limit on δm_0 comes from strongest bound between direct detection and BBN as shown in Fig. 3.1. The upper bound from the most stringent condition between DD constraint from PandaX-4T [53] and the perturbativity of the coupling of $\mathcal{O}_0$ in Eq. (3.1). Similarly, the lower limit on δm_{Q_M} comes from the BBN bound on the charged state decay rate, while the upper limit from the strongest limit between DD and the perturbativity of the coupling of $\mathcal{O}_+$ in Eq. (3.1).*

constraints on Higgs-mediated nuclear recoils. This leaves a finite window for the inelastic splitting of every multiplet which we report in Table 3.1. This window will be further probed by large exposure DD experiments such as LZ [54], Xenon-nT [55], and ultimately by DARWIN/G3 [41, 50].

The natural value of the charged splitting δm_Q is fixed by the radiative EW contributions [95–97] but (non-renormalizable) interactions with the SM Higgs can induce large deviations from this value. In particular, for all the n-plets with non-maximal hypercharge, these interactions are required to make the DM stable.

The allowed range of the two splittings above controls the hierarchy of the states within the EW multiplet. In this parameter space one can map out the expected signals in a future hypothetical muon collider [66]. Depending on the lifetime of the charged states we can have different signatures at colliders: i) long lived charged tracks; ii) disappearing tracks (DT); iii) missing energy accompanied by an EW bosons. While the first two searches rely on the macroscopic decay length of the charged states, the last is directly related to the DM pair production recoiling against one (or more) EW boson. Bound state formation is clearly relevant also for com-

plex WIMPs. The richer dynamics coming from the presence of additional sources of mass splittings requires a more devoted analysis, which is left for future work. We briefly comment on it in Sec. 3.4.2. In general, a future muon collider could complement the large exposure DD experiments in probing complex WIMPs in regions of the parameter space where the DD drops below the neutrino floor of xenon experiments [150].

The doublet with $Y = 1/2$ ($2_{1/2}$) and the triplet with $Y = 1$ (3_1) stand out as the only two complex candidates for which the lightest component of the multiplet is guaranteed to be electrically neutral, which is a necessary requirement for DM. It is well known that the $2_{1/2}$ DD cross section lies well below the neutrino floor because of an accidental cancellation between the different contribution to the elastic cross section with the nuclei [32]. We find that a muon collider of $\sqrt{s} = 3$ TeV would only be able to exclude the fermionic EW doublet with a large luminosity from around $\mathcal{L} = 5$ ab^{-1} to $\mathcal{L} = 50$ ab^{-1}, depending on the assumed systematics, by a combination of charged tracks, disappearing, tracks and missing mass searches. Somewhat less high luminosity may suffice at a $\sqrt{s} = 6$ TeV collider, which can exclude the $2_{1/2}$ with 4 ab^{-1} and make a discovery with a more demanding 20 ab^{-1}.[2]

The DD cross section of the 3_1 can only be probed with large exposure Xenon experiment like DARWIN, while a muon collider of $\sqrt{s} = 10$ TeV would be able to make a discovery at the thermal mass for the fermionic 3_1 using a luminosity around 10 ab^{-1}, that is considered as a benchmark for currently discussed project for this type of collider [118, 151]. This is clearly a major theoretical motivation for a high energy muon collider which could be in the unique position of testing the few WIMP scenarios whose DD cross section lies well below (or in proximity) of the neutrino floor.

This Chapter is organized as follows: in Sec. 3.1 we summarize the main features of EW WIMP paradigm focusing on fermionic DM and relegating many details to Appendix D.1 and analogous formulas for scalar DM to Appendix D.2. This section provides a full explanation on the results of Table 3.1 while the more technical aspects of the freeze-out computation are given in Appendix A. In Sec. 3.3 we show how large exposure DD experiments can probe most of the complex WIMPs with the minimal inelastic and charged splittings. In Sec. 3.4 we study the full parameter space of the complex WIMPs, in the charged vs neutral splitting plane. We take as examples the doublet and 4-plet with $Y = 1/2$ and the triplet and 5-plet with $Y = 1$. In Sec. 3.5 we summarize the indirect probes of complex WIMPs in electroweak observables and the electron dipole moment (EDM). In Appendix E we discuss the freeze-out prediction for complex WIMPs with $Y = 0$ and in Appendix F we illustrate the collider reach for the scalar WIMPs.

[2]Note that our results on the DT differs from the ones in Ref. [68]. This discrepancy can be ascribed to their overestimation of the efficiency for DTs with short lifetimes. We thank the authors for correspondence on this. We believe that our projections on the mono-γ are stronger than the ones derived on Ref. [92] because of our optimization of the kinematical cuts.

3.1 Which Complex WIMP?

Within the complex EW WIMP class we can further distinguish two subclasses of complex WIMPs: a) complex representations with $Y = 0$ and odd n; b) complex representation with $Y \neq 0$ with even n (odd n) for half-integer Y (integer Y). The first subclass is a straightforward generalization of the models analyzed in Chapter 2, where the stability of the DM is guaranteed by an unbroken dark fermion number which can be gauged as was first done in Ref. [35]. For completeness, we give the freeze-out prediction of these scenarios in Appendix E.

In this Chapter we focus on complex WIMPs with $Y \neq 0$ whose phenomenology differs substantially from the one with $Y = 0$. We focus here on the fermionic case and leave the discussion about the scalar WIMPs to the Appendix D.2. The minimal Lagrangian for a fermionic complex WIMP with $Y \neq 0$ is:

$$\begin{aligned}
\mathscr{L}_{\rm D} &= \overline{\chi}\left(i\not{D} - M_\chi\right)\chi + \frac{y_0}{\Lambda_{\rm UV}^{4Y-1}}\mathcal{O}_0 + \frac{y_+}{\Lambda_{\rm UV}}\mathcal{O}_+ + \text{h.c.}\ , \\
\mathcal{O}_0 &= \frac{1}{2(4Y)!}\left(\overline{\chi}(T^a)^{2Y}\chi^c\right)\left[(H^{c\dagger})\frac{\sigma^a}{2}H\right]^{2Y}\ , \\
\mathcal{O}_+ &= -\overline{\chi}T^a\chi H^\dagger\frac{\sigma^a}{2}H\ ,
\end{aligned} \tag{3.1}$$

where T^a is a $\mathrm{SU}(2)_L$ generator in the DM representation. The main difference with respect to real WIMPs is that the renormalizable Lagrangian is no longer sufficient to make the DM model viable. In Eq. (3.1) we write only the minimal amount of UV operators required to make the DM model viable. As we discuss in Appendix D.1 these operators are also unique and possibly accompanied by their axial counterparts. These are obtained from the ones in Eq. (3.1) by adding a γ_5 inside the DM bilinear. We now illustrate the physical consequence of $\mathcal{O}_0$ and $\mathcal{O}_+$ in turn in Sec. 3.1.1 and Sec 3.1.2 and derive the implication for complex WIMPs in Sec. 3.1.3. We comment on DM stability in Sec. 3.1.4.

3.1.1 Inelastic splitting

The non-renormalizable operator $\mathcal{O}_0$ is required to remove the sizeable coupling to the Z boson of the neutral component χ_N of the EW multiplet

$$\mathscr{L}_Z = \frac{ieY}{\sin\theta_W\cos\theta_W}\overline{\chi}_N\not{Z}\chi_N\ . \tag{3.2}$$

This coupling would lead to an elastic cross section with nuclei already excluded by many orders of magnitude by present DD experiments [48]. After the EWSB, $\mathcal{O}_0$ induces a mixing between χ_N and χ_N^c. Replacing the Higgs with its VEV, $(H^{c\dagger})\frac{\sigma^a}{2}H$ is non-zero only if we pick $\sigma^a = \sigma^+$, so that the new (pseudo Dirac) mass term in

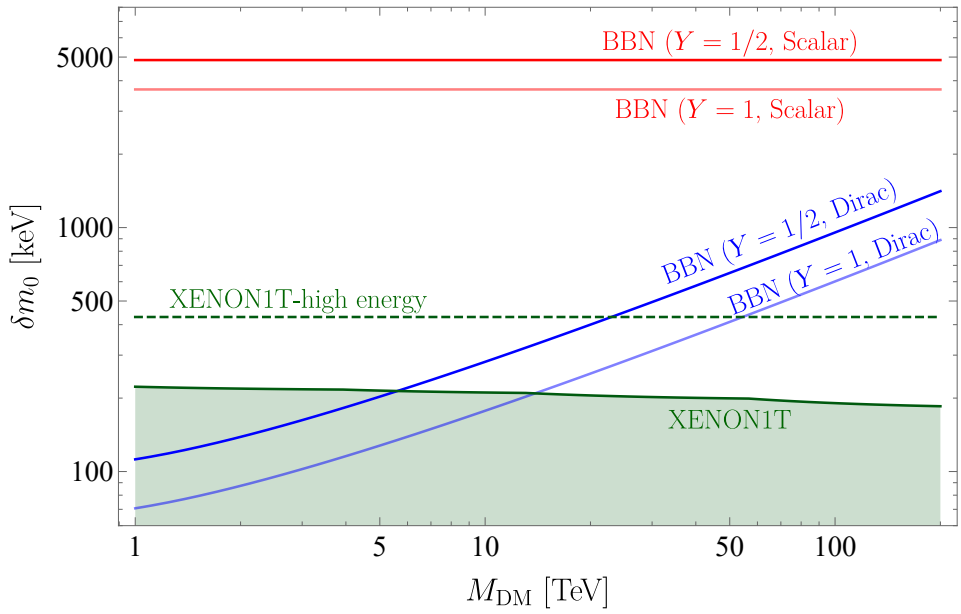

Figure 3.1: *Summary of the lower bounds on the neutral mass splitting. The* **dark green** *shaded region is excluded by tree-level Z-exchange in Xenon1T [152] for both scalar and fermionic DM. The* **dashed green** *line shows what Xenon1T could probe by analyzing high recoil energy data. The* **blue** *and* **red** *lines are the BBN bounds on the splitting for fermionic and scalar DM respectively.*

the Lagrangian reads

$$\begin{aligned} \mathscr{L}_m &= M_\chi \overline{\chi}_N \chi_N + \frac{\delta m_0}{4} \left[\overline{\chi}_N \chi_N^c + \overline{\chi^c}_N \chi_N\right], \\ \delta m_0 &= 4 y_0 c_{nY0} \Lambda_{\rm UV} \left(\frac{v}{\sqrt{2}\Lambda_{\rm UV}}\right)^{4Y} . \end{aligned} \tag{3.3}$$

$c_{nYQ} = \frac{1}{2^{Y+1}(4Y)!} \prod_{j=-Y-|Q|}^{Y-1-|Q|} \sqrt{\frac{1}{2}\left(\frac{n+1}{2}+j\right)\left(\frac{n-1}{2}-j\right)}$ contains the normalization of $\mathcal{O}_0$ and the matrix elements of the generators. The mass eigenstates are Majorana fermions, χ_0 and $\chi_{\rm DM}$, with masses $M_0 = M_\chi + \delta m_0/2$ and $M_{\rm DM} = M_\chi - \delta m_0/2$, whose coupling to the Z boson is

$$\mathscr{L}_Z = \frac{ieY}{\sin\theta_W \cos\theta_W} \overline{\chi}_0 \not{Z} \chi_{\rm DM} \, . \tag{3.4}$$

The Z-mediated scattering of DM onto nucleons is no longer elastic and the process is kinematically forbidden if the kinetic energy of the DM-nucleus system in the center-of-mass frame is smaller than the mass splitting

$$\frac{1}{2}\mu v_{\rm rel}^2 < \delta m_0 \, , \quad \mu = \frac{M_{\rm DM} m_N}{M_{\rm DM} + m_N} \, , \tag{3.5}$$

where m_N is the mass of the nucleus, μ is the reduced mass and $v_{\rm rel}$ is DM-nucleus relative velocity. In particular, given the upper bound on the relative velocity $v_{\rm rel} < v_{\rm E} + v_{\rm esc}$, where $v_{\rm E} = 240$ km/sec is the Earth's velocity and $v_{\rm esc} = 600$ km/sec

is the assumed escape velocity of DM in the Milky Way, the largest testable mass splitting is $\delta m_0^{\rm max} = 1/2\mu(v_{\rm E}+v_{\rm esc})^2$ which for xenon nuclei gives $\delta m_0^{\rm max} \simeq 450$ keV. The splitting for a given recoil energy is

$$\delta m_0(E_R) = \sqrt{2 m_N E_R}(v_{\rm E}+v_{\rm esc}) - E_R \frac{m_N}{\mu} \ , \tag{3.6}$$

which explain why the maximal constrained splitting experimentally is $\delta m_0^{\rm max,exp} \simeq 240$ keV as shown in Fig. 3.1, given that Xenon1T [152] analyzed data only for $E_R < 40$ keV. Extending the range of Xenon1T to higher recoil energies would be enough to probe splitting up to $\delta m_0^{\rm max}$ as already noticed in Ref. [148, 149].

In principle, larger mass splittings can be reached using heavier recoil targets than xenon such as iodine in PICO-60 [153], tungsten in CRESST-II [154], $CaWO_4$ [155], $PbWO_4$ [156], ^{180}Ta [157], Hf [158] and Os [159]. However, these experiments currently do not have enough exposure to probe EW cross-sections.

A complementary bound on δm_0 comes from requiring that the decay $\chi_0 \to \chi_{\rm DM}$+SM happens well before BBN. The leading decay channels are $\chi_0 \to \chi_{\rm DM}\gamma$, $\chi_0 \to \chi_{\rm DM}\bar{\nu}\nu$ and $\chi_0 \to \chi_{\rm DM}\bar{e}e$ with decay widths

$$\Gamma_\gamma = \left(1+\frac{1}{2}\log\left(\frac{m_W^2}{M_{\rm DM}^2}\right)\right)^2 \frac{Y^2\alpha_2^2\alpha_{\rm em}}{\pi^2}\frac{\delta m_0^3}{M_{\rm DM}^2} \ , \tag{3.7}$$

$$\Gamma_{\bar{\nu}\nu} \simeq 6\Gamma_{\bar{e}e} = \frac{G_F^2 \delta m_0^5 Y^2}{5\pi^3} \ . \tag{3.8}$$

The first process is induced by a dipole operator generated at 1-loop for fermionic DM as computed in [160]. The three body decays are instead induced at tree-level by the EW interactions both for fermionic and scalar DM. For fermionic DM, the dipole induce decay dominates the width in the mass range of interest. In order for these processes not to spoil BBN, we have to impose the following condition on the decay rate of χ_0:

$$\Gamma_{\chi_0} \equiv \Gamma_{\bar{\nu}\nu} + \Gamma_{\bar{e}e} + \Gamma_\gamma > \tau_{\rm BBN}^{-1} \ , \tag{3.9}$$

where $\tau_{\rm BBN}^{-1} = 6.58 \times 10^{-25}$ GeV. The lower bounds on the neutral mass splitting for fermions are shown in Fig. 3.1 together with those for scalars computed in Appendix D.2. The main difference between scalars and fermions is that the former are typically more long lived due to the suppression of $\chi_0 \to \chi_{\rm DM}\gamma$. As a consequence the BBN bouns are stronger for scalar WIMPs.

3.1.2 Charged splitting

The operator $\mathcal{O}_+$ in Eq. (3.1) is necessary to make the DM the lightest state in the EW multiplet for all the n-plets where the hypercharge is not maximal. Indeed, EW interactions induce at 1-loop mass splittings between the charged and the neutral components of the EW multiplet which in the limit $m_W \ll M_\chi$ are [95–97]

$$\Delta M_Q^{\rm EW} = \delta_g \left(Q^2 + \frac{2YQ}{\cos\theta_W}\right) \ , \tag{3.10}$$

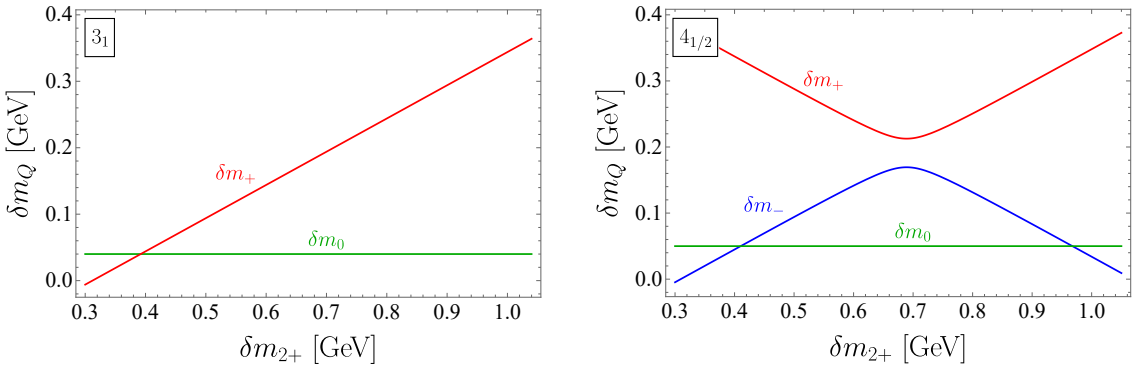

Figure 3.2: *Mass splittings of* 3_1 *(left) and* $4_{1/2}$ *(right) as a function of* δm_{2+}*. In the* 3_1 *case, no mixing between the charged components of the multiplet can occur and* δm_+ *is a monotonic function of* δm_{2+}*. In the* $4_{1/2}$ *case, instead, because of the mixing induced by* $\mathcal{O}_0$*, the positively charged mass eigenstate* χ^+ *is always heavier than* χ^-*. The splitting between* χ^+ *and* χ^- *has a minimum of order* δm_0*, which was taken 50 MeV in this plot for display purposes.*

where $\delta_g = (167 \pm 4)$ MeV and $Q = T_3 + Y$. This implies that negatively charged states with $Q = -Y$ are pushed to be lighter than the neutral ones by EW interactions. Notable exceptions are odd-n multiplets with $Y = 0$ and all the multiplets with maximal hypercharge $|Y_{\rm max}| = (n-1)/2$ where negatively charged states are not present. For these multiplets, having $y_+ = 0$ would be the minimal and phenomenologically viable choice.

Including the contribution of $\mathcal{O}_+$, the final splittings $\delta m_Q = M_Q - M_{\rm DM}$ between the DM and the charged components read

$$\delta m_Q = \frac{\delta m_0}{2} + \delta_g Q^2 + \mathrm{sgn}(Q)\sqrt{\left(\frac{2Y\delta_g}{\cos\theta_W} - \frac{y_+ v^2}{4\Lambda_{\rm UV}}\right)^2 Q^2 + \frac{\delta m_0^2}{4}\frac{c_{nYQ}^2}{c_{nY0}^2}}\,, \tag{3.11}$$

where $\mathrm{sgn}(Q)$ in Eq. (3.11) accounts for the presence of opposite charge states that are not related by charge conjugation, as implied by to the non-zero hypercharge of our WIMPs. The second term inside the square root comes from the mixing between the charged gauge eigenstates χ_Q and χ^c_{-Q} induced by $\mathcal{O}_0$. This obviosuly vanishes for $Q > (n-1)/2 - Y$.

The different charged-neutral mass splittings can all be written in terms of two independent splittings, which we choose to be δm_0 and δm_{Q_M}, where $Q_M \equiv Y + (n-1)/2$ is the largest electric charge in the multiplet. Since $c_{nYQ_M} = 0$, δm_{Q_M} is a monotonic function of y_+ and Eq. (3.11) can be inverted. In Fig. 3.2 we show as an example the mass splittings of 3_1 and $4_{1/2}$ as a function of δm_{2+}. In the former case, no mixing occur within the components of the multiplet and δm_+ is a monotonic function of δm_{2+}. For the $4_{1/2}$, instead, the mixing induced by $\mathcal{O}_0$ between the components with $Q = \pm 1$ makes the positively charged mass eigenstate χ^+ heavier than χ^-.

In Sec. 3.4 we will explore the parameter space spanned by δm_0 and δm_{Q_M}, fixing the thermal DM mass of every EW multiplet as shown in Table 3.1. Crucially,

the operators inducing the splitting in Eq. (3.1) also generate new higgs-exchange contributions to the spin-independent scattering cross-section of DM on nucleons. Therefore, the current best upper limit on the DM elestic cross section onto nucleons set by PandaX-4T [53] translates into upper bounds on the neutral and charged splittings as reported in Table 3.1.

Charged-neutral splittings smaller than the EW one in Eq. (3.10) require a certain amount of fine-tuning between UV operators and the EW contribution. To quantify this we define the Fine Tuning (F.T.)

$$\text{F.T.} \equiv \max_I \left[\frac{\mathrm{d} \log \delta m_Q}{\mathrm{d} \log \delta m_I} \right] , \tag{3.12}$$

where the index I runs over the three contributions in the definition of δm_Q in Eq. (3.11). Large values of F.T. imply a significant amount of cancellation between two or more parameters.

3.1.3 Viable complex WIMPs

The EFT approach used to write Eq. (3.1) is meaningful only if the UV physics generating $\mathcal{O}_+$ and $\mathcal{O}_0$ is sufficiently decoupled from DM. When $\Lambda_{\rm UV}$ approaches the DM mass the cosmological evolution of the DM multiplet cannot be studied in isolation, since the heavy degrees of freedom populates the thermal bath at $T \simeq M_{\rm DM}$ and are likely to modify our freeze-out predictions. To avoid these difficulties we restrict ourselves to $\Lambda_{\rm UV} \geq 10 M_{\rm DM}$.

This condition, together with the required inelastic splittings in Fig. 3.1, can be used to select the viable complex WIMPs. Starting from Eq. (3.3) and imposing $\delta m_0 > \delta m_0^{\rm min}$, we derive the viable window for $\Lambda_{\rm UV}$:

$$10 M_{\rm DM} < \Lambda_{\rm UV} \leq \left(\frac{4 y_0 c_{nY0} v^{4Y}}{2^{2Y} \delta m_0^{\rm min}} \right)^{\frac{1}{4Y-1}} . \tag{3.13}$$

We are now interested in estimating for which multiplets the viable window shrinks to zero. Setting $y_0 = (4\pi)^{4Y}$ in Eq. (3.13) that is the largest value allowed by Naive Dimensional Analysis (NDA) we derive the values of n and Y having a non zero cutoff window in Eq. (3.13). These are for both scalar and fermionic WIMPs $n_{1/2}$ multiplets with $n \leq 12$ together with the 3_1 and the 5_1 mupltiplets.

This result can be understood as follows. The upper bounds on n for $Y = 1/2$ multiplets come from the perturbative unitarity of the annihilation cross section as discussed in Appendix 2.3. The maximal cutoff required to obtain the phenomenologically viable splittings is of order $\sim 10^7$ TeV as shown in the fifth column of Table 3.1. This is many orders of magnitude larger than the DM masses allowed by freeze-out so that Eq. (3.13) results in a wide range of allowed $\Lambda_{\rm UV}$.

For $Y = 1$ multiplets the maximal required cutoff is of order $\sim 10^2$ TeV so that the n-dependence of the allowed window in Eq. (3.13) becomes relevant. Given that the DM mass grows with n as $M_{\rm DM} \sim n^{5/2}$ and the required cutoff stay approximately

constant, we expect the allowed window to shrink to zero for large n. Numerically we find that the last allowed multiplet has $n = 5$.

We refer to Appendix D.2 for a similar argument for scalar WIMPs. These have a slightly different parametric which however results in the same viable EW multiplets of the fermionic case.

3.1.4 DM stability

The Lagrangian in Eq. (3.1) preserves the DM number and as a consequence the DM is automatically stable. Gauge invariant interactions beyond those of Eq. (3.1) can however induce fast DM decay. Here we discuss whether the effect of these operators can be small enough to allow the DM to be accidentally stable. Throughout this discussion we not only require the DM lifetime to be long enough to circumvent cosmological bounds [103, 104] ($\tau_{\rm DM} \gtrsim 10^{19}$ sec) but also to satisfy the stronger astrophysical bounds on decaying DM [94, 105, 106] ($\tau_{\rm DM} \gtrsim 10^{28}$ sec).

For $2_{1/2}$ and 3_1 we can write renormalizable interactions $\overline{\chi^c} H e_R$ and $\overline{\chi} L^c H$ that break the DM number and lead to a fast DM decay. These EW multiplets require a DM number symmetry, for example a discrete $\mathbb{Z}_2$-symmetry acting only on the DM field to provide a viable DM candidate.

For even multiplets with $Y = 1/2$ and $n > 2$, we can write the following series of higher dimensional operators inducing DM decay

$$\begin{aligned}\mathscr{L}_{\rm even} = &\frac{C_1}{\Lambda_{\rm UV}^{n-3}}\overline{L^c}\chi(H^\dagger H)^{\frac{n-2}{2}} + \frac{C_2}{\Lambda_{\rm UV}^{n-3}}\overline{L^c}\chi W_{\mu\nu}W^{\mu\nu}(H^\dagger H)^{\frac{n-6}{2}} + \frac{C_3}{\Lambda_{\rm UV}^{n-3}}\overline{L^c}\chi(W_{\mu\nu}W^{\mu\nu})^{\frac{n-2}{4}} \\ &+ \frac{C_4}{\Lambda_{\rm UV}^{n-3}}\overline{L^c}\sigma^{\mu\nu}\chi W_{\mu\nu}(H^\dagger H)^{\frac{n-4}{2}} + \frac{C_5}{\Lambda_{\rm UV}^{2}}\overline{\chi}\chi^c\overline{L^c}\chi\ ,\end{aligned} \tag{3.14}$$

where the Higgs bosons are appropriately contracted to make every term an $SU(2)$ singlet. For $4_{1/2}$, the leading contribution to DM decay comes from the operators with coefficients C_1 and C_4, while for $n \geq 6$ this is given by the operator with coefficient C_5 by closing the χ loop and attaching $(n-2)/2$ $W^{\mu\nu}$ operators, in a similar fashion to real candidates [83]. In all cases, we need at least $\Lambda_{\rm UV} > 10^{10} M_{\rm DM}$ for $\mathcal{O}(1)$ Wilson coefficients to preserve DM stability. This lower bound is incompatible with the upper bound on the UV physics scale required to generate the inelastic splitting δm_0. This result implies that the DM stability depends upon the properties of the UV physics generating the neutral splitting in Eq. (3.3).

For the 5_1 WIMP the lowest dimensional operators inducing DM decay are

$$\mathscr{L}_5 = \frac{C_1}{\Lambda_{\rm UV}^2}(\overline{\chi}L^c H)(H^\dagger H) + \frac{C_2}{\Lambda_{\rm UV}^2}(\overline{\chi}\sigma^{\mu\nu}L^c H)W_{\mu\nu}. \tag{3.15}$$

These require $\Lambda_{\rm UV} > 10^{10} M_{\rm DM}$ to ensure DM accidental stability which is again incompatible with the upper bound of $\Lambda_{\rm UV} < 20 M_{\rm DM}$ needed to generate the inelastic splitting.

As a result, none of the complex WIMPs with $Y \neq 0$ can be accidentally stable in the sense of Minimal Dark Matter [23]. Specific UV completions of the physics generating the inelastic splitting in Eq. (3.3) might allow for DM accidental stability. This question goes beyond the scope of this study. Conversely, complex WIMPs with $Y = 0$ can be accidentally stable thanks to the gauging of the unbroken $U(1)$ flavor symmetry in the DM sector [35]. The freeze-out predictions for these millicharged WIMPs are given in Appendix E.

3.2 Complex WIMP cosmology

In this Section, we briefly describe the cosmological evolution of the Complex WIMP candidates. In particular, we highlight the main differences with respect to real WIMPs discussed in Chapter 2.

3.2.1 Sommerfeld Enhancement and Bound State Formation

At small velocities and in the symmetric limit, the Sommerfeld enhancement for Complex EW WIMPs can be approximated as

$$S_E^I \approx \frac{2\pi\alpha_{\rm eff}}{v_{\rm rel}} \,, \tag{3.16}$$

where now $\alpha_{\rm eff} = \alpha_2(I^2 + 1 - 2n^2)/8 + Y^2\alpha_Y \equiv \alpha_{2,\rm eff} + Y^2\alpha_Y$ includes also the contribution coming from the non-zero hypercharge. With this replacement, the annihilation cross-section takes the form as in the real case in Eq. (2.16):

$$\langle \sigma_{\rm ann}^{\rm SE} v_{\rm rel} \rangle = \sum_I \langle S_E^I \sigma_{\rm ann}^I v_{\rm rel} \rangle \,, \tag{3.17}$$

where $\sigma_{\rm ann}^I$ is the perturbative, s-wave, hard annihilation cross-section in the isospin channel I. We account for the mistake done neglecting p-wave contribution as in Eq. (2.18). The $SU(2)_L$ symmetric limit approximate better the exact result the more we increase the dimensionality of the EW multiplet. This is because most of the freeze-out dynamics for large n-plets occurs before the EWSB. For smaller multiplets the symmetric approximation generically fails because EWSB become important. In our computation, we always assume the symmetric limit for $n \geq 6$, while we compute the SE in the broken phase for smaller multiplets.

Besides, the mass splittings generated by $\mathcal{O}_0$ and $\mathcal{O}_+$ can alter the pattern of resonances in the SE, so that the thermal mass becomes a function of δm_0 and δm_+ as well. In Table 3.1 we assume the minimal δm_0, where the effect of the splitting is safely negligible, and account for the dependence on δm_+ in the theoretical uncertainty. More details about the effect of these UV operators are discussed in Sec. 3.2.2.

Concerning BSF, the main difference with respect to real WIMPs is the different selection rules selecting the bound states allowed by symmetries. In the real case, the bound states are of the form $\chi\chi$ and the (anti-)symmetry of the wave function

allows only for those BS satisfying $P_{\rm BS} \equiv (-1)^{L+S+\frac{I-1}{2}} = 1$, while for complex WIMPs the bound states are of the form $\overline{\chi}\chi$ and the above selection rule no longer applies.
The BSF cross-section can be computed in the $SU(2)_L$ symmetric limit with good approximation and scales as:

$$\sigma_{B_I} v_{\rm rel} \simeq \frac{E_{B_I} a_B}{M_{\rm DM} n^2} (\alpha_{2,\rm eff} S_E^{I\pm 2} + Y^2 \alpha_Y S_E^I) \ , \tag{3.18}$$

where the first and second term account for weak and hypercharge vector boson emmission, respectively, $E_{B_I} \approx \alpha_{\rm eff}^2 M_{\rm DM}/4n_B^2$ - n_B being the energy level - is the binding energy and $a_B = 1/\alpha_{\rm eff} M_{\rm DM}$ the Bohr radius.
Once the BS is formed, it can annihilate into SM, decay to lower lying BS, both with rate $\Gamma \approx \alpha_{2,\rm eff}^2 \alpha_{\rm eff}^3 M_{\rm DM}$ or $Y^2 \alpha_Y^2 \alpha_{\rm eff}^3 M_{\rm DM}$, depending on the mediator, or be broken by the interactions with the plasma (ionization). The ionization rate limits the efficiency of DM annihilation through BSF and it is Boltzmann suppressed as $\sim e^{E_{B_I}}/T$. The Boltzmann suppression gets bigger as we increase the dimensionality of the multiplet, due to the larger binding energies, so that neglecting BS ionizations is a good approximation for large EW multiplets. Under this approximation, we write the overall DM effective annihilation cross-section as follows:

$$\langle \sigma_{\rm eff} v_{\rm rel} \rangle \equiv \langle \sigma_{\rm ann}^{\rm SE} v_{\rm rel} \rangle + \sum_{B_J} \langle \sigma_{B_J} v_{\rm rel} \rangle, \tag{3.19}$$

that is, once a BS is formed it eventually annihilates to SM without being destroyed. In Chapter 2 we checked the validity of this approximation for $n \leq 7$ and found that it overestimates the thermal mass of about 5 TeV. We assume this holds also for complex WIMPs and include this uncertainty in the estimate of our theoretical uncertainty, see also Ref. [161]. In the symmetric limit the effect of the mass splittings generated after EWSB are not taken into account. We expect these to make the heavier components of the multiplet decouple earlier than the lighter ones, thus reducing the cross-section. In order to estimate the error due to this approximation, we compute the thermal mass first setting to zero σ_{B_I} for $T < \max \delta m_Q$ and then including BSF until the DM abundance saturates. These two effects are the dominant sources of error for $n \lesssim 8$. Instead, for $n \gtrsim 8$, the theoretical uncertainty is dominated by NLO corrections to the potential controlling the SE as in Eq. (2.24).

3.2.2 Impact of mass splittings

Here we discuss under which conditions the effect of the UV splittings can be neglected in the prediction of the thermal mass. The UV splittings can affect the freeze-out computation in two ways: i) they directly contribute to the DM annihilation cross-section into Higgs bosons, ii) after the EWSB, the interaction Eq. (3.28) generates a Higgs-mediated Yukawa potential, thus affecting the Sommerfeld enhancement. For definiteness, we focus on fermionic WIMPs and on the $\mathcal{O}_0$ contributions. We checked that similar conclusions hold for scalar WIMPs and for the contrbutions from $\mathcal{O}_+$.

For $Y = 1/2$ WIMPs, the hard annihilation cross-section into higgses induced by $\mathcal{O}_0$ can be estimated as

$$\sigma_{2H} v_{\rm rel} \simeq \frac{3 y_{0,+}^2}{32 n^2 \pi \Lambda_{\rm UV}^2} T_R \,, \tag{3.20}$$

where $T_R = n(n^2-1)/16$ is the Dynkin index of the DM $SU(2)_L$ representation. This should be compared with the typical EW hard cross-section, which is

$$\sigma_{\rm EW} v_{\rm rel} \simeq \frac{\pi \alpha_2^2 (n^2-1)^2}{32 n M_{\rm DM}^2} \,. \tag{3.21}$$

The condition $\sigma_{2H}/\sigma_{\rm EW} < 1$ can be translated into an upper bound on the mass splittings. For instance for the inelastic mass splitting we get

$$\delta m_0 < 1.6 \text{ GeV} \left(\frac{1 \text{ TeV}}{M_{\rm DM}} \right) n^2 \,. \tag{3.22}$$

Since $M_{\rm DM} \sim n^{5/2}$ we get stronger upper bound on the splitting for large multiplets. All in all, we do not expect significant changes in the picture presented in Sec. 3.4 even though for large splittings (above 1 GeV) one can get $\mathcal{O}(1)$ effects on the thermal freeze-out predictions for small multiplets.

For $Y = 1$ the contribution from $\mathcal{O}_0$, which now is a 7D operator which controls the 4-body process $\overline{\chi}\chi \to 4H$ whose cross section can be estimated as

$$\sigma_{4H} v_{\rm rel} \approx \frac{\pi y_0^2 M_{\rm DM}^4}{(16\pi^2)^3 \Lambda_{\rm UV}^6} \frac{(n^2-1)^2}{64 n} \,. \tag{3.23}$$

The condition $\sigma_{4H}/\sigma_{\rm EW} < 1$ translates into

$$\delta m_0 < 0.45 \text{ GeV} \left(\frac{1 \text{ TeV}}{M_{\rm DM}} \right)^3 n^2, \tag{3.24}$$

which, for $n = 3, 5$ is much looser than the upper bound on δm_0. As a consequence, the UV splittings do not impact the freeze-out prediction for $Y = 1$ WIMPs.

Finally, concerning the contribution to the Sommerfeld enhancement, the potential arising from the Yukawa interaction in Eq. (3.28) is:

$$V_H(r) = -\left(\frac{\lambda_D v}{8\pi \Lambda_{\rm UV}} \right)^2 \frac{e^{-m_h r}}{r}. \tag{3.25}$$

Such potential is shorter range with respect to typical EW Yukawa potentials, due to the larger Higgs mass as compared to weak boson masses. We find that $V_H(r)$ is negligible compared to the size of the EW potential α_2/r for the mass splittings of our interest.

3.3 Minimal Splitting

In this section we discuss the DD signal of Complex WIMPs in the minimal splitting scenario, that is when the mass splittings are chosen to be the smallest possible allowed by the requirements of the previous section. For fermions, we set $\delta m_0 = 220$ keV for $n_{1/2}$ WIMPs with $n \leq 4$ as well as for the allowed n_1 WIMPs. For $n_{1/2}$ WIMPs with $n > 4$ the BBN bound in Fig. 3.1 gives the minimal δm_0. For scalars instead, we set $\delta m_0 = 4.9$ MeV for $n_{1/2}$ and $\delta m_0 = 3.7$ MeV for n_1 WIMPs, both coming from BBN.

In this minimal setup, $2_{1/2}$ and 3_1 stand out as the only two multiplets where the DM is automatically the lightest state, with a splitting with the $Q = 1$ state given by the pure EW splitting in Eq. (3.10) that is 354 MeV for $2_{1/2}$ and 542 MeV for 3_1. For all the other WIMPs a UV generated splitting is needed to make the DM lighter than the negatively charged states. We fix this splitting to the smallest possible value that gives the DM as the lightest state. As can be seen from Eq. (3.11) this requires a UV splitting which is of the order of the EW one. We want now to study the phenomenology in direct detection in Sec. 3.3.1 and at a future muon collider in Sec. 3.3.2.

3.3.1 Direct Detection prospects

The spin independent scattering cross-section $\sigma_{\rm SI}$ of DM on nuclei receives two contributions: i) from purely EW loop diagrams ii) from Higgs mediated tree-level diagrams generated by both $\mathcal{O}_0$ and $\mathcal{O}_+$. For minimal splitting Higgs mediated scattering is subdominant and $\sigma_{\rm SI}$ can be computed by considering only EW loop diagrams.

In this case, the Lagrangian describing the spin-independent (SI) DM interactions with quarks and gluons is again the one written in Eq. (2.52). The Wilson coefficients now are given by [32]

$$
\begin{aligned}
f_q^{\rm EW} &\simeq -\frac{\pi\alpha_2^2}{16 m_h^2 m_W}\left[n^2-1-\left(1.03+22(a_q^{V,2}-a_q^{A,2})\right)Y^2\right], \\
g_q^{\rm EW} &\simeq \frac{\pi\alpha_2^2}{24 m_W^3}\left[n^2-1-\left(4-18.2(a_q^{V,2}+a_q^{A,2})\right)Y^2\right], \\
f_G^{\rm EW} &\simeq \frac{\alpha_s\alpha_2^2}{192 m_h^2 m_W}\left[\left(\sum_{q=c,b,t}\kappa_q+2.6\right)(n^2-1)-\left(1.03\sum_{q=c,b,t}\kappa_q-7.5\right)Y^2\right],
\end{aligned}
\tag{3.26}
$$

where $a_q^V = T_{3q}/2 - Q_q s_w^2$, $a_q^A = -T_{3q}/2$ with c_w, s_w being the cosine and the sine of the Weinberg angle, respectively. The terms proportional to Y correspond to the exchange of Z bosons inside the EW loops.

The direct detection reach on the different complex multiplets for minimal splitting is summarized in Fig. 3.3. As can be seen by the figure, most of the WIMPs can be

probed for minimal splitting by future large exposure direct detection experiments like DARWIN with the notable exception of the $2_{1/2}$ and 5_1 that we discuss below.

Combining Eq. (3.26) with Eq. (2.56) the parametric expression for $\sigma_{\rm SI}$ is

$$\sigma_{\rm SI} \approx 10^{-49}\ {\rm cm}^2 (n^2 - 1 - \xi\, Y^2)^2, \tag{3.27}$$

where $\xi = 16.6 \pm 1.3$ with the error coming from the lattice determination of the nucleon form factors. This formula makes evident that large cancellations with respect to the natural size of the elastic cross section can take place when $Y \simeq \sqrt{(n^2-1)/\xi}$. In particular, for $n = 2$ the exact cancellation takes place at $Y \simeq 0.44 \pm 0.02$, which almost matches the exact hypercharge of the doublet leading to the large uncertainty in Fig. 3.3. Similarly, the cancellation happens at $Y \simeq 1.2$ for $n = 5$, which explains why in this case the signal entirely lies below the neutrino floor, while it is within DARWIN reach for their real or millicharged counterparts as shown in Fig 2.11 and Fig. E.1, respectively.

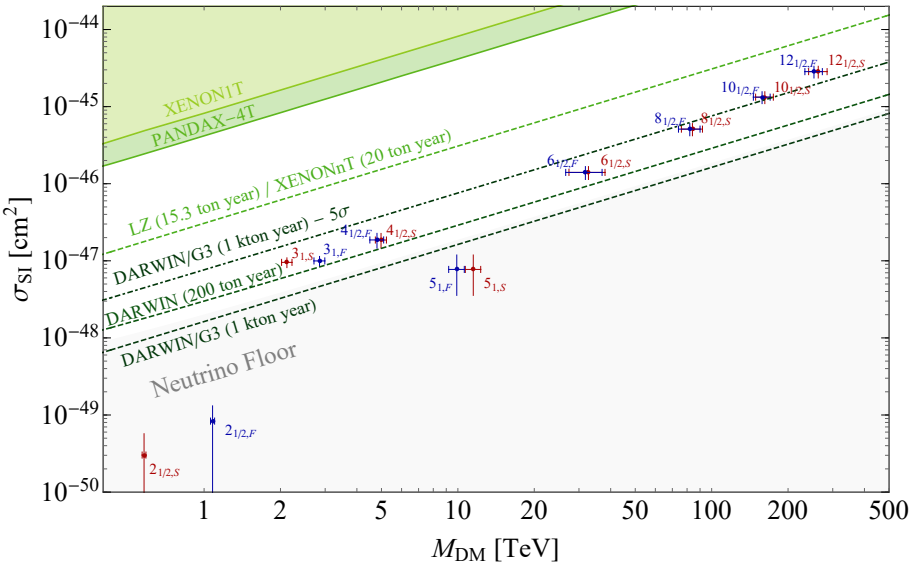

Figure 3.3: *Expected SI cross-sections for different complex WIMPs for minimal splitting as defined in Sec. 3.3. The* **blue dots** *correspond to Dirac WIMPs and the* **red dots** *to complex scalar WIMPs. The vertical error bands correspond to the propagation of LQCD uncertainties on the elastic cross-section (Eq. (2.56)), while the horizontal error band comes from the uncertainty in the theory determination of the WIMP freeze out mass in Table 3.1. The* **light green** *shaded region is excluded by the present experimental contraints from XENON-1T [52] and PandaX-4T [53], the* **green dashed** *lines shows the expected 95% CL reach of LZ/Xenon-nT [54, 55] and DARWIN [41, 50].*

Spin dependent (SD) interactions of DM with the nuclei are also induced by EW loops and can lead to a larger cross section compared to the SI one [32]. Unfortunately, the predicted SD cross section for all the complex WIMPs lies always well below the neutrino floor and it will be impossible to test even at future direct detection experiments.

3.3.2 Collider Searches

Conversely to the case of real WIMPs, large exposure experiments like DARWIN will not be able to entirely close the window of Complex WIMP candidates. This further motivates us to study the expected reach on these DM candidates at a high energy lepton collider such as a muon collider running well beyond TeV center of mass energy.

In this Section we first fix the luminosity as in Eq. (2.26) and we concentrate on machines running at $\sqrt{s} = 3, 6, 10$ TeV [118, 151]. We then provide estimates for scenarios in which the luminosity is a free parameter not fixed by Eq. (2.26). We will comment on resonant BS production, which require the COM energy to be tuned around the BS mass, at the end of Sec. 3.4.2.

The most compelling candidates for collider searches are the complex doublet ($2_{1/2}$) and the complex triplet (3_1), that are the lightest WIMPs and have greater chances to be discovered at $\sqrt{s} \leq 10$ TeV. Theoretically, these candidates are the most minimal complex WIMPs since they have maximal hypercharge and the neutral component is automatically the lightest one at the renormalizable level. The only required higher dimensional operator is $\mathcal{O}_0$ which generates the inelastic splitting in Eq. (3.3). We also briefly discuss the sensitivity of high energy muon colliders to heavier multiplets, namely the $4_{1/2}$ and the 5_1. Finally, as in Chapter 2, we focus on fermions, postponing the discussion on scalars to Appendix F.

The expected signatures at future colliders depend very much on the lifetime of the charged states in the EW multiplet. These might decay back to the neutral DM either promptly or with a macroscopic lifetime on detector scales.

In the prompt case, the decay of the charged state will give rise to soft radiation which would be impossible to disentangle from the SM background and the DM signal will be characterized only by a large missing energy recoiling against EW radiation. This can be further resolved from the SM background at lepton colliders thanks to the knowledge of the center of mass energy by looking for features in the MIM distribution. For the MIM searches we have proceeded similarly to Section 2.4 and optimized the selection for the fermion $2_{1/2}$ and 3_1 at $\sqrt{s} = 3, 6$ TeV and $\sqrt{s} = 6, 10$ TeV, respectively. For the other candidates we used the optimal cuts that we derived from our previous results on real candidates. For each level of systematics ϵ we have interpolated our previous results as functions of n and $\sqrt{s}$ and derived optimal cuts for the new $n-$plets studied in this Chapter. We remark that this procedure is potentially inaccurate as the real odd $n-$plets contain 2 times fewer degrees of freedom, hence have rates smaller by a factor 2. This can in principle affect the result of the optimization of the selection. We checked that the difference with a dedicated optimization is negligible, thus our event selection should be quite close to the optimal one. Following the mono-W discussion in Sec. 2.4.1, we have computed the background rate with MadGraph5_aMC@NLO using the full 3-body process for $\eta \lesssim 6$, and matched it to a computation using the Weizsäcker-Williams approximation for larger values of pseudorapidity.

In the long-lived case, depending on the decay length of the charged state it might

be beneficial to look at disappearing or "stub" tracks (DT) as studied in Ref. [68], or at long-lived charged tracks that could be distinguished from the SM backgrounds by their energy losses in the material and by the measurement of their time of flight (see for example analogous searches performed by ATLAS and CMS at the LHC [162, 163]).

We show detailed results for the combination of the MIM and DT searches for fixed thermal mass of the $2_{1/2}$ and the 3_1 in Fig. 3.4. For the MIM searches, we fix the splitting of the $Q = 1$ state with respect to the neutral one to be the one generated purely by EW corrections. In this minimal case the rest-frame lifetime of the charged state decaying back to the DM is $c\tau_+ \approx 6.6$ mm for the $2_{1/2}$ and $c\tau_+ \approx 0.75$ mm for the 3_1. As can be seen from Fig. 3.4, the MIM search at $\sqrt{s} = 3$ TeV with the benchmark luminosity $\mathcal{L} = 1$ ab^{-1} is not sensitive to the $2_{1/2}$. A $\sqrt{s} = 6$ TeV collider with benchmark luminosity $\mathcal{L} = 4$ ab^{-1}, instead, is able to probe the doublet WIMP at 2σ C.L. In general the mono-W and mono-γ channels give comparable mass reach for the benchmark luminosity adopted here.The sensitivity of each channel has a specific behavior as a function of the luminosity and for different assumed systematics. The overall combination as function of the total luminosity for fixed thermal mass is shown in Fig. 3.4. We remark that the reach deviates from a pure rescaling by $\sqrt{\mathcal{L}}$ because the selections, hence the result, have been optimized as a function of $\mathcal{L}$ when dealing with $\epsilon_{\rm sys} \neq 0$.

In Fig. 3.4 we also display results for the DT search as a function of the lifetime of the charge $+1$ state, that is in a 1-to-1 relation with the mass splitting δm_+. We see that a collider of $\sqrt{s} = 6$ TeV can probe the $2_{1/2}$ for charge-neutral splitting generated purely by EW interactions. A collider of $\sqrt{s} = 3$ TeV can probe a large portion of the allowed lifetimes for the charged tracks corresponding to non-zero UV contributions in Eq. (3.11). It is important to notice that with an $\mathcal{O}(1)$ fine tuning of the UV contribution to the charged neutral splitting against the irreducible EW contribution the charged tracks could be extremely long-lived on detector scale for both the $2_{1/2}$ and 3_1. This observation motivates a detailed detector simulation of a muon collider environment to reliably estimate the expected reach in this channel. We will provide some estimates for the signal yield in Fig. 3.8 in the next section.

In Fig. 3.4 we show similar results for the 3_1 at its thermal mass, which entails interesting results at 6 and 10 TeV center of mass energy machines. For the 10 TeV collider we find that MIM searches are effective probes of this WIMP candidate and can establish a bound at 95% CL with a small luminosity or give a discovery with the nominal luminosity. Mono-W and mono-γ perform similarly well and their combination is worth being done. The DT search cannot probe the EW splitting for the 3_1, however it can cover a large portion of allowed lifetimes in the non-minimal case in which UV physics is contributing to the charged-neutral splitting.

We report in Fig. 3.5 the detailed sensitivities of the different collider searches for the $2_{1/2}$, 3_1, $4_{1/2}$, 5_1, at colliders with suitable $\sqrt{s}$ that can provide 95% C.L. exclusion. In general, we find that the MIM reach is dominated by the mono-W and the mono-γ channels, which show similar sensitivities. Despite the non-zero hypercharge enhancing the coupling to the Z, the mono-Z channel has a lower reach, similarly

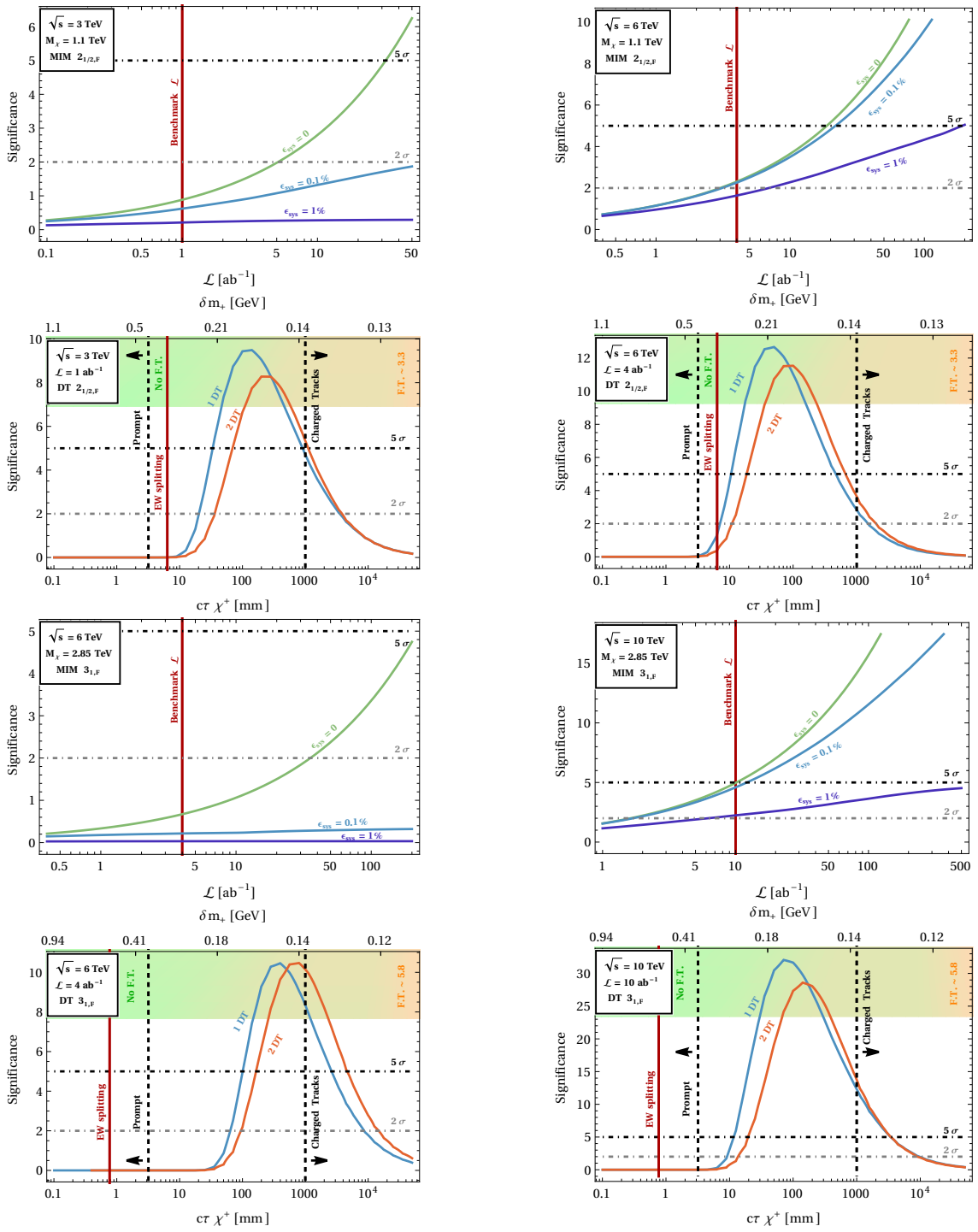

Figure 3.4: Top two rows: *Collider reach for the* $2_{1/2}$ *of mass* $M_\chi = 1.1$ *TeV and* $\sqrt{s} = 3$ *TeV (left) and* $\sqrt{s} = 6$ *TeV (right). Upper row: Combined reach for MIM (mono-*γ*+mono-W) as a function of the luminosity* $\mathcal{L}$ *for different value of the expected systematic uncertainties parametrized by* ϵ_{sys}*:* 1% **(purple)**, 0.1% **(cyan)**, *0* **(green)**. *The* **red** *lines show the benchmark luminosity following Eq. (2.26). Lower row: Reach of DT for varying lifetime of the charged track. The* **red** *vertical line shows the benchmark lifetime for EW splitting. The* **blue** *and* **orange** *curves correspond to the reach with 1 and 2 disappearing tracks. Fine-Tuning values computed on* δm_+ *following Eq. (3.12) are displayed as color code from green (no fine-tuning) to red (higher fine-tuning).* **Bottom two rows**: *same as for the top rows, but for the case of the* 3_1 *of mass* $M_\chi = 2.85$ *TeV and* $\sqrt{s} = 6$ *TeV (left) and* $\sqrt{s} = 10$ *TeV (right).*

to what was found in the real case.

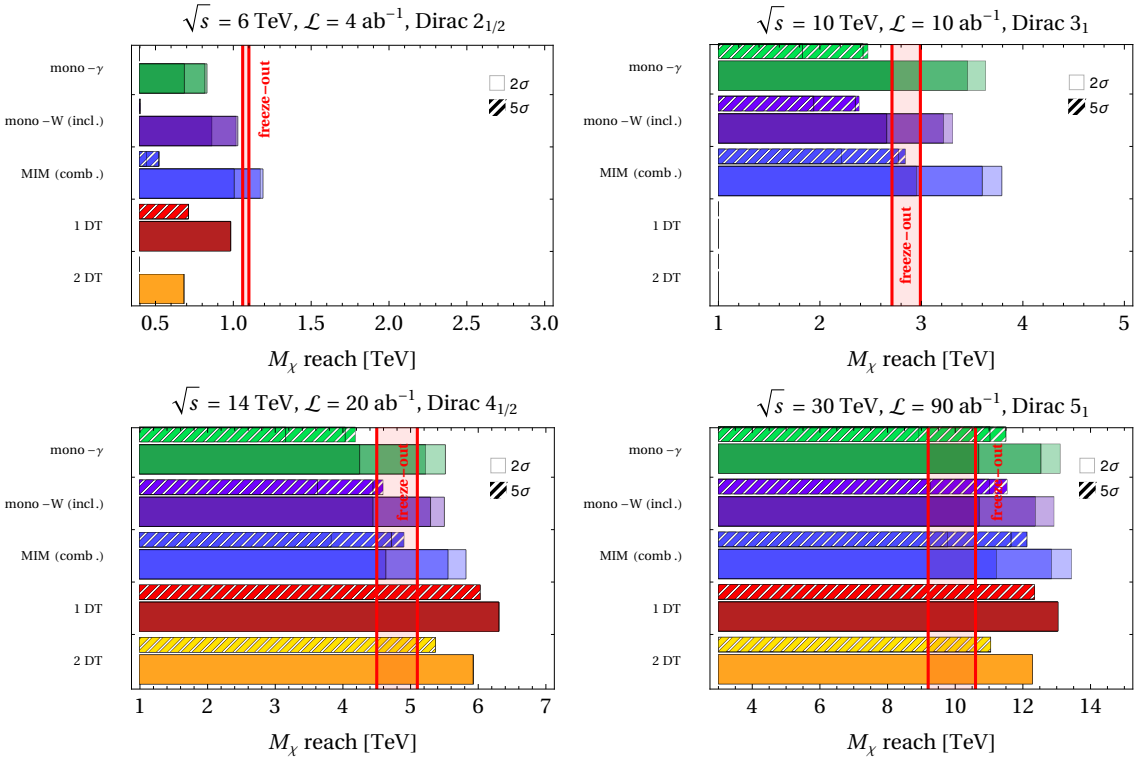

Figure 3.5: *Different bars show the 2 σ(solid wide) and 5σ (hatched thin) reach on the fermionic WIMP mass at a muon collider for different search channels. The first three bars show the channels discussed in Sec. 3.4 where DM would appear as missing invariant mass (MIM) recoiling against one or more SM objects: mono-γ, inclusive mono-W, and the combination of all these MIM channels (blue). The mono-Z channel is not reported since it gives results below the minimum mass shown. The last two bars show the reach of disappearing tracks, requiring at least 1 disappearing track (red), or at least 2 tracks (orange). All the results are shown assuming systematic uncertainties to be 0 (light), 1‰(medium), or 1% (dark). The vertical red bands show the freeze-out prediction. Tracks have been computed assuming minimally split neutral states, and a charged-neutral splitting δm_+ equal to the gauge contribution for the $2_{1/2}$ and 3_1. For the $4_{1/2}$ and 5_1 the splitting-inducing couplings y_0 and y_+ have been tuned so that $\delta m_+ = \delta m_-$ (up to minimal δm_0 corrections), which represents a least favorable condition for DT searches.* ***Top Left:*** *Dirac $2_{1/2}$ for $\sqrt{s} = 6$ TeV and $\mathcal{L} = 4$ ab^{-1}.* ***Top Right:*** *Dirac 3_1 for $\sqrt{s} = 10$ TeV and $\mathcal{L} = 10$ ab^{-1}.* ***Bottom Left:*** *Dirac $4_{1/2}$ for $\sqrt{s} = 14$ TeV and $\mathcal{L} = 20$ ab^{-1}.* ***Bottom Right:*** *Dirac 5_1 for $\sqrt{s} = 30$ TeV and $\mathcal{L} = 90$ ab^{-1}.*

Results for generic center-of-mass energy and integrated luminosity are displayed in Figs. 3.6 and 3.7 for the mono-γ and mono-W channels. The results on this figure have been obtained by rescaling the results at $\sqrt{s} = 3, 6, 10, 14, 30$ TeV, under the assumption that all cross-sections and kinematical cuts scale trivially with collider energy, and neglecting systematic errors.

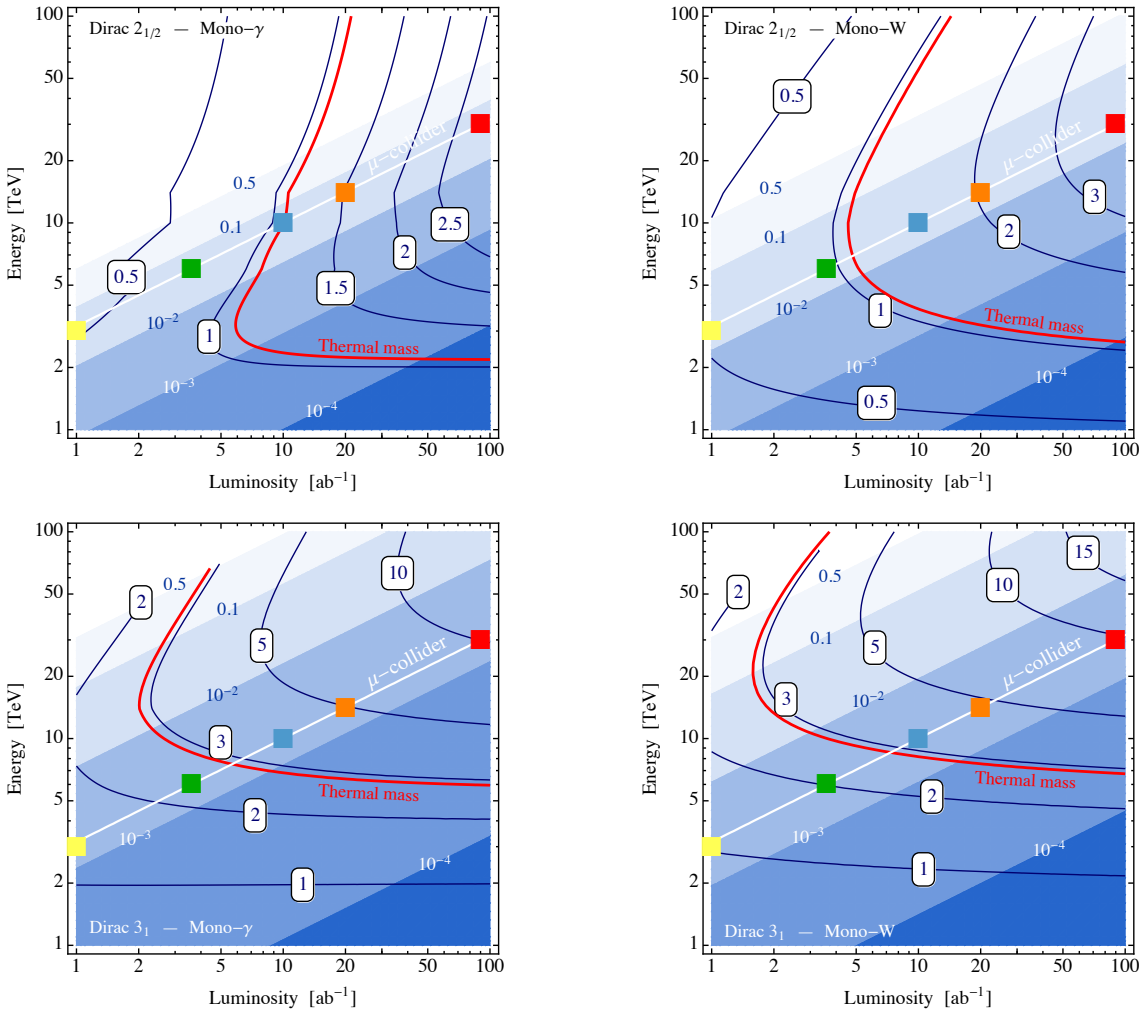

Figure 3.6: *Mass reach (in TeV) in the mono-γ and mono-W channels as a function of collider center-of-mass energy and luminosity, for Dirac fermion doublets and triplets(blue lines). The thermal freeze-out mass is shown in red. Blue shades show the expected values of the ratio of the signal rate over background. Systematic uncertainties are set to zero. The muon collider luminosity Eq. (2.26) is shown as a white line, with the benchmark values of $\sqrt{s}$ highlighted by the colored squares.*

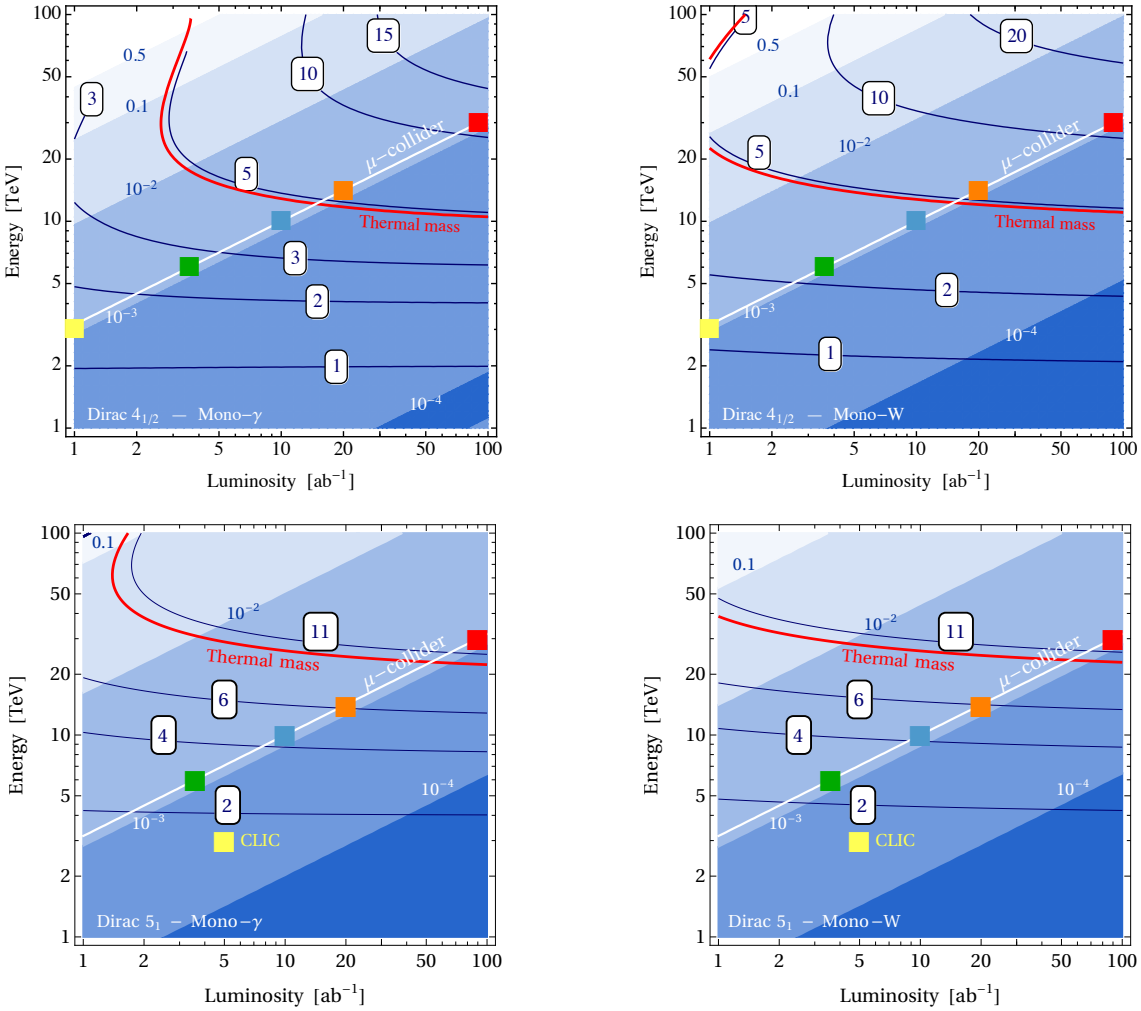

Figure 3.7: *Same as Fig. 3.6 for Dirac* $4_{1/2}$ *and* 5_1.

3.4 Non-minimal splittings

Exploiting the freedom to change the spectrum given by the UV operators in Eq. (3.1) one can have significant changes in the phenomenology described in Sec. 3.3. We dedicate this section to explore the phenomenological consequences of releasing the minimal splitting assumption.

3.4.1 Direct detection

The Higgs portal operators in Eq. (3.1) generate upon EWSB a linear coupling of the DM to the Higgs boson of the form

$$\mathscr{L}_{D,h} = -\frac{\lambda_D v}{2\Lambda_{\rm UV}}\chi^2_{\rm DM} h\,. \tag{3.28}$$

This coupling mediates tree-level SI scattering processes of DM onto nuclei, therefore it can be constrained by direct detection experiments. As the mass splitting δm_0 has to be sufficiently large to suppress the scattering mediated by the Z boson, we find that the allowed parameter space for the non-renormalizable couplings is compact.

Following Ref. [164] we can integrate out the Higgs boson and write the couplings of the DM to the SM

$$\mathscr{L}^{\rm SI}_{\rm eff,h} = \frac{\lambda_D}{2m_h^2\Lambda_{\rm UV}}\chi^2\left(m_q\bar{q}q - \frac{\alpha_s}{4\pi}G^a_{\mu\nu}G^{a\mu\nu}\right), \tag{3.29}$$

so that the matrix elements f_q and f_G required to compute $\sigma_{\rm SI}$ are simply given by

$$f_q = f_q^{\rm EW} + \frac{\lambda_D}{2m_h^2\Lambda_{\rm UV}},\; f_G = f_G^{\rm EW} - \frac{\alpha_s}{8\pi}\frac{\lambda_D}{2m_h^2\Lambda_{\rm UV}},$$

where $f_q^{\rm EW}$ and $f_G^{\rm EW}$ come from EW loops and are given in Eq. (3.26). We can rewrite the coupling λ_D solely in terms of mass splitting as

$$\frac{\lambda_D}{\Lambda_{\rm UV}} = -\frac{2Y}{v^2}(\delta\mu_{Q_M} + n\delta\mu_0)\,, \tag{3.30}$$

where

$$\delta\mu_{Q_M} \equiv \frac{2\delta m_{Q_M} - \delta m_0 - 2\Delta M^{\rm EW}_{Q_M}}{2Q_M}\,,\;\; \delta\mu_0 \equiv \frac{\delta m_0}{n} \tag{3.31}$$

and $\Delta M^{\rm EW}_{Q_M}$ is the gauge induced mass splitting in Eq. (3.10).

Replacing Eq. (3.30) into Eq. (2.56) allows us to translate the upper bound on $\sigma_{\rm SI}$ into an upper bound on δm_0 and δm_{Q_M}.

3.4.2 Collider searches

The splittings $\delta m_0, \delta m_{Q_M}$ determine the lifetime of the charged components of the EW multiplet, which are pivotal to understand the viable collider signatures. In what follows we take as reference the detector geometry proposed in [68] and we

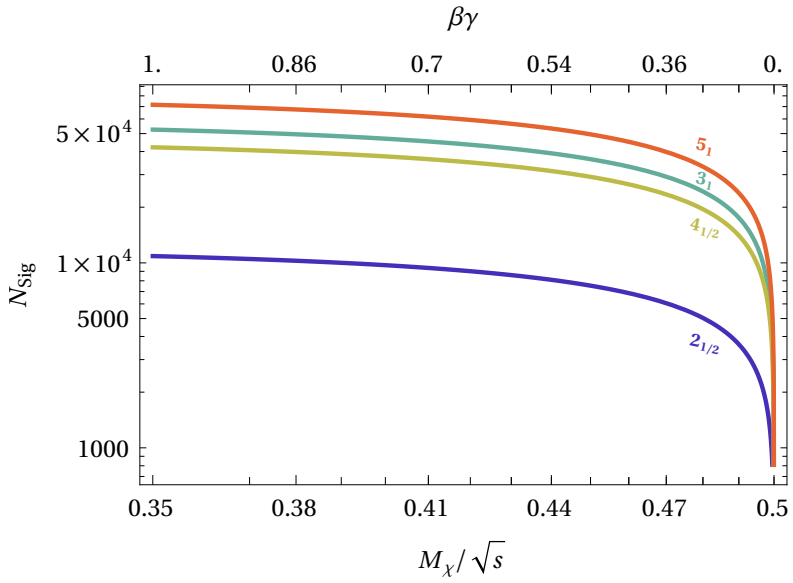

Figure 3.8: *Signal yield of the charged tracks for the* $2_{1/2}$, 3_1, $4_{1/2}$, 5_1. *The plot holds for all* $\sqrt{s}$ *in the tens of TeV range, assuming the luminosity scales as Eq. (2.26). The cuts applied on the produced charged* χ*'s are* $p_T > 200$ *GeV,* $|\eta_\chi| < 2$.

classify the parameter space $(\delta m_0, \delta m_{Q_M})$ in various regions according to the lifetime $\tau_{\rm LCP}$ of the Longest Lived Charged Particle (LCP) of a given multiplet.

Missing Mass. For $c\tau_{\rm LCP} < 0.33$ cm the lightest charged WIMP decays promptly on collider scales and gives missing energy signatures such as the mono-W and mono-γ discussed in Sec. 3.3. The choice for the threshold value to consider the signal as prompt corresponds to $c\tau/2$ of the charged track for the $2_{1/2}$ WIMP in the minimal splitting scenario, which is a known benchmark where DT reconstruction starts to become challenging. We refer for further details on MIM searches to Sec. 2.4.

Disappearing Tracks. For 1 m $> c\tau_{\rm LCP} > 0.33$ cm the lightest charged WIMP gives a disappearing track signal. This search has been introduced in Sec. 3.3. Here we generalize the analysis to non-zero hypercharges. To get a feel of how powerful DT searches can be, we fix the neutral splitting to a representative value $\delta m_0 \simeq 200$KeV for the fermions. Our results are given in Fig. 3.10 where we display the region of the plane WIMP mass versus $c\tau$ where experiments can probe the several WIMPs considered in each panel of the figure. For this result we consider only χ^+ and its conjugate as candidate long-lived for the $2_{1/2}$. For the 3_1, the $4_{1/2}$ and 5_1 all states with charge greater than 1 are assumed to decay promptly to the candidate charged long lived states at the bottom the spectrum.[3] As we have fixed δm_0 much smaller than the mass splitting between the neutral and charged states, we can effectively consider decays into both χ^0 and $\chi^{\rm DM}$ as if they were degenerate in mass. Considering the possible decay channels χ^- into $e^-\nu_e\chi^{0,{\rm DM}}$, $\mu^-\nu_\mu\chi^{0,{\rm DM}}$,

[3]We keep track in detail of the mixing of the charge ±1 gauge eigenstates into the suitable charge ±1 mass eigenstates.

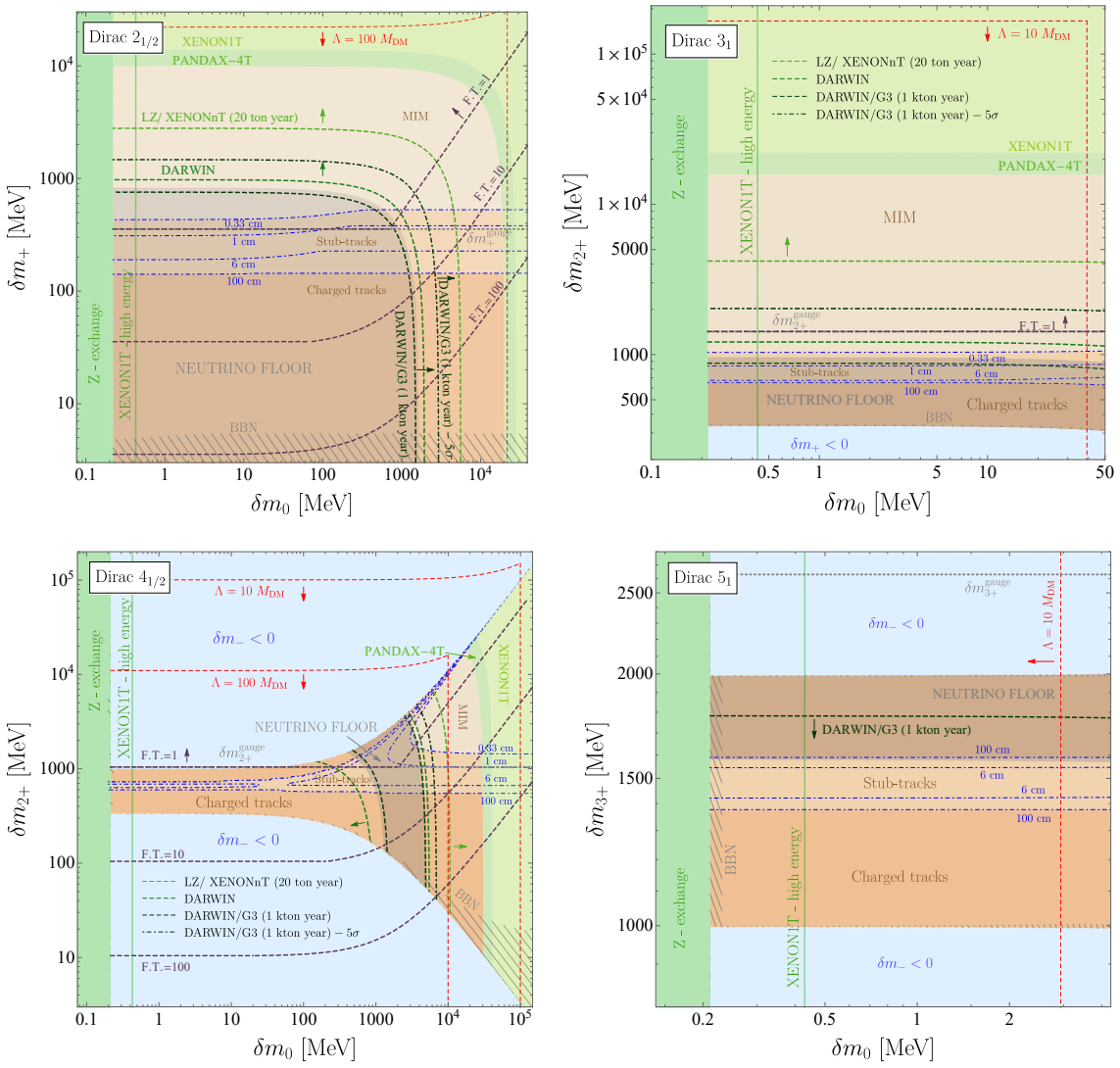

Figure 3.9: *Direct Detection and collider signatures in the plane δm_0 vs. δm_{Q_M} from the $2_{1/2}$ (upper left), 3_1 (upper right) $4_{1/2}$ (lower left) and 5_1 (lower right). The* **green** *shaded regions are excluded by current DD constraints on inelastic DM at small δm_0 and on Higgs-exchange elastic scattering at large splittings.* **Gray hatched** *regions are excluded by BBN constraints on the longest lived unstable particle in the multiplet.* **Red** *dashed lines delimit the range of perturbative mass splitting at fixed Λ_{UV}/M_{DM} ratio.* **Light blue** *shaded patches are not viable because the lightest WIMP in the n-plet is not the neutral one.* **Dashed green** *lines show prospects from future high exposure xenon experiments: LZ, DARWIN and DARWIN/G3 (arrows pointing to the direction of the expected probed region). In the* **gray shaded** *region the DD signal falls below the neutrino floor of xenon experiments [50, 150]. The vertical Xenon1T-high energy line show the ultime reach of xenon experiments on inelastic DM (see Fig. 3.1). Xenon* **Blue** *and* **black** *dashed lines corresponds to different expected lengths of charged tracks. Accordingly, different hues of* **brown** *distinguish regions where different signatures at future colliders are expected. The* **dashed gray** *line shows the EW value of δm_{Q_M}. **Purple** dashed lines show the contours of the fine-tuning among the different mass splittings as defined in Eq. (3.12). Mass splittings above the F.T.=1 line are not fine tuned.*

$\pi^- \chi^{0,\mathrm{DM}}$ and the charge conjugates for χ^+ we get

$$\Gamma\left(\chi^\pm \to \chi^{0,\mathrm{DM}} + \mathrm{SM}\right) = \Gamma_{e^\pm} + \Gamma_{\mu^\pm} + \Gamma_{\pi^\pm} \,, \tag{3.32}$$

where the RHS indicates the decay width into neutral states plus the SM states indicated by the subscript. The relevant widths are given by:

$$\begin{aligned}
\Gamma_{e^\pm} &= g\left(n, Y, \pm 1\right) \frac{G_F^2 \delta m_\pm^5}{60\pi^3} \,, \\
\Gamma_{\mu^\pm} &= g\left(n, Y, \pm 1\right) \frac{G_F^2 \delta m_\pm^5}{2\pi^3} \Phi(\delta m_\pm, m_\mu) \,, \\
\Gamma_{\pi^\pm} &= g\left(n, Y, \pm 1\right) \frac{G_F^2 f_\pi^2 |V_{ud}|^2 \delta m_\pm^3}{4\pi} \sqrt{1 - \frac{m_\pi^2}{\delta m_\pm^2}} \,,
\end{aligned} \tag{3.33}$$

where $g\left(n, Y, Q\right)$ accounts for the different strengths of the W boson coupling to each of the χ^Q:

$$g\left(n, Y, Q\right) = n^2 - 1 - 4(Q - Y)(Q - Y - \mathrm{sgn}(Q)) \,, \tag{3.34}$$

with n the dimensionality of the multiplet and Y its hypercharge, G_F is the Fermi constant, $f_\pi = 131$ MeV is the pion decay constant. In the above formula Φ is the full phase space of the 3-body decay of a massive particle of mass M into a massless lepton (e.g neutrino), a massive lepton with mass $m_l \ll M$ (e.g. muon), and a heavy particle with a mass $M - \delta$, for splitting $\delta \ll M$:

$$\begin{aligned}
\Phi(\delta, m_l) =& \frac{1}{60} \sqrt{\delta^2 - m_l^2} \left(2\delta^4 - 9\delta^2 m_l^2 - 8 m_l^4\right) + \\
&+ \frac{1}{4} m_l^4 \delta \,\mathrm{ArcCoth}\left(\frac{\delta}{\sqrt{\delta^2 - m_l^2}}\right) \,.
\end{aligned} \tag{3.35}$$

The massless limit was employed for the electron since in the regions relevant for DTs the splittings allow to neglect m_e. In principle, for large splittings, also kaon and tau channels should be considered. However, for such large splittings the decays into the other SM particles are so fast that tracks will never be reconstructed.

If we move away from the $\delta m_0 \simeq 0$ points, we have to consider cases in which χ^+ is heavier than some of the particles with $Q > 1$. We checked that for the 3_1, $4_{1/2}$, 5_1 there are choices of the couplings y_0 and y_+ for which $M_{\chi^{++}} < M_{\chi^+}$. In this case, χ^{++} cannot decay into χ^+, and is forced to decay to the neutral states by emitting twice an off-shell W boson that gives rise to $l^+\nu_l$ or π^+. This decay rate has been estimated by summing over all possible final states using NDA. With respect to the decay with just one off-shell W emission, we get an extra factor $g(n, Y, 2) G_F f_\pi \delta/(16\pi^2)$ and $g(n, y, 2) G_F \delta^2/(16\pi^2)^2$ for any extra π or $l^+ v_l$ pair, respectively. Decays into negatively charged states are even more suppressed, since they need more extra final states. These configurations can give χ^{++} DT signals as well as CT signals, which are potentially interesting for their peculiar detector response.

Following [68], we employ two different DT signal regions: i) events with at least one disappearing track in addition to a hard photon with energy $E_\gamma > 25$ GeV; ii)

events with two disappearing tracks, one of which is short, and the hard photon. The former has an estimated background cross section of $\sigma_B = 18.8$ ab at the 10 TeV collider, leading to a signal-to-noise ratio of order 1. The latter is background free. To compute the number of expected signal events, we do a Monte Carlo simulation with MadGraph5_aMC@NLO. We also got similar results employing the analytic approximation explained in the appendix of [83]. The sensitivity to disappearing tracks is shown in the plots of Fig. 3.10, for minimal δm_0 imposed by DD and BBN, as a function of the dark matter mass and the lifetime $c\tau$ for each of the considered WIMP candidates.

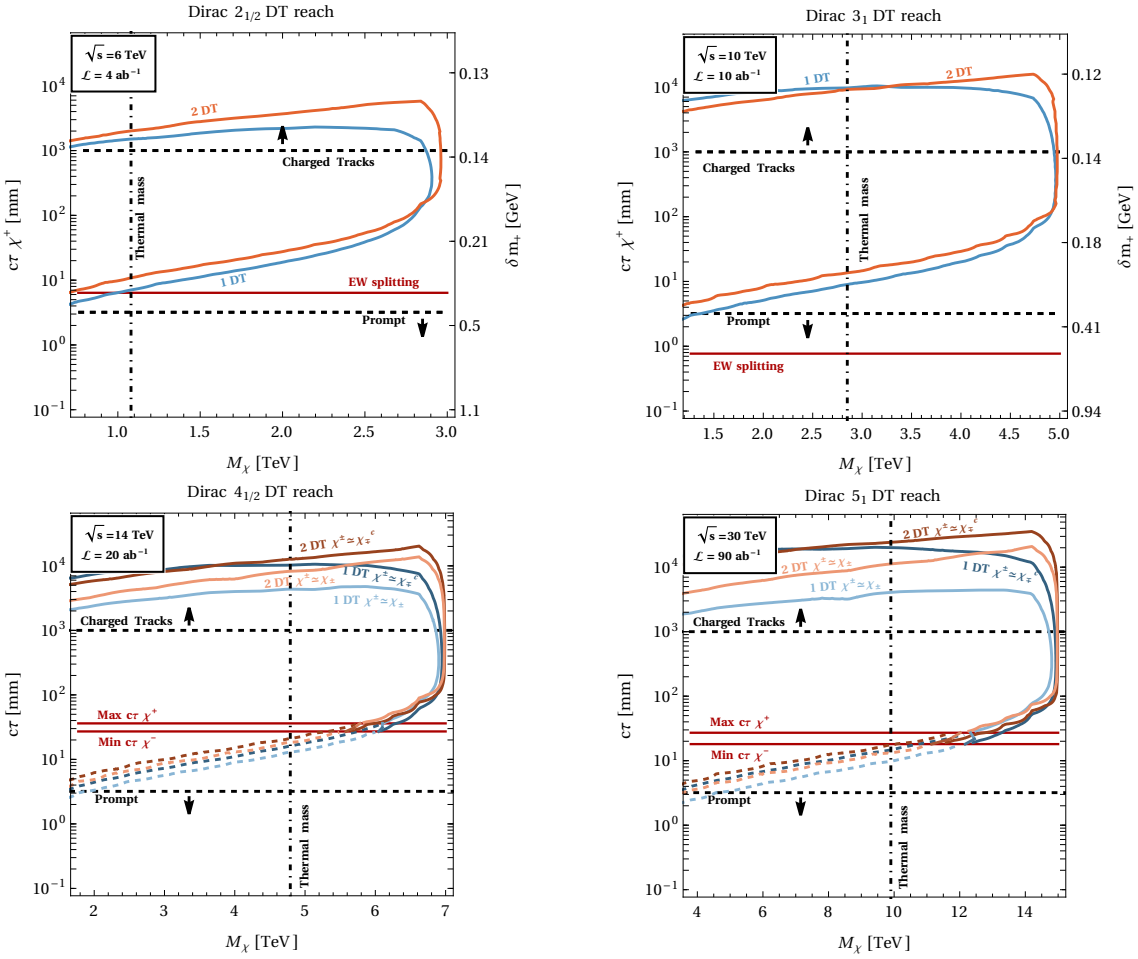

Figure 3.10: *Sensitivity at 95% C.L. from DT searches as a function of M_χ and the proper lifetime of the charged particle χ^+. The mass splitting δm_+ is also shown in the extra vertical axis in two upper panels. In the lower panels, the two different contours for each search channel correspond to the different physical situations where the heavy mass eigenstate corresponds to one of the two gauge eigenstates χ_+ or χ_-^c.* ***Top Left:*** *Dirac $2_{1/2}$ at $\sqrt{s} = 6$ TeV, $\mathcal{L} = 4$ ab^{-1}.* ***Top Right:*** *Dirac 3_1 at $\sqrt{s} = 10$ TeV, $\mathcal{L} = 10$ ab^{-1}.* ***Bottom Left:*** *Dirac $4_{1/2}$ at $\sqrt{s} = 14$ TeV, $\mathcal{L} = 20$ ab^{-1}.* ***Bottom Right:*** *Dirac 5_1 at $\sqrt{s} = 30$ TeV, $\mathcal{L} = 90$ ab^{-1}.*

Our results in Fig. 3.10 show that the thermal mass can be excluded over the entire range of lifetimes that give rise to the DT signature. For the $2_{1/2}$ this corresponds to the full parameter space with splitting larger than the EW one. The contours for the

$4_{1/2}$ and 5_1 WIMPs deserve some comment. In this case two singly-charged states are present: at least one state is in the DT region, and DT searches for this long-lived state, shown as solid contours, can probe the thermal mass over the full range of possible lifetimes. We also show the DT reach for the state with shorter lifetime, which could produce a second observable signal in parts of the parameter space. We show with different colors the two different physical solutions where the long-lived mass eigenstate χ^+ corresponds to the gauge eigenstate χ_+ or χ_-^c (corresponding to the regions of low or high δm_{2+} in Fig. 3.2), which have slightly different production cross-sections.

Charged Tracks. For $c\tau_{\rm LCP} > 1$ m the LCP gives long charged tracks (CT) with an average length roughly corresponding to the middle layer of the outer tracker. The SM background processes for this "long" track with anomalous properties strongly depends on the properties of the detector, therefore its study is outside the scope of this work. We limit ourselves to estimate the number of expected signal events of charged χ pair production at a muon collider, as shown in Fig. 3.8. We highlight that this results approximately hold for generic $\sqrt{s}$ in the domain of tens of TeV, as long as Eq. (2.26) for the luminosity holds. In Fig. 3.8 we show the $\beta\gamma$ of the produced charged particle, which plays a crucial role to disentangle these special tracks from the SM background.

Our estimates for the LCP signature is based on the counting the number of LCP produced. For the LCP we require $p_T > 200$ GeV, $|\eta_\chi| < 2$, inspired by LHC searches [163]. For the $2_{1/2}$ and 3_1 we include in our counting all charged particles production, using the fact that χ^{2+} always promptly decays to the long lived χ^+. For the $4_{1/2}$ and 5_1, which have more complicated spectra, we stick to the minimal splitting scenario for the estimate of the charged tracks yield, which corresponds to the minimal y_+ necessary to lift χ^- above $\chi_{\rm DM}$. In this spectrum configuration χ^- is the most natural and only candidate to make long charged tracks, therefore we only consider this contribution in our result.[4]

Finally, we briefly comment on the direct production of WIMP bound states. In the minimal splitting case, the analysis is pretty similar to the real case, since the effect of the operators $\mathcal{O}_0$ and $\mathcal{O}_+$ can be neglected. This means that the only state that can be resonantly produced is the ${}^n_1 s_3^{--}$, in the notation of Sec. 2.4.3. Therefore, scalars are not suitable for this kind of search and the first multiplet for each hypercharge that can be probed are the Dirac $4_{1/2}$, 5_0 and 5_1. In the non-minimal splitting scenario, instead, the operators with the Higgs, as well as their parity odd counterpart in Eq. (D.1) and Eq. (D.3), introduce additional production channels, similarly to what happens in DD. For example, bound states like ${}^n s_3$ can now be resonantly produced in the complex scalar case, which, conversely to the real WIMPs, can thus in principle be probed through this channel. Besides, the pattern of intra-BS decays is modified by the non-zero hypercharge of the multiplet, so that new signatures, albeit rare, can be expected. In any case, since these additional dynamics is sourced by the operators with the Higgs, BS production in this scenario

[4] We neglect any possible contribution coming from χ^+ decaying into $\chi^{-,c}$, since in the region where mixing is relevant, the charged particles lifetimes are too short and are in the "stub tracks region", as shown in Fig. 3.9.

can only be used to probe the wider parameter space of complex WIMPs, rather than conclusively exclude or discover DM. The analysis of BS production at collider for complex WIMPs is left to a devoted work.

3.4.3 Parameter space for complex WIMPs

In the rest of this section, we examine in greater detail the parameter space spanned by δm_0 and δm_{Q_M} specifically looking at each of the lightest multiplets of Tab. E.1 up to the 5_1 WIMP. This will allow us to discuss the salient phenomenological features of the complex WIMPs.

The Dirac $2_{1/2}$ and 3_1

The $2_{1/2}$ and 3_1 are special WIMPs because they are the only multiplets with maximal hypercharge compatible with our assumptions. In particular, for $2_{1/2}$ requiring $\delta m_{0,+} > 0$ automatically implies the neutral WIMP candidate is the lightest one. Perturbativity requires $\delta m_0 < 40$ MeV for the $n = 3_1$ WIMP, because of the strong suppression of the 7 dimensional operator generating the neutral splitting. The narrower range of δm_0 for the 3_1 with respect to $2_{1/2}$ was expected from the higher dimensionality of $\mathcal{O}_0$ for $Y = 1$ as compared to $Y = 1/2$.

In Fig. 3.9 we show the constraints on the Dirac $2_{1/2}$ and 3_1 in the parameter space spanned by δm_0 and δm_{Q_M} coming from present DD experiments like Xenon1T and PANDAX-4T, as well as prospect from future high exposure Xenon experiments, *i.e.* LZ, XENONnT, DARWIN and DARWIN/G3. As we can see from Eq. (3.30), these bounds depend solely on the combination

$$\delta\mu \equiv 2\delta m_{Q_M} + (2Q_M - 1)\delta m_0 \ . \tag{3.36}$$

In particular we find

$$\sigma_{\rm SI} \approx 10^{-48}{\rm cm}^2 \begin{cases} \left(0.3 - \dfrac{\delta\mu}{1\ {\rm GeV}}\right)^2, & [2_{1/2}] \\ \left(0.2 + \dfrac{\delta\mu}{1\ {\rm GeV}}\right)^2, & [3_1] \end{cases} . \tag{3.37}$$

In the region of low mass splitting for both $2_{1/2}$ and 3_1 the direct detection cross section lies below the neutrino floor. For $2_{1/2}$, Eq. (3.37) shows that large cancellations between EW loops and tree-level Higgs exchange occur around $\delta\mu \simeq 300$ MeV, while for 3_1 the minimum $\sigma_{\rm SI}$ is obtained for $\delta\mu = 0$ and falls below the neutrino floor. To produce a direct detection cross section above the neutrino floor for the $2_{1/2}$ (3_1) we need $\delta\mu > 1.6$ GeV ($\delta\mu > 2.0$ GeV). PANDAX-4T already excludes mass splitting $\delta\mu < 20$ GeV ($\delta\mu < 30$ GeV) for the $2_{1/2}$ (3_1).

All in all, DD still leaves a large portion of parameter space unconstrained between the neutrino floor and the PANDAX-4T constraints. Remarkably, this region corresponds to mass splittings that do not require tuned adjustments of the three contributions to δm_0 and δm_+. The region of large splittings down to $\delta\mu \sim 1$ GeV

can be covered by large exposure Xenon experiments while the large portion of the parameter space lying below the neutrino floor should be taken as a major motivation for a future muon collider.

For $2_{1/2}$ WIMP the neutrino floor region can be fully probed only via a combination of charged tracks, DT and MIM searches. The different search strategies become relevant depending on the δm_+ value, as shown in Fig. 3.9. For the 3_1 WIMP stub and charged tracks can exclude the entire neutrino floor region, while MIM and DT searches can be complementary to large exposure DD experiments to probe the rest of the parameter space.

While the plot in Fig. 3.9 show the possible regions in which DT can be reconstructed efficiently, they do not show if the reach is large enough to guarantee exclusion (or discovery) of the WIMP candidate. For these two WIMP candidates a detailed discussion was given in Sec. 3.3.2. The general message is that for $\sqrt{s}$ sufficiently larger than twice the thermal DM mass DT searches will be powerful enough to probe the parameter space.

The Dirac $4_{1/2}$ and 5_1

Being the first multiplet with non-maximal hypercharge, the constraints coming from DM stability shape the allowed parameter space of the $4_{1/2}$. In particular, we must require δm_- to be positive. This constraint excludes the light blue shaded region in Fig. 3.9 bottom left.

The region where the direct detection cross section lies below the neutrino floor is reduced to a tiny band for 4 GeV $< \delta\mu <$ 15 GeV. This region can be probed by direct searches at a future high energy muon collider with $\sqrt{s} > 10$ TeV because of the thermal mass of the $4_{1/2}$ lies around 4.8 TeV. In particular, stub and charged tracks searches could cover almost the entire neutrino floor region, except for a small portion accessible only to MIM searches. The rest of the viable parameter space for the $4_{1/2}$ can be in principle probed by large exposure direct detection experiments.

We show the parameter space of the 5_1 WIMP in Fig. 3.9 bottom right. The dominant constraint comes from the perturbativity of the operator generating the neutral splitting, which requires $\delta m_0 < 3$ MeV. As a consequence, testing larger splittings for inelastic DM at Xenon1T can already probe large portions of the allowed parameter space of the 5_1. DM stability requires 1 GeV $\lesssim \delta m_{3+} \lesssim$ 2 GeV. The parameter space can be fully excluded by charged and stub track searches if a muon collider of $\sqrt{s} > 20$ TeV will be constructed. Besides, all the allowed mass splittings except a small window 1.8 GeV $\lesssim \delta m_{3+} \lesssim$ 2.0 GeV can be probed by DARWIN/G3.

3.5 Indirect probes of complex WIMPs

In this section we briefly comment on indirect probes of complex WIMPs, focusing in particular on the distinctive imprints of their Higgs interactions on precision electroweak observables (Sec. 3.5.1) and on the electron dipole moment (Sec. 3.5.2).

3.5.1 Electroweak precision observables

The addition of new EW multiplets to the SM leads to deviations in EW observables which could be tested with LEP data, at the LHC and at future colliders [30, 165]. Since the presence of new EW multiplets affects mainly gauge bosons self energies, their indirect effects can be encoded in the oblique parameters [166, 167]. Here we briefly summarize the main features of these contributions following the notation of Ref. [167]. The most relevant oblique parameters can be related to the SM gauge boson vacuum polarizations

$$\begin{aligned} \hat{Y} &= \frac{g_Y^2 m_W^2}{2}\Pi''_{BB}(0) \quad , \quad \hat{W} = \frac{g_2^2 m_W^2}{2}\Pi''_{33}(0) \ , \\ \hat{S} &= \Pi'_{3B}(0) \quad , \quad \hat{T} = \frac{\Pi_{33}(0) - \Pi_{WW}(0)}{m_W^2} \ , \end{aligned} \tag{3.38}$$

where Π_{ij} appear in the kinetic terms of the EFT describing the SM vectors interactions at energies smaller than the DM mass

$$\mathscr{L}_{\text{oblique}} = -\frac{1}{2} V_i^\mu \Pi_{ij} V_{j,\mu} \ . \tag{3.39}$$

In particular, all the EW multiplets (both real and complex) give a universal contribution to the $\hat{W}$, $\hat{Y}$ as previously found in [23]

$$\hat{W} = \frac{\alpha_{\text{em}} \cot^2\theta_W}{180\pi}\frac{m_Z^2}{M_{\text{DM}}^2}\kappa n(n^2-1) \simeq 3.8\kappa \times 10^{-7}\left(\frac{1\text{ TeV}}{M_{\text{DM}}}\right)^2 n(n^2-1) \tag{3.40}$$

$$\hat{Y} = \frac{\alpha_{\text{em}}}{15\pi}\frac{m_Z^2}{M_{\text{DM}}^2}\kappa n Y^2 \simeq 3.4\kappa \times 10^{-7}\left(\frac{Y}{1/2}\right)^2\left(\frac{1\text{ TeV}}{M_{\text{DM}}}\right)^2 n \tag{3.41}$$

where $\kappa = 1, 1/2, 1/8, 1/16$ for Dirac fermions, real fermions, complex scalars and real scalars respectively. The rough expectations for heavier WIMPs can be obtained from the equations above by remembering that $M_{\text{DM}} \sim n^{5/2}$. The contribution to $\hat{W}$ scale like as $\sim 1/n^2$ while the one to $\hat{Y}$ as $\sim 1/n^4$.

$\hat{W}$ and $\hat{Y}$ induce effects in SM observables that grow with energy so that LHC searches have already ameliorated the sensitivity on these operators compared to LEP. In particular $\hat{W}$ has been recently bounded by CMS [168] and $\hat{Y}$ is also set to be tested with a similar precision [169]. Even if the current precision is not sufficient to probe the WIMP thermal masses, further improvements are expected in a future high energy muon collider. This could provide interesting indirect tests of EW WIMPs [30, 170, 171]. The size of the expected WIMP contributions in Eq. (3.40) and Eq. (3.41) the results of Ref. [171] indicates that a muon collider of $\sqrt{s} = 30$ TeV would be needed to observed these deviations.

As extensively discussed in this paper, complex WIMPs require contact interactions with the SM Higgs to be phenomenologically viable. These interactions give an additional contributions to the $\hat{S}$ parameter. Moreover, the mass splittings inside the EW multiplet induced by $\mathcal{O}_0$ and $\mathcal{O}_+$ break the custodial symmetry in the Higgs

sector. As a consequence, complex WIMPs give irreducible contributions also to the $\hat{T}$ parameter. The explicit formulas for fermionic WIMPs are

$$\hat{S}_F = -\frac{\alpha_{\rm em} Y n(n^2-1)}{9\pi s_{2W} M_{\rm DM}} \delta\mu_{Q_M} \simeq -1.6\times 10^{-6} \left(\frac{Y}{1/2}\right)\left(\frac{1\text{ TeV}}{M_{\rm DM}}\right)\left(\frac{\delta\mu_{Q_M}}{10\text{ GeV}}\right) n(n^2-1)\,, \tag{3.42}$$

$$\hat{T}_F = -\frac{\alpha_{\rm em}}{18\pi s_{2W}^2} n(n^2-1)\frac{\delta\mu_{Q_M}^2+\delta\mu_0^2}{m_Z^2} \simeq -2.3\times 10^{-6}\frac{\delta\mu_{Q_M}^2+\delta\mu_0^2}{100\text{ GeV}^2} n(n^2-1)\,, \tag{3.43}$$

where $s_{2W}^2 = \sin^2 2\theta_W \simeq 0.83$ while $\delta\mu_{Q_M}$ and $\delta\mu_0$ are defined in Eq. (3.31). The corresponding formulas for scalar WIMPs are easily obtained from the fermionic ones by replacing $\hat{S}_S = \frac{1}{4}\hat{S}_F$ and $\hat{T}_S = -\hat{T}_F$. Our result for $\hat{T}_S$ is consistent with the result in Ref. [27], first computed in [172].

Both $\hat{S}$ and $\hat{T}$ are currently constrained at the level of 3×10^{-3} by LEP data (where the precise value will of course depend on the correlation between these two parameters [167]). High luminosity colliders further exploring the Z pole like FCC-ee will improve this precision typically by a factor of 10 [173] with the ultimate goal of pushing the precision of EW observables to the level of 10^{-5} [174].

Concerning $\hat{S}$ we conclude that the deviations induced by complex WIMPs are unlikely to be visible unless for light multiplets with the ultimate EW precision. Conversely, at fixed large splitting and increasing size of the multiplet, the deviations on $\hat{T}$ are enhanced to the point that a $12_{1/2}$ multiplet is giving $\hat{T}\simeq 3\times 10^{-3}$, which is within the reach of current LEP data and could help reducing the tension the m_W mass extracted from the EW fit and the one measured directly by the CDF collaboration [175]. Of course this extreme scenario requires very large couplings at the boundary of perturbativity for the contact operators inducing the splitting in Eq. (3.1).

3.5.2 Electric dipole moment

As mentioned in Sec. 3.1 and detailed in Appendix D.1, the operators generating the splittings for fermionic WIMPs have in general two different chiral structures and different relative phases. This generically induces operators contributing to the electron EDM at 1-loop [176, 177]. Following the notation of Ref. [176], the leading operator generated by WIMPs loops is

$$\mathscr{L}_{\rm EDM} \supset \frac{c_{WW}}{\Lambda_{\rm UV}^2}|H|^2 W\tilde{W}\,, \tag{3.44}$$

where we neglect for this discussion operators such as $|H|^2 B\tilde{B}$ and $H^\dagger\sigma^a H W\tilde{B}$ that would be suppressed by powers of Y/n with respect to the one with two $SU(2)$ field strength insertions.

The Wilson coefficient in Eq. (3.44) is constrained by the recent measurement of the ACME collaboration [178] to be

$$c_{WW} < 4 \times 10^{-3} g_2^2 \left(\frac{\Lambda_{\rm UV}}{10\ {\rm TeV}}\right)^2 \frac{d_e}{1.1 \times 10^{-29} {\rm e\,cm}} \ . \tag{3.45}$$

The effective operator in Eq. (3.44), is generated at $4Y$-loops from the $\mathcal{O}_0$ operator and its axial partner and at 2-loop from the $\mathcal{O}_+$ operator and its axial partner. For example the 2-loops Wilson coefficients can be estimated as

$$c_{WW}|_{2-{\rm loop}} \simeq \frac{g_2^2 n (n^2-1)^2 \mathcal{I}[y_I y_{I,5}^*]}{32 (16\pi^2)^2 \Lambda_{\rm UV}^2} \ , \tag{3.46}$$

where the index y_I controls the contribution from $\mathcal{O}_0$ or $\mathcal{O}_+$ and $y_{I,5}$ the ones from their axial counterpart. If only $\mathcal{O}_0$ is present, like it would be for instance in the minimal splitting case for the $2_{1/2}$ multiplet, the bound in Eq. (3.45) can be rewritten as an upper bound on the neutral splitting

$$\delta m_0 < 16\ {\rm GeV} \left(\frac{2}{n}\right)^{\frac{3}{2}} |\theta_{\rm CP}|^{\frac{1}{2}} \sqrt{\frac{|d_e|}{1.1 \times 10^{-29} {\rm e\,cm}}} \ , \tag{3.47}$$

where we defined $\theta_{\rm CP} = y_I^2 / \mathcal{I}[y_I y_{I,5}^*]$. A similar bound is found for δm_{Q_M} in the minimal splitting case, where $\mathcal{O}_0$ can be neglected. Hence, for $\mathcal{O}(1)$ couplings and CP-violating phases, the EDM already gives competitive if not stronger bounds with respect to those shown in Table 3.1. Interestingly, future experimental upgrades are expected to be sensitive to electron EDM as small as $d_e \simeq 10^{-34}$e cm [179] which would provide sensitivity to the WIMP parameter space down to splittings of order ~ 50 MeV for $\mathcal{O}(1)$ couplings and CP-violating phases.

It would be interesting to further explore this direction in models where the $\mathcal{O}(1)$ CP-violating phase is motivated by a mechanism producing the observed baryon asymmetry in the Universe such as WIMP baryogenesis [180, 181].

3.6 Summary

In this Chapter we derived the full classification of WIMP in complex representations of the EW group. Our only assumption is that below a certain UV scale the SM is extended by the addition of a single EW multiplet containing the DM candidate. Our main results are contained in Table 3.1, where we give all the freeze-out predictions for the WIMP thermal masses, the ranges of phenomenologically viable splittings and the maximal scale separation between the DM mass and the UV physics generating the splittings.

We then inspected the phenomenology of complex WIMPs with the goal of understanding what would be required experimentally to provide the ultimate test on the EW nature of DM. We focused on the interplay between future large exposure direct detection experiments and a future high energy lepton collider, e.g. a muon collider. The reach from the current and forthcoming indirect detection experiments

of pure electroweak multiplets are very promising (see e.g. [34, 73] for current reaches and [42, 182] for prospects). Neverthless a robust assessments of the sensitivities for all the complex WIMPs classified here and the real WIMPs classified in would require a careful evaluation of the expected annihilation cross sections and an assessment of the astrophyisical uncertanties [77]. We leave this work for a future investigation. Similarly, the prospects of discovering WIMPs via kinetic heating of compact astrophysical objects, like neutron stars [183, 184] or white dwarfs [185], should be further assessed by the future James Webb Space Telescope infrared surveys [186].

Our main result is that a kiloton exposure Xenon experiment would be able to probe most of the complex and the real WIMPs, with the notable exceptions of the complex doublet with $Y = 1/2$ whose cross section lies naturally well below the neutrino floor. This result for the complex doublet was of course well known from the many previous studies on the SUSY Higgsino [187], but it gets further substantiated in the context of our WIMP classification. Our findings constitute a major motivation to push forward the research and development of a future high energy lepton collider. Specifically, we find that a future muon collider with $\sqrt{s} = 6$ TeV would be able to fully probe the existence of a fermionic complex WIMP doublet at its thermal mass around 1.1 TeV.

We further study the parameter space of the different complex WIMPs and find regions where the direct detection cross section can drop below the neutrino floor because of accidental cancellations of the EW elastic scattering (like for the 5_1) or at small (mildly tuned) values of the charged-neutral mass splittings (like for the 3_1) or for the destructive interference of EW and Higgs induced scattering (like for the $4_{1/2}$). In all these cases a high energy lepton collider might be again the only way of discovering these WIMPs.

Interestingly, the list of WIMP candidates we furnished provides a series of targets that can be probed at successive stages of a future machine. Moreover, our analysis shows that future searches for long-lived charged tracks will be crucial to fully probe the WIMP parameter space. This strongly motivates a detailed collider study assessing the expected sensitivity of these searches in a realistic muon collider environment. We hope to come back to this issue in the near future.

Chapter 4

Conclusions

In this Thesis we have reanalyzed the WIMP paradigm focusing on the case in which the DM is the neutral component of a single EW multiplet, both scalar and fermionic. In Chapter 2 and 3 we distinguished between two main cases, the *real* and *complex* EW WIMP, respectively. For each case, we determined the largest dimensionality n of the multiplets allowed by the perturbative unitarity bound (PUB). In the complex case, a further condition comes from the request that the coefficients of the operators necessary to make the DM inelastic and lighter with respect to the charged components of the multiplet remain perturbative. All in all, we found the following list of calculable candidates, which thus defines our window of EW WIMP:

- Odd $n \leq 13$ and $Y = 0(\epsilon)$;
- Even $n \leq 12$ and $Y = 1/2$;
- $n = 3, 5$ and $Y = 1$.

For each candidate we determined the thermal mass, obtained including the non-perturbative effects represented by the Sommerfeld enhancement and bound state formation. With the thermal masses at our disposal, we then proceeded with a systematic analysis of DM phenomenology at future experiments, focusing on direct detection and lepton colliders.

In the real case studied in Chapter 2, we showed that a high exposure Xenon experiment like DARWIN would be in the position to wipe out the entire WIMP window. This represents the main motivation for this kind of experiment and a unique opportunity to reliably test all the real candidates at once. Collider searches, in fact, can be employed to probe only the lightest multiplets. In this Thesis, we assumed that a lepton (muon) collider with a center-of-mass energy $\sqrt{s}$ up to 30 TeV can be built. We considered three kind of searches: missing mass (MIM), disappearing tracks (DT) and bound state production. DT is the most efficient channel for the 3-plets, which can be discovered with $\sqrt{s} \geq 6$ TeV. For the 5-plets, instead, $\sqrt{s} > 30$ TeV is necessary both for MIM and DT search for a 2σ exclusion. In fact, the best opportunity to discover the Majorana 5-plet is through bound state production. In particular, BS with the same quantum numbers of EW vectors, namely the ${}^n s_3$, can

be produced resonantly with a large cross-section. The production rates of such states can be so large that one day of running can be enough to claim the discovery. Besides, additional signatures like vectors emitted by decays among bound states, though rarer, can be observed. Such channel is basically precluded for the scalar 5-plet, since spin statistics forbids the formation of ${}^{n}s_3$ states, while production rates of other BS are to small to be significant.
Finally, we commented on the potential of indirect detection searches performed by next-generation telescopes like CTA. Similarly to direct detection, ID searches can probe the entire window of DM candidates. Unfortunately, a more precise determination of the thermal mass as well as of the annihilation cross-section, including one-loop contributions, is required and is left for future work.

The complex candidates, except for the "millicharged" multiplets, considered in Chapter 3, exhibit a richer and more variegated phenomenology with respect to their real counterparts. This is mainly due to the presence of the UV mass splittings generated by the operators with the Higgs $\mathcal{O}_+$ and $\mathcal{O}_0$. We scanned the parameter space spanned by these mass splittings for all complex candidates with $Y = 1/2$, 1 up to $n = 5$, showing the interplay between DD and collider searches. In particular, DD can exclude most of this parameter space, except for those regions where the signal falls below the neutrino floor because of cancellations between loop diagrams induced by gauge interactions and tree-level contributions from $\mathcal{O}_+$ and $\mathcal{O}_0$. Hence, conversely to the real case, DD alone is no longer sufficient to probe the entire window due to the larger parameter space. This provides a main motivation for a lepton collider which can exclude the lightest candidates as well as providing complementary constraints and information on the dynamics of DM. For example, DT searches are crucial to further probe the parameter space of mass splittings. The richer dynamics related to bound state production is left for future analysis. A summary of the capabilities of the several stages of a high energy muon collider is given in Fig. 4.1 under the assumption of luminosity following the scaling of Eq. (2.26) and minimal splitting for the complex WIMP. The upshot of these studies is that, as the center of mass energy of the collider is increased, the higher energy machine gains sensitivity to heavier WIMP candidates.

In summary, in this Thesis we aimed at conveying two messages. The first is that the window of EW WIMP is wider than what considered so far in the literature. The second is that future experiments are in a very good position in covering most of the EW WIMP parameter space. DD, in particular, is the most promising strategy as it will be able to discover or definitely exclude many WIMP models. Besides that, EW WIMP searches would greatly benefit if a muon collider will ever be built, as it would represent a fundamental complementary tool to DD experiments.

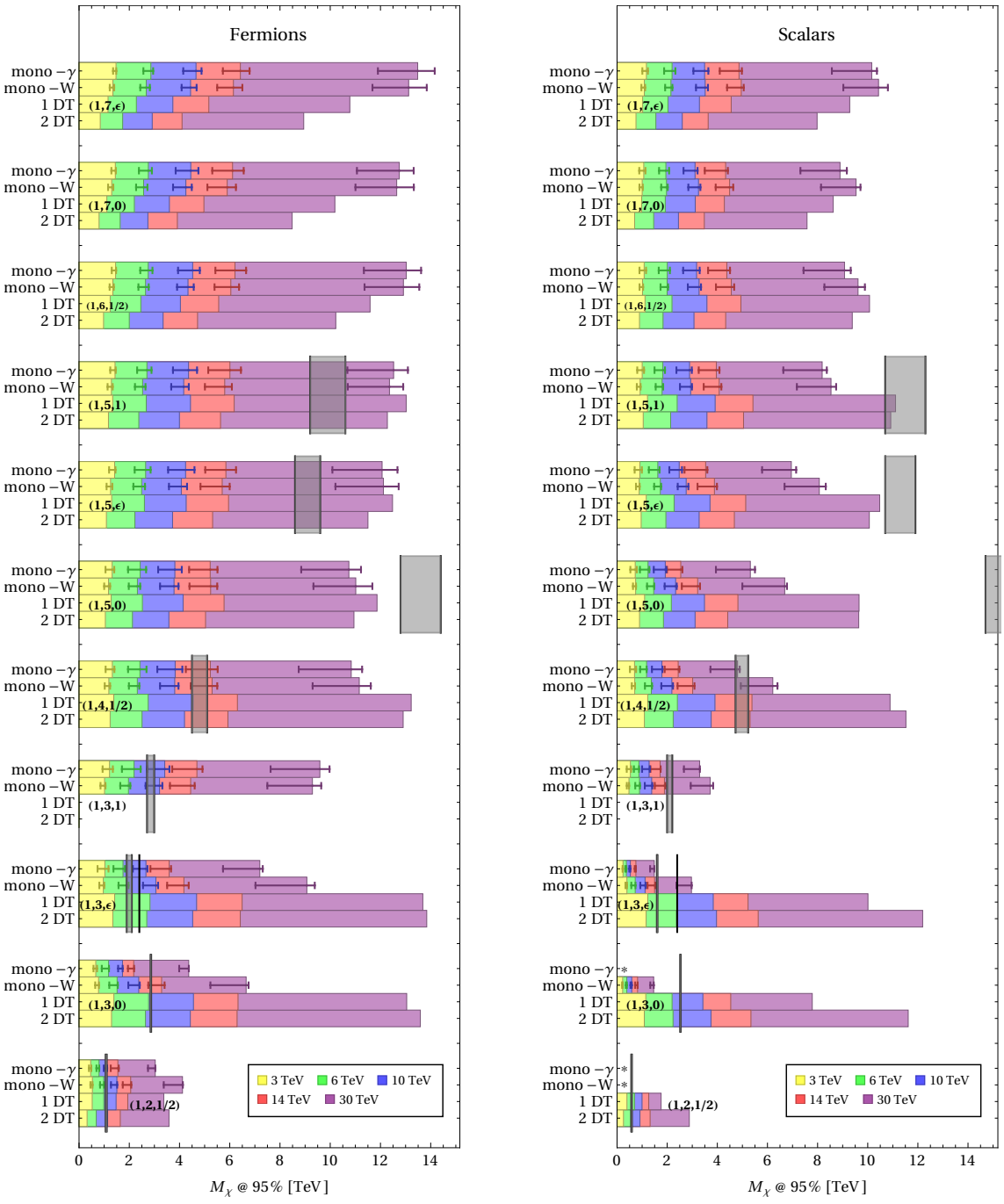

Figure 4.1: *Mass reach in the mono-γ, mono-W and DT channels for fixed luminosity as per Eq. (2.26) at $\sqrt{s}$ 3 TeV (yellow), 6 TeV (green), 10 TeV (light blue), 14 TeV (red), and 30 TeV (purple). In the mono-W and mono-γ searches we show an error bar, which covers the range of possible exclusion as the systematic uncertainties are varies from 0 to 1%. The colored bars are for an intermediate choice of systematics at 0.1%. Missing bars denoted by an asterisk * correspond to cases where no exclusion can be set in the mass range $M_\chi > 0.1\sqrt{s}$. For such cases it is worth considering VBF production modes at the fixed luminosity Eq. (2.26) or higher luminosity at potentially smaller $\sqrt{s}$.*

Appendix A

Bound States Dynamics at NLO

In this Appendix we discuss the general features of BSF at leading order (LO) in gauge boson emission and at next-to-leading order (NLO) in gauge boson emission.

At leading order, bound states form through the emission of a single vector boson V^a: $\chi_i + \chi_j \to \mathrm{BS}_{i'j'} + V^a$. The non-relativistic limit of the amplitude can be recast in the form of an effective interaction Hamiltonian, such that the full amplitude can be obtained from its matrix element with the wave function of the initial and final two-particle states (reconstructed from the resummation of the ladder diagrams). The leading order contribution to this effective hamiltonian comes in the form of electric dipole interaction terms [26, 36]:

$$\begin{aligned} \mathscr{H}_I^{\mathrm{LO}} = & -\frac{g_2}{M_\chi}\left(\vec{A}^a(\vec{x}_1)\cdot\vec{p}_1 T^a_{i'i}\delta_{j'j} + \vec{A}^a(\vec{x}_2)\cdot\vec{p}_2\overline{T}^a_{j'j}\delta_{i'i}\right) \\ & + g_2\alpha_2\left(\vec{A}^a(0)\cdot\hat{r}e^{-M_a r}\right) T^b_{i'i}\overline{T}^c_{j'j} f^{abc} \,, \end{aligned} \tag{A.1}$$

where the first to terms are a simple generalization of the standard QED dipole interaction while the last one is a purely non-abelian term which arises from vector boson emission from a vector line.

The computation of the transition amplitudes from Eq. (A.1) simplifies if we assume the $\mathrm{SU}(2)_L$-invariant limit. This approximation applies when the DM (BS) de Broglie wavelength is much smaller than the range of the Yukawa interaction $1/m_W$ and therefore for $z \leq (M_\chi/m_W)^2$. In this regime the Yukawa potential is well approximated by the Coulomb one which turns out to be a good approximation to describe WIMP freeze-out. The BS dynamics can then be understood by using isospin selection rules while the main consequence of having finite vector masses is to provide an energy threshold to the emission of a single massive boson in the formation or the decay of a BS.

Since $\alpha_{\mathrm{eff}} \sim n^2$, increasing the dimensionality of the DM multiplet enhances next to leading order (NLO) processes in gauge boson emission such as $\chi_i + \chi_j \to \mathrm{BS}_{i'j'} +$

$V^a + V^b$. These could be in principle relevant for both the computation of the thermal mass and the saturation of the perturbative unitarity bound.

The main NLO contributions to BSF come from diagrams like the ones in Fig. A.1 and are essentially of two types: i) the first diagram is essentially the second order Born approximation of the LO Hamiltonian, with the intermediate state being a free or a BS; ii) the second diagram, where the two emitted vectors come from the same vertex, is generated by the effective Hamiltonian at order $\mathcal{O}(A^2)$. The latter contains terms of the form

$$\mathscr{H}_I^{\rm NLO} \supset \frac{g_2^2}{2M_\chi} T^a T^b \left[\vec{A}^a \cdot \vec{A}^b + \frac{(\vec{p}\cdot\vec{A}^a)(\vec{p}\cdot\vec{A}^b)}{M_\chi^2} \right], \tag{A.2}$$

where we focus here on the abelian part of the hamiltonian, postponing a full study for a future work. Given the above Hamiltonian and the LO one in Eq. (A.1) we can estimate the corresponding contribution to the double emission BSF cross-section as:

$$\sigma_{\rm BSF}^{\rm LO} v_{\rm rel} \simeq \frac{2\pi\alpha_{\rm eff}}{M_\chi^3 n^2} \Delta E \tag{A.3}$$

$$\sigma_{\rm BSF}^{\rm NLO} v_{\rm rel} \simeq \frac{g_\chi^2}{8 M_\chi^2 v_{\rm rel} n^2} \left(\frac{\Delta E}{M_\chi}\right)^3 . \tag{A.4}$$

In the LO estimate, a factor $\frac{2}{\alpha_{\rm eff} M_\chi} \frac{2\pi\alpha_{\rm eff}}{v_{\rm rel}}$ comes from the overlap integral while a factor $\frac{\Delta E}{8\pi}$ from the two-body phase space. Similarly, in the NLO estimate a factor $\frac{1}{2}\frac{\Delta E^3}{256\pi^3}$ comes from the 3-body phase space, taking into account the two identical final vectors, and $\left(\frac{2}{\alpha_{\rm eff} M_\chi}\right)^3 \frac{2\pi\alpha_{\rm eff}}{v_{\rm rel}}$ from the overlap integrals between the wave functions. From the above formula we derive the scaling of the NLO corrections in Eq. (2.23).

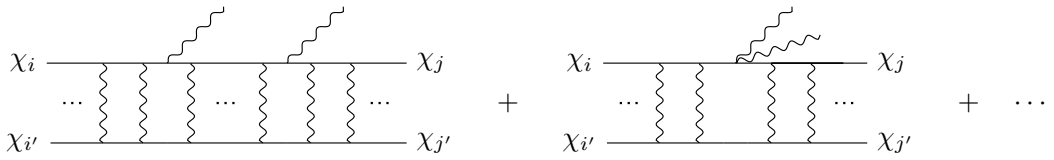

Figure A.1: *Examples of diagrams controlling the BS effective Hamiltonian at next-to-leading order in gauge boson emission The first diagram corresponds to the second order Born approximation for the dipole operators in Eq. (A.1), where the resummation of the vector boson insertions between the two emission reconstructs the wave function of an intermediate BS or scattering state. The second diagram, instead, is obtained from the $\mathcal{O}(A^2)$ terms in the interaction Hamiltonian, at leading order in the Born approximation.*

We now discuss the contributions from second order Born expansion whose general expression is given by

$$(\sigma v_{\rm rel})_{2V} = \frac{2^6 \alpha_2^2}{3^3 \pi M_\chi^4} \int {\rm d}\omega \omega (E_n - \omega) \left| \mathcal{C}_{\rm BS} + \mathcal{C}_{\rm free} \right|^2 , \tag{A.5}$$

where we defined

$$\mathcal{C}_{\rm BS} = \sum_m \left(\frac{1}{E_n - E_m - \omega + i\Gamma_{{\rm dec},m}} + \frac{1}{\omega - E_m + i\Gamma_{{\rm dec},m}} \right) \mathcal{I}_{\vec{q}m} \mathcal{I}_{mn} \ , \tag{A.6a}$$

$$\mathcal{C}_{\rm free} = \int \frac{{\rm d}^3 k}{(2\pi)^3} \left(\frac{1}{E_n - \omega + \frac{k^2}{M_\chi} + i\epsilon} + \frac{1}{\omega - \frac{q^2}{M_\chi} + \frac{k^2}{M_\chi} + i\epsilon} \right) \mathcal{I}_{\vec{q}\vec{k}} \mathcal{I}_{\vec{k}f} \ , \tag{A.6b}$$

with $\mathcal{I}_{if}$ being the overlap integrals between the states i and f, the index m running over all intermediate BS and the k-integral running over all the intermediate scattering states.

Starting from $\mathcal{C}_{\rm BS}$, the intermediate BS are rather narrow resonances because

$$\Gamma_{\rm dec} \sim \alpha_{\rm eff}^3 E_B \ll E_B \ , \tag{A.7}$$

where E_B is a typical binding energy. This quick estimate, supported by the full numerical computation, suggests that $\mathcal{C}_{\rm BS}$ contribution is fully captured in the Narrow Width Approximation (NWA) for the intermediate BS. Therefore, neglecting the interference terms, one gets

$$(\sigma v_{\rm rel})_{2V} = \sum_m (\sigma v_{\rm rel})_{1V,m} {\rm BR}_{m\to n} \ , \tag{A.8}$$

which is exactly the single emission result.

To estimate the contribution from $\mathcal{C}_{\rm free}$ we need to estimate $\mathcal{I}_{\vec{q}\vec{k}}$ which encodes the contribution from intermediate continuum states. For simplicity, we stick to the abelian contribution which reads

$$\mathcal{I}_{\vec{q}\vec{k}} = \int r^2 {\rm d}r R_{\vec{k},1} \partial_r R_{\vec{q},0} \ . \tag{A.9}$$

The integral above can be split into small and large r regions, roughly separated by the Bohr radius $a_0 = \frac{1}{\alpha_{\rm eff} M_\chi}$

$$\begin{aligned} \mathcal{I}_{\vec{q}\vec{k}} &= \int_0^{a_0} r^2 {\rm d}r R_{\vec{k},1} \partial_r R_{\vec{q},0} + \int_{a_0}^{\infty} r^2 {\rm d}r R_{\vec{k},1} \partial_r R_{\vec{q},0} \\ &\sim \frac{1}{\alpha_{\rm eff} M_\chi \sqrt{kq}} + \frac{q}{(M_\chi \alpha_{\rm eff})^2} \delta(q-k) \ , \end{aligned} \tag{A.10}$$

which plugged into Eq. (A.6) gives an estimate to $\mathcal{C}_{\rm free}$. All in all, plugging these estimates in Eq. (A.5) and replacing $q = M_\chi v_{\rm rel}$ we get that the contribution from NLO exchange of continuum states behaves similarly to the ones estimated in Eq. (A.4) up to subleading terms in the $v_{\rm rel} < \alpha_{\rm eff}$ regime.

In conclusion, NLO corrections to BSF are suppressed by $\sim \alpha_{\rm eff}^3/64\pi$ with respect to the LO ones. As a consequence, the leading NLO contributions to the total annihilation cross-section are the ones correcting the LO SE. The latter are log-enhanced as detailed in Eq. (2.24) and first computed in [112] for the fermionic 3-plet and in [113] for generic EW n-plets.

Appendix B

The 7-plet Bound States in detail

In this Appendix, we detail the Majorana 7-plet BS dynamics, focusing on the differences with the 5-plet case.

The 7-plet has a richer bound states dynamics with respect to the 5-plet, essentially because of the additional layers of isospin and energy levels. As we will discuss here, keeping track of this dynamics is crucial to compute correctly the relic abundance.

The left panel of Fig. B.1 shows the relative importance of the different BS and the SE to the effective cross-section at fixed $T = 10^{-3} M_\chi$. As we can see, BSF accounts for most of the total cross-section. Compared to the 5-plet case, the new attractive isospin channels with $I = 7$ give a sizeable contribution to the 7-plet cross-section as well as the $2p$ states which were instead irrelevant for the 5-plet. In the right panel of Fig. B.1 we show how the details of the bound state dynamics are especially important at temperatures around the freeze-out (i.e. $z = 10^2$) where the effects of BS breaking due to interactions with the plasma are non negligible. This can be seen by comparing the behavior of the full computation of the effective cross-section (solid lines) against the BSF cross-section with zero ionization rate (i.e. $R_{BS} = 1$ in the notation of Eq. (2.19)). In particular taking $R_{BS} = 1$ yields an overestimate of the final thermal mass of about 6 TeV. Interestingly, we see that for $z = 10^3$ all the BSF rates approach the $R_{BS} = 1$ limit, signalling that the ionization rate is already heavily Boltzmann suppressed.

We now illustrate the details of the BS dynamics for the 7-plet. The general computation outlined around Eq. (2.12) is in general cumbersome, but it simplifies singling out the specific features of each BS. These are summarized in Fig. B.2. We now discuss them in turn, going from the largest to the smallest binding energy.

i) $1s_I$ and $2s_I$ states with isospin $I \leq 5$ annihilate fast into pairs of SM vectors and fermions, with rates $\Gamma_{\rm ann} \simeq \frac{\alpha_{\rm eff}^5}{n_B^2} M_\chi$. Since their decay rate can be neglected, the effective cross-section can easily be obtained from Eq. (2.20).

ii) The $1s_7$ BS cannot decay directly into SM pairs because of its large isospin so that its annihilation rate arises at NLO in gauge boson emission. Similarly, the decay to lower $1s$ states can only go through NLO processes or velocity-

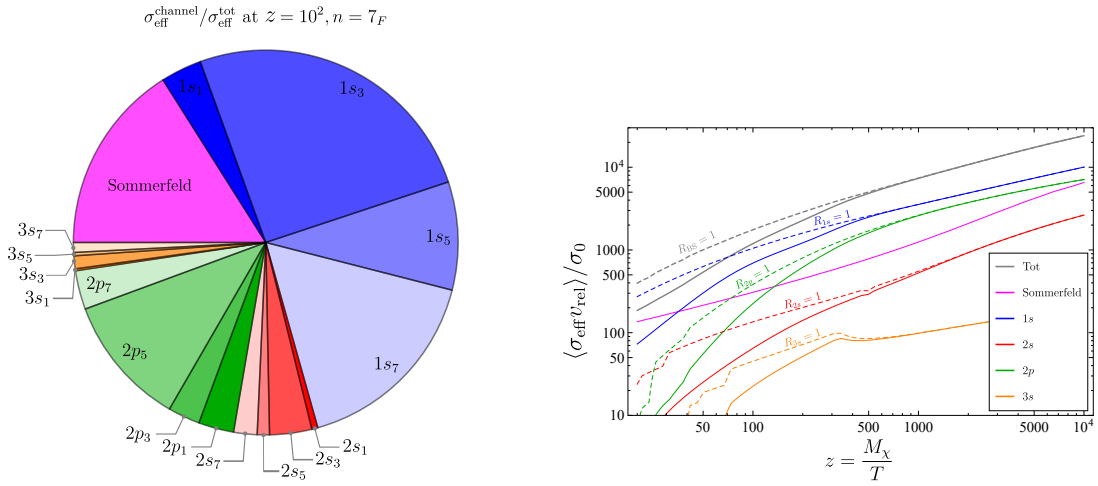

Figure B.1: Left: *Piechart showing the contributions to the 7-plet effective annihilation cross-section of each single BS channel, together with the SE, at fixed* $T = 10^{-2} M_\chi$ *(i.e.* $z = 10^2$*).* **Right:** *Temperature dependence of the different contributions to the 7-plet effective cross-sections. Each BS channels is summed over the different isospins.*

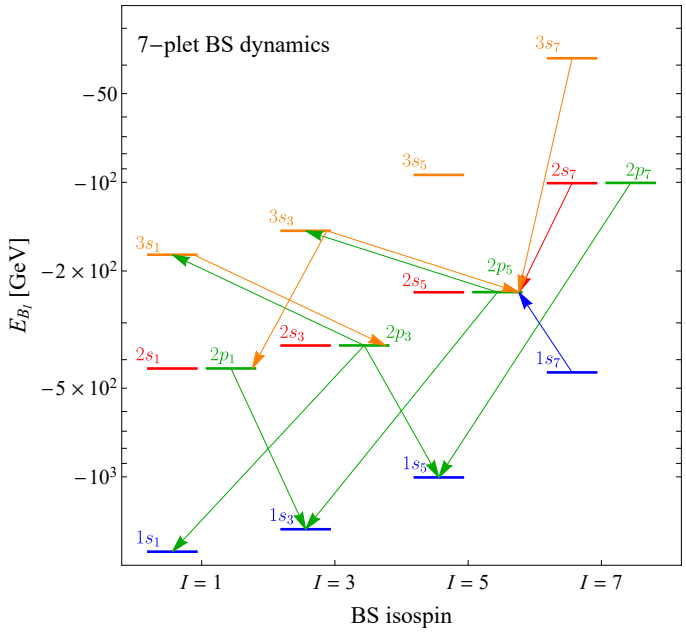

Figure B.2: *BS energy levels for the 7-plet: blue* $n = 1$*, red* $n = 2$ *with* $L = 0$*, green* $n = 2$ *with* $L = 1$ *and orange* $n = 3$*. The arrows indicate the decay rate of each state. BS with no lines attached have an annihilation rate at least one order of magnitude larger than the decay rate.*

suppressed magnetic transitions. As a consequence, this BS can only be excited to $2p_5$ at LO, and its effective cross-section can be written in terms of the one of the $2p_5$:

$$R_{1s_7}(z) = \frac{\langle \Gamma_{1s_7 \to 2p_5} \rangle}{\langle \Gamma_{1s_7 \to 2p_5} \rangle + \langle \Gamma_{1s_7,\text{break}} \rangle} R_{2p_5}(z) \ , \tag{B.1}$$

where the excitation rate can be written in terms of the decay rate $\Gamma_{I \to J} \simeq g_I/g_J \Gamma_{J \to I} e^{-\frac{\Delta E}{T}}$ times the probability of finding a vector in the plasma with energy of order ΔE. Because of the small energy required from the plasma compared to ionization, excitations still occur long after the ionizations have gone out of equilibrium.

iii) The $2s_7$ has a suppressed annihilation rate to SM like the $1s_7$, but it quickly decays to the $2p_5$ at LO in vector boson emission so that we have

$$R_{2s_7}(z) = \frac{\langle \Gamma_{2s_7 \to 2p_5} \rangle}{\langle \Gamma_{2s_7 \to 2p_5} \rangle + \langle \Gamma_{2s_7,\text{break}} \rangle} R_{2p_5}(z) \ . \tag{B.2}$$

iv) The annihilation rates into SM state of the $2p_I$ BS are suppressed by α_{eff}^2 compared to the ones of the $2s_I$ BS. Their dynamics is then dominated by the decay (excitation) rates into lower (higher) $s-$orbital BS which scale as $\Gamma_{\text{dec}} \sim \alpha_{\text{eff}}^5 M_\chi$. A simple example of this dynamics is provided by the two-state system $2p_1 - 1s_3$ where $2p_1$ dominantly decays to $1s_3$, which promptly annihilates to SM. The effective cross-section of $2p_1$ reads

$$R_{2p_1}(z) = \frac{\langle \Gamma_{2p_1 \to 1s_3} \rangle}{\langle \Gamma_{2p_1 \to 1s_3} \rangle + \langle \Gamma_{2p_1,\text{break}} \rangle} R_{1s3}(z) \ , \tag{B.3}$$

as we would intuitively expected. The other $2p$ states have more intricated chains, which involve also excitations $3s$ states.

v) We also include $3s_I$ BS which annihilate directly to SM for $I \leq 5$ and decay into $p-$orbitals states.

Finally, we checked that p states with $n > 2$, s states with $n > 3$, and BS with $I = 9$ have a negligible impact on the cosmological evolution.

Appendix C

Additional Details on Bound State Production at Future Colliders

In this Appendix we discuss additional signatures related to bound state production at future colliders. In particular, we consider the production of BS other than the target ${}^n s_3$ in Sec. C.1 and the expected signal from intra-BS decays in Sec. C.2.

C.1 Production of other bound states from VV

The charged components $B_\mu^\pm$ of the isospin triplet of bound states are produced with a relatively large cross section, given that the partonic neutrino component of a $\mu^\pm$ beam is peaked at energy fraction $x = 1$ [188], in view of soft $W^\pm$ emission. By running a bit above the peak, the state with $n = 1$ is produced as $\mu^+\mu^- \to B_\mu^\pm W_\mu^\mp$ with fb-scale cross section, as shown by the blue curve in Fig. C.1.

Finally, we mention that the state ${}^3 d_3$ too has the same quantum numbers as electroweak vectors and can thereby be produced directly from $\mu^+\mu^-$ collision; however its annihilation rate (see bottom row of table 2.3) is highly suppressed by $\alpha_2^{5+2\ell}$ in view of $\ell = 2$ and we neglect it.

The other bound states annihilate to weak vectors and can thereby be produced through associated production via vectors. Then, the energy spread in the effective collision energy becomes large, $\sigma_E \sim \sqrt{s}$, and the cross sections small. These more general processes can be computed using automated codes [124], approximating bound states as particles with effective couplings to their decay products that reproduce the widths [189] computed in table 2.3. For example, the ground pseudo-scalar bound state ${}^1 s_1$ with $I = 1$ can be written as a scalar singlet B coupled as $B\epsilon_{\mu\nu\mu'\nu'} V^a_{\mu\nu} V^a_{\mu'\nu'}$. The pseudo-scalar bound state ${}^1 s_5$ with $I = 5$ can be written as a scalar $B_{aa'}$ in the symmetric trace-less representation of $\mathrm{SU}(2)_L$ coupled as $B_{aa'}\epsilon_{\mu\nu\mu'\nu'} V^a_{\mu\nu} V^{a'}_{\mu'\nu'}$.

We focus on the ground state ${}^1 s_1$, as it has the largest annihilation rate. It can be produced via scatterings of SM electroweak vectors, $\gamma\gamma \to B_{1s_1}$, $\gamma\mu^\pm \to B_{1s_1}\mu^\pm$, $\mu^+\mu^- \to B_{1s_1}\mu^+\mu^-$, $\mu^+\mu^- \to B_{1s_1}\nu_\mu\bar{\nu}_\mu$. Resonant production is not possible and

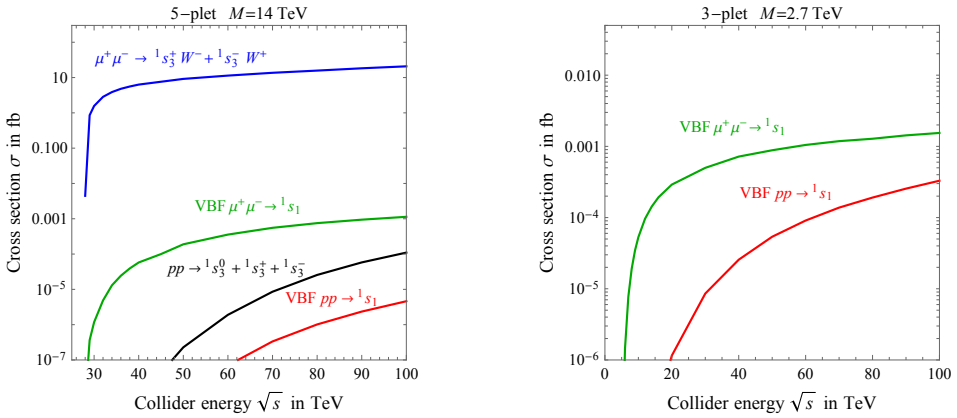

Figure C.1: *Cross sections for the production of some bound states of the Minimal DM fermionic 5-plet with constituent mass $M = 14\,\text{TeV}$ (left) and of the fermionic 3-plet with $M = 2.7\,\text{TeV}$ (right) at a $\mu^+\mu^-$ collider and at a pp collider.*

one thereby must run at higher $\sqrt{s} > 2M_\chi$: the green curve in Fig. C.1 shows that, as expected, the production cross section is much smaller.

The red curve in Fig. C.1 shows its analogous production cross sections at a pp collider, which is even smaller given that vector partons in a p beam have lower energy than in a μ beam. For completeness, the black curve in Fig. C.1 shows the cross section for production at a pp collider of the ${}^1s_3$ bound state discussed in the previous section. We do not discuss the backgrounds.

Furthermore, we consider a Wino-like Minimal DM fermionic triplet. The DM abundance is reproduced thermally for $M_\chi = 2.7\,\text{TeV}$. At this mass only one ${}^1s_1$ bound state exists with $E_B \approx 68\,\text{MeV}$ and $\Gamma_B = 8\alpha_2^5 M_\chi \approx 4\,\text{MeV}$ [26]. This bound state cannot be produced with a resonantly-enhanced cross section. Fig. C.1b shows its production cross section at a muon or pp collider.

C.2 Decays of bound states and their collider signals

In this section we describe the computation of the bound state decays listed in table 2.3, having in mind that we seek characteristic collider signals produced by decays among bound states. The leading-order decays $B \to B'V$ proceed through the emission of a weak vector boson V, which is often a photon as the phase space for W, Z emission is often closed. Such process dominantly occurs via electric dipole transitions, although magnetic dipole transitions happen to be important in cases where selection rules forbid electric dipole transitions. We compute bound states in the $\text{SU}(2)_L$-symmetric approximation, so that bound states of two 5-plets have two indices ij in the 5 representation, that can be converted into isospin eigenstates $B_{\tilde{I}\tilde{I}_3}$ through Clebsch-Gordan coefficients: $B_{ij} = C_{ij}^{\tilde{I}\tilde{I}_3} B_{\tilde{I}\tilde{I}_3}$.

- The effective interaction hamiltonian for the electric dipole at leading order is

$$H_{\rm el} = -\frac{g_2}{M_\chi}[\vec{A}^a(x_1)\cdot\vec{p}_1\, T^a_{i'i}\delta_{jj'} + \vec{A}^a(x_2)\cdot\vec{p}_2\, \bar{T}^a_{j'j}\delta_{ii'}] + g_2\alpha_2[\vec{A}^a(0)\cdot\hat{r}]T^b_{i'i}\bar{T}^c_{j'j}f^{abc} \tag{C.1}$$

  leading to the following selection rules: $|\Delta\tilde{I}| = 1$, $|\Delta\ell| = 1$, $\Delta S = 0$. Decay rates are obtained as

$$\Gamma({}^2p_{\tilde{I}} \to {}^1s_{\tilde{I}'} + V^a) = \frac{16}{9I_{2p}}\frac{\alpha_2 k}{M_\chi^2}\sum_{\tilde{I}_3\tilde{I}'_3}\left|\int r^2{\rm d}r\, R_{\tilde{I},2p}\left(C_{\mathcal{J}}^{a\tilde{I}_3\tilde{I}'_3}\partial_r - C_{\mathcal{T}}^{a\tilde{I}_3\tilde{I}'_3}\frac{\alpha_2 M_\chi}{2}\right)R_{\tilde{I}',1s}\right|^2 \tag{C.2}$$

$$\Gamma({}^3s_{\tilde{I}} \to {}^2p_{\tilde{I}'} + V^a) = \frac{16}{3I_{3s}}\frac{\alpha_2 k}{M_\chi^2}\sum_{\tilde{I}_3\tilde{I}'_3}\left|\int r^2{\rm d}r\, R_{\tilde{I}',2p}\left(C_{\mathcal{J}}^{a\tilde{I}_3\tilde{I}'_3}\partial_r + C_{\mathcal{T}}^{a\tilde{I}_3\tilde{I}'_3}\frac{\alpha_2 M_\chi}{2}\right)R_{\tilde{I},3s}\right|^2 \tag{C.3}$$

  where r is the radius, $R(r)$ are normalized radial wave-functions, k is the spatial momentum of V, I is the isospin of the initial bound state, and

$$C_{\mathcal{J}}^{a\tilde{I}_3\tilde{I}'_3} = \frac{1}{2}{\rm Tr}\left[C^{\tilde{I}'\tilde{I}'_3}\left\{C^{\tilde{I}\tilde{I}_3}, T^a\right\}\right], \qquad C_{\mathcal{T}}^{a\tilde{I}_3\tilde{I}'_3} = i{\rm Tr}\left[C^{\tilde{I}'\tilde{I}'_3}T^bC^{\tilde{I}\tilde{I}_3}T^c\right]f^{abc}. \tag{C.4}$$

- The effective interaction hamiltonian for the magnetic dipole at leading order is (see e.g. [190])

$$H_{\rm mag} = -\frac{g_2}{2M_\chi}[T^a_{i'i}\delta_{jj'}\vec{\sigma}\cdot\vec{B}^a(x_1) + \bar{T}^a_{j'j}\delta_{ii'}\vec{\sigma}\cdot\vec{B}^a(x_2)] + \cdots \tag{C.5}$$

  leading to the following selection rules: $|\Delta\tilde{I}| = 1$, $\Delta\ell = 0$, $|\Delta S| = 1$. Decay rates are obtained as [190]

$$\Gamma({}^{n_i}s_{\tilde{I}_i} \to {}^{n_f}s_{\tilde{I}_f} + V^a) = \frac{2^3}{I_i}\frac{\alpha_2 k^3}{M_\chi^2}\sum_{\tilde{I}_{3,i}\tilde{I}_{3,f}}\left|C_{\mathcal{J}}^{a\tilde{I}_{3,i}\tilde{I}_{3,f}}\int r^2{\rm d}r\, R_{n_is_{\tilde{I}_i}}R_{n_fs_{\tilde{I}_f}}\right|^2 \tag{C.6}$$

  with no contribution from the omitted non-abelian term in Eq. (C.5).

- Higher-order interactions lead to multiple-vector emission, with suppressed rates that turn out to be negligible.

As discussed in Sec. 2.4.3, the lightest bound state that can be produced resonantly is the neutral component of ${}^1s_3$. This is the only component of ${}^1s_3$ that can decay ($W^\pm$ emission from charged components of ${}^1s_3$ is kinematically blocked) to ${}^1s_1\gamma$ via a magnetic transition with a rate $\Gamma_{\rm dec} = 3\times 4.6\,{\rm keV}$. Such rate is of order $\alpha_2^6\alpha_{\rm em}M_\chi$, where an α_2^2 factor arises from the γ phase space; another α_2^4 from the magnetic field $\vec{B}^a$; the $\alpha_{\rm em}$ from photon emission. Taking into account its annihilation rate, the neutral component of the ${}^1s_3$ bound state decays into a monochromatic γ with energy $E_\gamma \approx 38\,{\rm GeV}$ with branching ratio ${\rm BR}_{\rm dec} \approx 9\ 10^{-5}$. This corresponds to 19 events in a run with baseline $\sigma_E = 10^{-3}$ and luminosity $\mathcal{L} = 90/\,{\rm ab}$.

Higher order states are produced with a lower cross section, that scales as $\Gamma_{\rm ann} \propto 1/n^3$. Nevertheless, such states could give a higher rate of decay events, proportional to $\sigma\ {\rm BR}_{\rm dec} \propto \Gamma_{\rm ann}\times\Gamma_{\rm dec}/\Gamma_{\rm ann} \propto \Gamma_{\rm dec}$.

- At $n = 2$, the ${}^2s_3$ bound state similarly decays magnetically, with the difference that it can now also emit massive weak bosons, and decay into multiple states ${}^1s_1$, ${}^1s_5$ (we neglect decays in ${}^2s_1$ because their rate is negligibly small, at eV level). The neutral component of ${}^2s_3$ decays emitting a γ with rate $\Gamma_{\rm dec} \approx 2.0\,{\rm keV}$ and emitting a Z with rate $\Gamma_{\rm dec} \approx 1.7\,{\rm keV}$; charged components have similar decay rates. In view of the lower binding energy and wave-function overlap, ${}^2s_3$ thereby gives a similar number of decay events as ${}^1s_3$. As a result, the γ decays of the ${}^2s_3$ neutral component produces two distinctive single-photon lines, at $E_\gamma \approx 105\,{\rm GeV}$ and $13\,{\rm GeV}$, as well as Z bosons.
- At $n = 3$, the ${}^3s_3$ bound state can decay electrically into ${}^2p_{1+5}\gamma$, with a rate of order $\alpha_2^4\alpha_{\rm em}M_\chi$ (where an α_2^2 factors arises from the γ phase space; another α_2^2 from the dipole matrix element; the $\alpha_{\rm em}$ from photon emission). The numerical coefficient turns however to be small, and the decay rate is again around a keV. More precisely, only the neutral component can decay into ${}^2p_1$, and all components decay equally into ${}^2p_5$. Thereby, table 2.3 implies that the decay rate of the neutral component is $\Gamma_{\rm dec} = (3 \times 0.003 + 0.005)\alpha_2^4\alpha_{\rm em} \approx 1.7\,{\rm keV}$. The ${}^2p_{1+5}$ bound states next dominantly decay via a large electric dipole into ${}^1s_3$, that annihilates. This process thereby gives a set of multiple-photon lines, with $E_\gamma \approx \{18\,{\rm GeV}, 60\,{\rm GeV}\}$, and with $E_\gamma \approx \{0.5\,{\rm GeV}, 79\,{\rm GeV}\}$. As signal events have very distinctive $\gamma\gamma$ signatures, backgrounds can be strongly reduced.

For completeness, in table 2.3 we also computed decay rates of other states that cannot be produced resonantly with large rates. Thereby we do not discuss them. All above numbers assume $M_\chi = 13.7\,{\rm TeV}$ and need to be recomputed otherwise.

Appendix D

Complex WIMP classification

In this appendix we give further details on our complex WIMP classification. In Sec. D.1 we explicitly classify the possible UV operators, substantiating the result of Sec. 3.1. In Sec. D.2 we give the results for scalar WIMPs.

D.1 UV Operators

In Sec. 3.1 we showed that in order to make complex WIMPs with $Y \neq 0$ viable, new UV sources of splitting between the charged and neutral components and among the neutral components are necessary. In Eq. (3.1) we showed how the neutral splitting can be generated by $\mathcal{O}_0$ and the charged-neutral splitting by $\mathcal{O}_+$. Here we take a step back and investigate the generality of this choice.

The general form of an operator responsible for a Majorana mass term for χ_N after EWSB is

$$\overline{\chi}(y_0 + y_{0,5}\gamma_5)\mathcal{I}\chi^c H^{4Y} \ , \tag{D.1}$$

where the H^{4Y} is necessary to match the hypercharge of the χ^2 piece, while $\mathcal{I}$ is a $\mathrm{SU}(2)_L$ tensor. We are crucially assuming that the Higgs is the only scalar picking a VEV after EWSB. Under this assumption, since the Higgs is a boson, the only surviving $\mathrm{SU}(2)_L$ structure is the totally symmetric combination. This can be seen as the symmetric combination of $2Y$ Higgs pairs in the isotriplet representation (the isosinglet is antisymmetric and vanishes identically), so that we are left with $\mathcal{O}_0$ defined in Eq. (3.1) and its axial counterpart with the γ_5 insertion. The latter can be shown to give only subleading contributions to the mass splitting between the neutral components of χ. Assuming y to be real, the shift on δm_0 induced by $y_{0,5} \neq 0$ with respect to its expression in Eq. (3.3) is

$$\delta m_0 \to \delta m_0 \sqrt{1 + 4\Re[y_{0,5}]^2 \frac{\Lambda_{\mathrm{UV}}^2}{M_{\mathrm{DM}}^2} \left(\frac{v}{\sqrt{2}\Lambda_{\mathrm{UV}}}\right)^{8Y}} \ , \tag{D.2}$$

which is highly suppressed for $\Lambda_{\mathrm{UV}} > M_{\mathrm{DM}} > v$. The operator $\mathcal{O}_0$ in Eq. (3.1) is then the dominant contribution to the inelastic splitting among the neutral components.

The isospin structure and field content of $\mathcal{O}_+$ is already the minimal required to generate additional splitting between the charged components, the only possibility is again to change its chiral structure writing the general operator inducing charged-neutral splitting as

$$\overline{\chi} T^a (y_+ + y_{+,5}\gamma_5)\chi H^\dagger \sigma^a H \ . \tag{D.3}$$

Similarly to the neutral case, the γ_5 insertion leads to a subleading shift in the mass splittings with respect to the value of Eq. (3.11)

$$M_Q^2 \to M_Q^2 + y_{+,5}^2 \frac{v^4}{16 M_{\rm DM}^2 \Lambda^2}(Q-Y)^2 \ . \tag{D.4}$$

Finally, we comment on the implications on DD signals. Both operators with the γ_5 insertions give additional contributions to the SI cross-section and match to the effective operators:

$$\begin{aligned}\mathscr{L}_{\rm eff}^{\rm SI} =& \tilde{f}_q m_q \bar{\chi} i\gamma_5 \chi \bar{q} q + \frac{\tilde{g}_q}{M_{\rm DM}} \bar{\chi} i\partial^\mu \gamma^\nu i\gamma_5 \chi \mathcal{O}^q_{\mu\nu} \\ &+ \tilde{f}_G \bar{\chi} i\gamma_5 \chi G_{\mu\nu} G^{\mu\nu}.\end{aligned}$$

However, all these operators are strongly momentum-suppressed [191, 192], so that their corrections to $\sigma_{\rm SI}$ are expected to be $(q/m_N)^2 \sim 10^{-6}$ smaller than those from Eq. (2.52), and thus negligible.

D.2 Complex Scalar WIMPs

Following the discussion in Sec. 3.1 for the fermions, supported by the previous Appendix D.1, the minimal Lagrangian for a scalar complex WIMP is

$$\begin{aligned}\mathscr{L}_{\rm S} &= |D_\mu \chi|^2 - M_\chi |\chi|^2 + \frac{y_0}{\Lambda_{\rm UV}^{4Y-2}} \mathcal{O}_0^S + y_+ \mathcal{O}_+^S + \text{h.c.}\,, \\ \mathcal{O}_0^S &= \frac{1}{2(4Y)!}\left(\chi^\dagger (T^a)^{2Y} \chi^c\right)\left[H^{c\dagger}\frac{\sigma^a}{2} H\right]^{2Y}\,, \\ \mathcal{O}_+^S &= -\chi^\dagger T^a \chi H^\dagger \frac{\sigma^a}{2} H\,.\end{aligned} \tag{D.5}$$

Conversely to the fermionic case, no additional operators can be written to generate the fundamental mass splitting. The neutral and charged *squared* mass splitting, $\mu_Q^2 = M_Q^2 - M_{\rm DM}^2$, can be written as

$$\begin{aligned}\mu_0^2 &= 4 y_0 c_{nY0} \Lambda_{\rm UV}^2 \left(\frac{v}{\Lambda_{\rm UV}\sqrt{2}}\right)^{4Y}\,, \\ \mu_Q^2 &= \frac{\mu_0^2}{2} + 2 M_{\rm DM}\delta_g Q^2 + \text{sgn}(Q)\sqrt{\left(\frac{4Y\delta_g M_{\rm DM}}{\cos\theta_W} - \frac{y_+ v^2}{4}\right)^2 Q^2 + \frac{\mu_0^2}{4}\frac{c_{nYQ}^2}{c_{nY0}^2}}.\end{aligned} \tag{D.6}$$

The linear mass splittings, $\delta m_Q = M_Q - M_{\rm DM}$, are then given by $\delta m_Q = \mu_Q^2/(2M_{\rm DM})$. Notice that for $Y = 1/2$ all the operators are renormalizable and any dependence on the cutoff disappears.
The lower bound on δm_0 from DD is identical to that for fermions, since $\sigma_{\rm SI}$ does not change. Instead, the BBN bound differs since the one-loop decay channel $\chi_0 \to \chi_{\rm DM}\gamma$ now is now heavily suppressed with respect to the three-body decays. As a consequence, the BBN condition becomes

$$\Gamma_{\chi_0} \equiv \Gamma_{\bar{\nu}\nu} + \Gamma_{\bar{e}e} > 6.58 \times 10^{-25}\ \text{GeV}\,, \tag{D.7}$$

which explains why the bound on $\delta m_0^{\rm min} \simeq 4-5$ MeV for scalars is so much stronger than the one for fermions, as shown in Fig. 3.1. For $Y \neq 1/2$, the lower bound on δm_0 sets the upper bound of the allowed window for $\Lambda_{\rm UV}$

$$10\, M_{\rm DM} < \Lambda_{\rm UV} \leq \left(\frac{2y_0 c_{nY} v^{4Y}}{2^{2Y}\delta m_0^{\rm min} M_{\rm DM}}\right)^{\frac{1}{4Y-2}}\,, \tag{D.8}$$

which is the analogous of Eq. (3.13) for scalar WIMP. Once set $y_0 = (4\pi)^{4Y}$ to its NDA maximal value and given the scaling $M_{\rm DM} \sim n^{5/2}$ Eq. (D.8) can be used to determine the viable EW multiplets. It turns out that the allowed multiplet are the same as for fermions, *i.e.* all even $n_{1/2}$ plus 3_1 and 5_1.

Finally, we discuss DM stabiity for scalars. All the $Y = 1/2$ scalars are never accidentally stable, since DM decay can be induced by the renormalizable operator $\chi^2\chi^\dagger H^c$. Similarly, for 3_1 we can write $\chi^\dagger H^2$, while for 5_1 the lowest dimensional operators are:

$$\mathscr{L} = \frac{C_1}{\Lambda_{\rm UV}}\chi^\dagger H^2 (H^\dagger H) + \frac{C_2}{\Lambda_{\rm UV}}(\chi^\dagger\chi)(\chi^\dagger H^2)\,, \tag{D.9}$$

which ensures stability for $\Lambda_{\rm UV} > 10^{21} M_{\rm DM}$, way larger than $\Lambda_{\rm UV} < 20 M_{\rm DM}$ from δm_0 perturbativity.

Results for the collider reach on the scalars are given in Fig. F.3.

Appendix E

Millicharged WIMPs

Complex WIMPs with $Y = 0$ have an unbroken $U(1)$ flavor symmetry which can be gauged by a new dark photon. Generically the dark photon would mix with the visible one through a kinetic mixing operator $\epsilon FF'$ and the complex WIMP would acquire a EM charge ϵ. In this scenario the dark gauge symmetry makes the DM accidentally stable as noticed in Ref. [35] at the price of giving up charge quantization. Here we want to summarize the freeze-out predictions and the basic phenomenology of millicharged WIMPs in the limit of very small ϵ (i.e. $\epsilon < 10^{-10}$) when their phenomenology resemble the one of the real WIMPs discussed in Ref. [83].

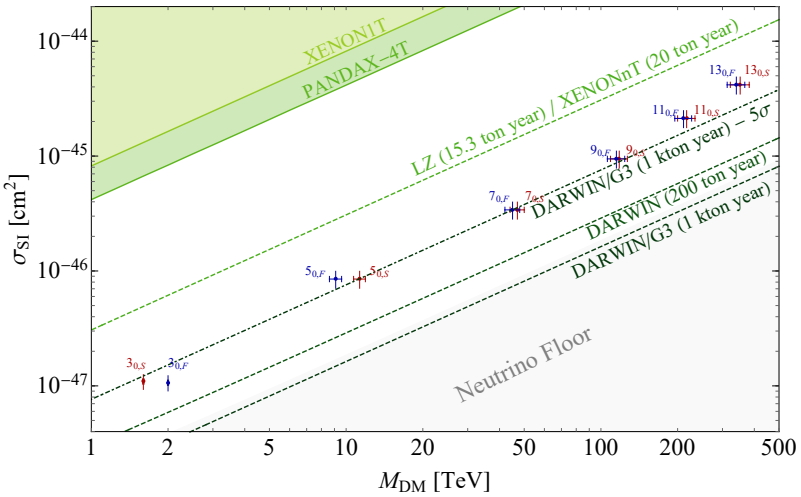

Figure E.1: *Expected SI cross-sections for different millicharged complex WIMPs with* $\epsilon \lesssim 10^{-10}$. *The* **blue dots** *correspond to Dirac WIMPs and the* **red dots** *to complex scalar WIMPs. The vertical error bands correspond to the propagation of LQCD uncertainties on the elastic cross-section (Eq. (2.56)), while the horizontal error band comes from the uncertainty in the theory determination of the WIMP freeze out mass in Table E.1. The* **light green** *shaded region is excluded by the present experimental contraints from XENON-1T [52] and PandaX-4T [53], the* **green dashed** *lines shows the expected 95% CL reach of LZ/Xenon-nT [54, 55] and DARWIN [41, 50].*

Concerning the freeze-out dynamics, the only difference between real and millicharged

WIMPs is in the existence of BS with $P_{\rm BS} = (-1)^{L+S+\frac{I-1}{2}} = -1$ formed by $\bar{\chi}\chi$ pairs of millicharged WIMPs. These are forbidden by the spin-statistic properties of the $\chi\chi$ wave function for real WIMPs. Since $P_{\rm BS}$ is preserved by dipole interactions for $Y = 0$, to leading order no transitions can occur between states with opposite $P_{\rm BS}$ and excited BS with $P_{\rm BS} = -1$ will dominantly decay to $1s$ and $2s$ states with the same $P_{\rm BS}$. The latter have small decay widths with respect to their $P_{\rm BS} = 1$ counterparts. $ns_1^{S=1}$ and $ns_5^{S=1}$ annihilate into four vectors with a rate

$$\Gamma(ns_{1,5}^{S=1} \to VVVV) \simeq \frac{\alpha_{\rm eff}^4}{16\pi^2 M_{\rm DM}^2} \frac{|R_{n0}(0)|^2}{M_{\rm DM}^2}\,, \tag{E.1}$$

while $ns_3^{S=0}$ annihilates into three vectors with rate:

$$\Gamma(ns_3^{S=0} \to VVV) \simeq \frac{\alpha_{\rm eff}^3}{4\pi M_{\rm DM}^2} \frac{|R_{n0}(0)|^2}{M_{\rm DM}^2}\,. \tag{E.2}$$

where $R_{n0} \sim (\alpha_{\rm eff} M_{\rm DM})^{3/2}$ is the radial wave function of the BS at the origin. As noticed in Ref. [35] for the millicharged 3-plet a large resonance in the Sommerfeld enhancement leads to two different freeze out predictions. We summarize our freeze out predictions in Table E.1.

DM spin	n_ϵ	$M_{\rm DM}$ (TeV)	$\Lambda_{\rm Landau}/M_{\rm DM}$	$(\sigma v)_{\rm tot}^{J=0}/(\sigma v)_{\rm max}^{J=0}$
Complex scalar	3	$1.60 \pm 0.01 - 2.4^*$	$> M_{\rm Pl}$	-
	5	11.3 ± 0.6	$> M_{\rm Pl}$	0.003
	7	47 ± 3	2×10^6	0.02
	9	118 ± 9	110	0.09
	11	217 ± 17	7	0.25
	13	352 ± 30	3	0.6
Dirac fermion	3	$2.0 \pm 0.1 - 2.4^*$	$> M_{\rm Pl}$	-
	5	9.1 ± 0.5	4×10^6	0.002
	7	45 ± 3	80	0.02
	9	115 ± 9	6	0.09
	11	211 ± 16	2.4	0.3
	13	340 ± 27	1.6	0.7

Table E.1: *Freeze-out mass predictions for millicharged WIMP DM. The annihilation cross-section includes both the contribution of SE and BSF. For the triplets, a second prediction, denoted with a *, for the thermal mass is present due to the emergence of a large resonance in the Sommerfeld enhancement for $M_{DM} \approx 2.4$ TeV. We provide a measure of how close the DM annihilation cross-section is to the unitarity bound for s-wave annihilation $(\sigma v)_{max}^{J=0} = 4\pi/M_{DM}^2 v$. We derive the scale where EW gauge coupling will develop a Landau pole by integrating-in the WIMP multiplet at its freeze-out mass.*

For completeness, in Fig. E.1 we show the SI scattering cross-section of DM on xenon nuclei for the different millicharged candidates. This cross-section is identical

to that computed for real candidates with $\epsilon \lesssim 10^{-10}$ [35, 91], while larger ϵ would open up new opportunities for direct detection (see e.g. Fig 1 of [35]). From Fig. E.1 we see that even in the worst case scenario of very small millicharge large exposure experiments will be able to fully probe millicharged WIMPs with 200 ton-year exposure. The heavier multiplets could be also firmly discovered at DARWIN with kiloton exposure.

Appendix F

The scalar WIMPs at future lepton colliders

Probing scalar WIMPs with typical missing mass searches is quite hard. This is due to multiple reasons. First, the scalar production cross-sections are roughly one order of magnitude smaller than for fermions with same n, as shown on the left of Fig. F.1 for real candidates. A factor of 4 suppression comes from the lower number of degrees of freedom for scalar final states, while the remaining suppression comes from a velocity suppressed production cross-section compared to the fermionic case. Since the reach is a very slow function of the mass of the WIMP M_χ, a reduction of the signal cross-section implies a drastic change in the reach. The example of the real WIMPs is shown in Fig. F.1. ii) The scalar WIMPs have typically larger freeze-out masses compared to fermionic WIMPs with same EW charge n.

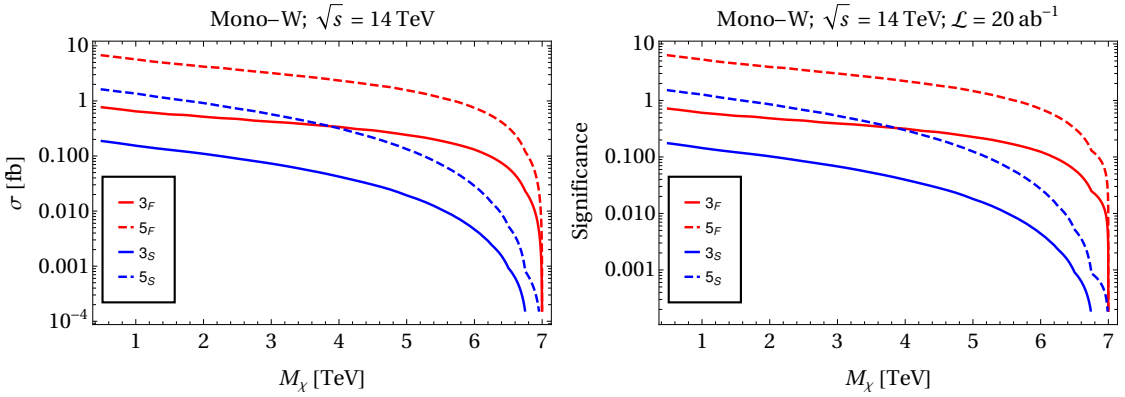

Figure F.1: Left: *Drell-Yan Mono-W cross-section for* $\sqrt{s} = 14\,\text{TeV}$. **Right:** *Significance of the mono-W search for* $\sqrt{s} = 14\,\text{TeV}$. *In both plots, the only cuts applied are* $|\eta_W| < 2.5$ *(geometric acceptance) and* $\text{MIM} > 2M_\chi$. *Both plots refer to real WIMPs.*

All in all, scalar WIMPs give dimmer signals at colliders and are generically heavier than fermionic WIMP. It is thus not surprising that the results expected from collider searches of scalar WIMPs, shown in Fig. F.2 for real scalars and in Fig. F.3 for complex ones, are far less exciting than those for fermions in Figs. 2.5 and 3.5, respectively.

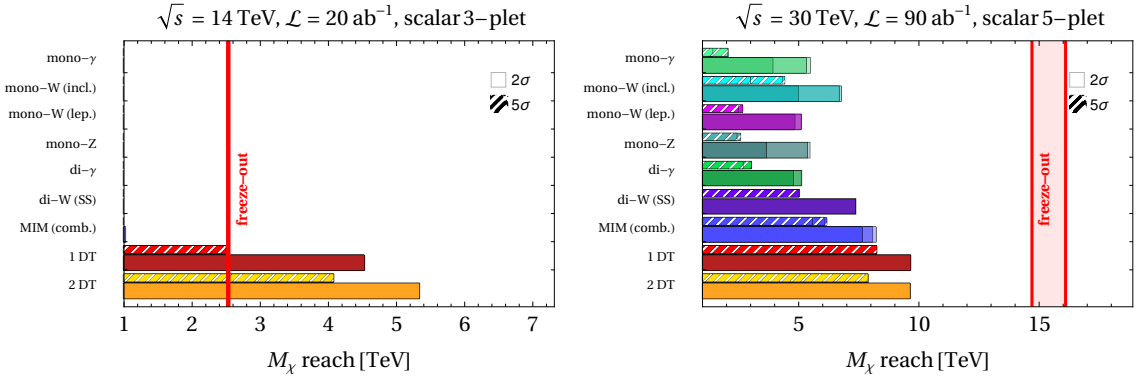

Figure F.2: *Different bars show the reach at* 2σ *(full wide) and at* 5σ *(hatched thin) on the WIMP mass at a muon collider with baseline luminosity given by Eq. (2.26) for the different search channels discussed in Sec. 2.4.1: mono-gamma, inclusive mono-W, charged mono-W, mono-Z, di-gamma, same-sign di-W , the combination of all these MIM channels (blue). We also show the reach of disappearing tracks as discussed in Sec. 2.4.2: at least 1 disappearing track (red), or exactly 2 tracks (orange). All the results are obtained assuming systematic uncertainties to be: 0 (light), 1 ‰(medium), or 1% (dark). The vertical red lines show the freeze-out prediction band.* **Above:** *Scalar 3-plet for* $\sqrt{s} = 14\,\text{TeV}$ **Below:** *Scalar 5-plet for* $\sqrt{s} = 30\,\text{TeV}$.

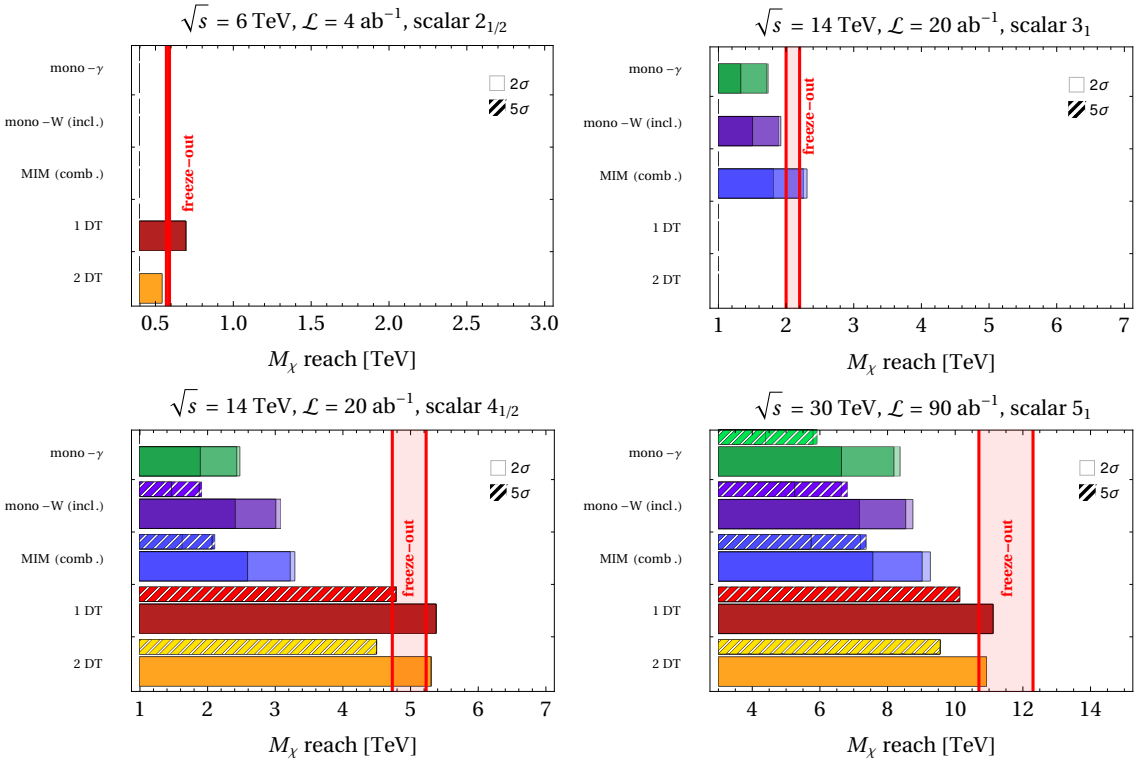

Figure F.3: *Results for complex scalar WIMPs. Same notation as in Fig. F.3.*

The overall picture in the landscape of possible beam energy and luminosity options for mono-W searches is displayed in Fig. F.4 for both real scalar 3-plet and 5-plet. In Fig. F.6, instead, we show the results for the scalar 3_1, $4_{1/2}$ and 5_1, respectively, in the case of mono-γ and mono-W searches. In the relevant $\sqrt{s}-$luminosity plane,

instead, the scalar $2_{1/2}$ never reaches the 2σ significance. All in all, at variance with the fermionic cases presented in Figs. 2.4, 3.6 and 3.7, the potential to probe scalar WIMPs with mono-X signals is very limited.

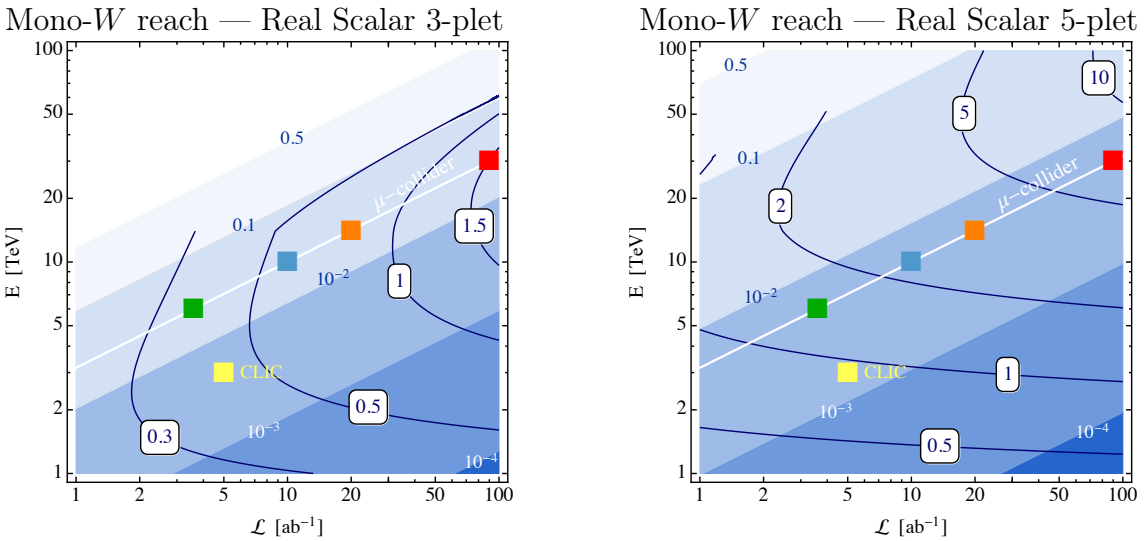

Figure F.4: *Same as Fig. 2.4, but for real scalar WIMPs.* **Left:** *Scalar 3-plet.* **Right:** *Scalar 5-plet.*

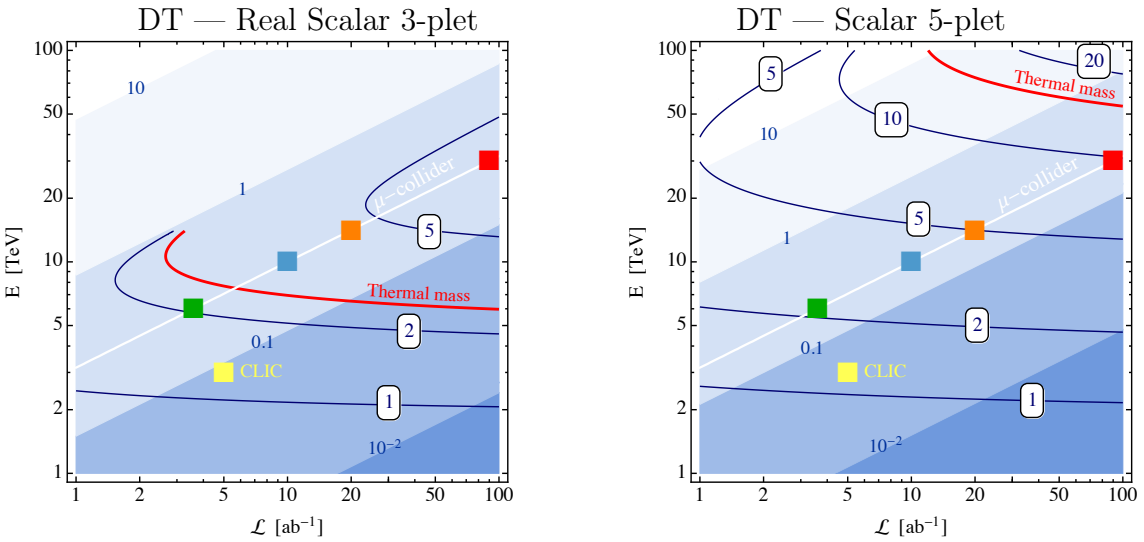

Figure F.5: *Same as Fig. 2.6, but for real scalar WIMPs.* **Left:** *Scalar 3-plet.* **Right:** *Scalar 5-plet.*

We stress that our results are based purely on Drell-Yan production of χ, which accounts perfectly for the total production rate of WIMPs of mass comparable with $\sqrt{s}$. For significantly lighter WIMPs it is possible to add further production modes and discovery channels, such as production by vector boson fusion and mono-muon channels studied for lighter fermionic WIMPs [92], which may result in a bound for light enough scalar WIMPs. In Fig. F.7 we plotted the cross-sections for scalar $\chi\chi$ production in W-fusion (as a representative for VBF modes) and Drell-Yan as a function of M_χ. It can be seen that the VBF cross-section decreases quickly, while

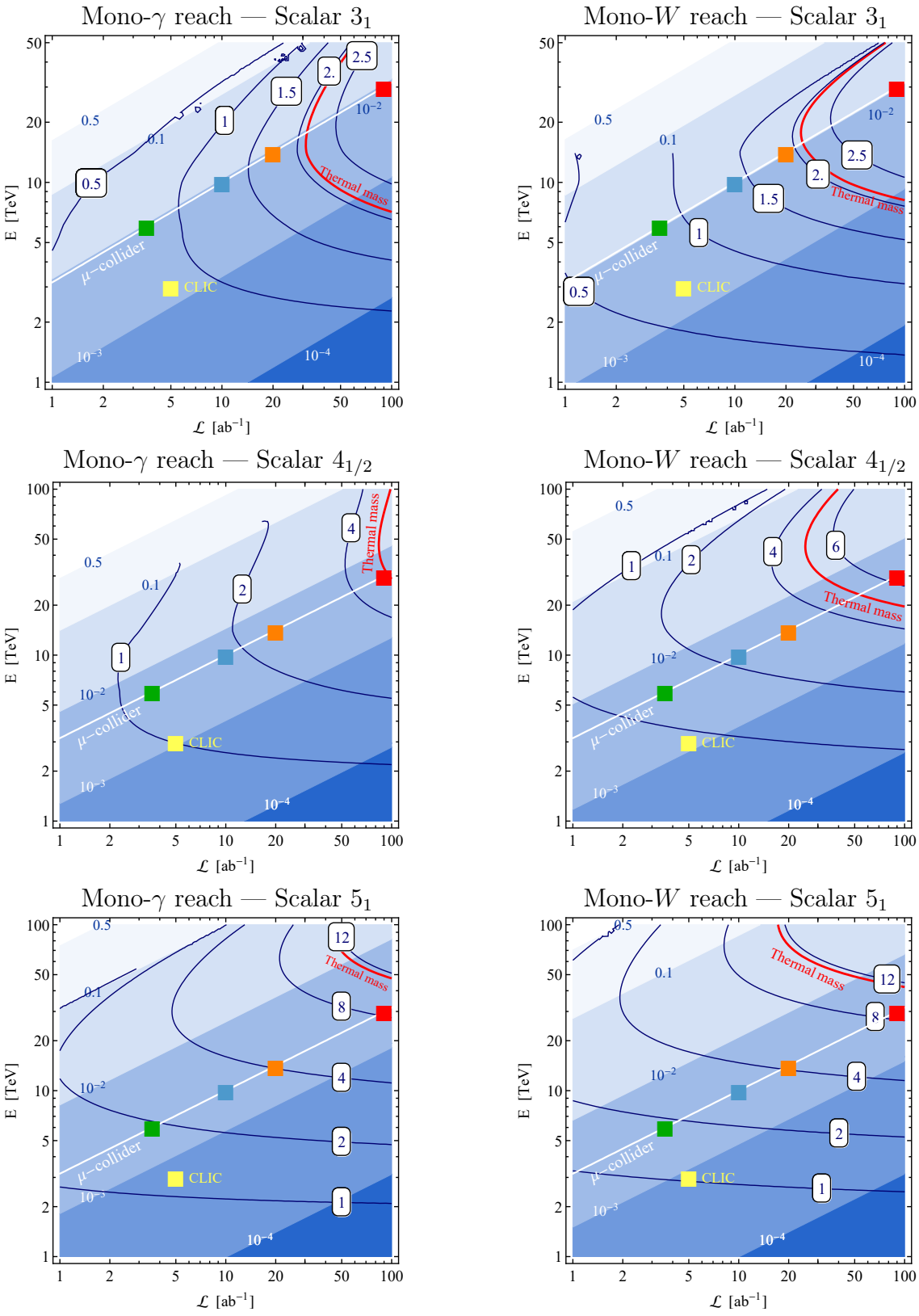

Figure F.6: *Same as Figs. 3.6 and 3.7 for the scalar* 3_1, $4_{1/2}$ *and* 5_1, *respectively.*

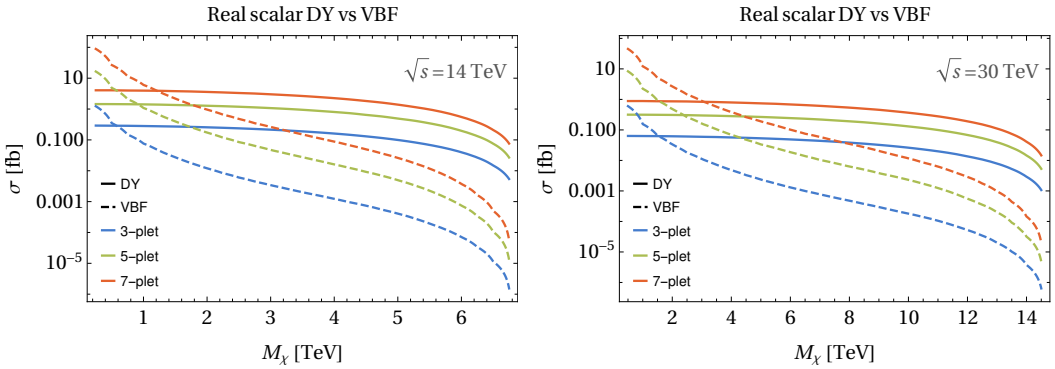

Figure F.7: *Drell-Yan and W-fusion $\chi\chi$ production as a function of M_χ.* **Left:** *Scalar 3-plet cross-section for $\sqrt{s} = 14\,\text{TeV}$.* **Right:** *Scalar 5-plet cross-section for $\sqrt{s} = 30\,\text{TeV}$.*

DY remains almost constant except near the kinematic threshold. In particular, for the real scalar 5-plet at $\sqrt{s} = 30$ TeV our DY 2σ reaches can be trusted, as the VBF contribution is smaller than 10% of the DY one. For the scalar triplet at $\sqrt{s} = 14$ TeV, the inclusion of VBF modes is not expected to improve the reach for masses $\gtrsim 1$ TeV.

It is remarkable that for real scalars the mass splitting between charged and neutral states in the n-plet is dominated by EW interactions. Indeed, no splitting term with the Higgs can be written at the quartic level, due to the antisymmetry of the SU(2) contraction. By hypercharge conservation, and assuming the scalar does not get any extra VEV, the leading terms contributing to the mass splitting are dimension 6 in the SM. Therefore the stub-track prediction is robust and does not depend on peculiar UV completions of the model. Results for searches of scalar WIMPs from stub-track analyses are reported in Fig. F.5.

Bibliography

[1] Planck Collaboration, N. Aghanim et al., *Planck 2018 results. VI. Cosmological parameters*, *Astron. Astrophys.* **641** (2020) A6 [1807.06209].

[2] N. Arkani-Hamed, A. G. Cohen and H. Georgi, *Electroweak symmetry breaking from dimensional deconstruction*, *Phys. Lett. B* **513** (2001) 232 [hep-ph/0105239].

[3] N. Arkani-Hamed, A. G. Cohen, T. Gregoire and J. G. Wacker, *Phenomenology of electroweak symmetry breaking from theory space*, *JHEP* **08** (2002) 020 [hep-ph/0202089].

[4] N. Arkani-Hamed, A. G. Cohen, E. Katz, A. E. Nelson, T. Gregoire and J. G. Wacker, *The Minimal moose for a little Higgs*, *JHEP* **08** (2002) 021 [hep-ph/0206020].

[5] N. Arkani-Hamed, A. G. Cohen, E. Katz and A. E. Nelson, *The Littlest Higgs*, *JHEP* **07** (2002) 034 [hep-ph/0206021].

[6] D. E. Kaplan and M. Schmaltz, *The Little Higgs from a simple group*, *JHEP* **10** (2003) 039 [hep-ph/0302049].

[7] M. Schmaltz, *Physics beyond the standard model (theory): Introducing the little Higgs*, *Nucl. Phys. B Proc. Suppl.* **117** (2003) 40 [hep-ph/0210415].

[8] S. Chang and J. G. Wacker, *Little Higgs and custodial SU(2)*, *Phys. Rev. D* **69** (2004) 035002 [hep-ph/0303001].

[9] M. Schmaltz and D. Tucker-Smith, *Little Higgs review*, *Ann. Rev. Nucl. Part. Sci.* **55** (2005) 229 [hep-ph/0502182].

[10] I. Low, *T parity and the littlest Higgs*, *JHEP* **10** (2004) 067 [hep-ph/0409025].

[11] J. Hubisz and P. Meade, *Phenomenology of the littlest Higgs with T-parity*, *Phys. Rev. D* **71** (2005) 035016 [hep-ph/0411264].

[12] J. Hubisz, P. Meade, A. Noble and M. Perelstein, *Electroweak precision constraints on the littlest Higgs model with T parity*, *JHEP* **01** (2006) 135 [hep-ph/0506042].

[13] H. Goldberg, *Constraint on the Photino Mass from Cosmology*, *Phys. Rev. Lett.* **50** (1983) 1419. [Erratum: Phys.Rev.Lett. 103, 099905 (2009)].

[14] J. R. Ellis, J. S. Hagelin, D. V. Nanopoulos, K. A. Olive and M. Srednicki, *Supersymmetric Relics from the Big Bang*, *Nucl. Phys. B* **238** (1984) 453.

[15] G. Jungman, M. Kamionkowski and K. Griest, *Supersymmetric dark matter*, *Phys. Rept.* **267** (1996) 195 [hep-ph/9506380].

[16] H.-C. Cheng, J. L. Feng and K. T. Matchev, *Kaluza-Klein dark matter*, *Phys. Rev. Lett.* **89** (2002) 211301 [hep-ph/0207125].

[17] G. Servant and T. M. P. Tait, *Is the lightest Kaluza-Klein particle a viable dark matter candidate?*, *Nucl. Phys. B* **650** (2003) 391 [hep-ph/0206071].

[18] Z. Chacko, H.-S. Goh and R. Harnik, *The Twin Higgs: Natural electroweak breaking from mirror symmetry*, *Phys. Rev. Lett.* **96** (2006) 231802 [hep-ph/0506256].

[19] Z. Chacko, H.-S. Goh and R. Harnik, *A Twin Higgs model from left-right symmetry*, *JHEP* **01** (2006) 108 [hep-ph/0512088].

[20] R. Barbieri, T. Gregoire and L. J. Hall, *Mirror world at the large hadron collider*, hep-ph/0509242.

[21] N. Craig and K. Howe, *Doubling down on naturalness with a supersymmetric twin Higgs*, *JHEP* **03** (2014) 140 [1312.1341].

[22] I. Garcia Garcia, R. Lasenby and J. March-Russell, *Twin Higgs WIMP Dark Matter*, *Phys. Rev. D* **92** (2015) 055034 [1505.07109].

[23] M. Cirelli, N. Fornengo and A. Strumia, *Minimal dark matter*, *Nucl. Phys. B* **753** (2006) 178 [hep-ph/0512090].

[24] M. Cirelli, A. Strumia and M. Tamburini, *Cosmology and Astrophysics of Minimal Dark Matter*, *Nucl. Phys. B* **787** (2007) 152 [0706.4071].

[25] M. Cirelli and A. Strumia, *Minimal Dark Matter: Model and results*, *New J. Phys.* **11** (2009) 105005 [0903.3381].

[26] A. Mitridate, M. Redi, J. Smirnov and A. Strumia, *Cosmological Implications of Dark Matter Bound States*, *JCAP* **05** (2017) 006 [1702.01141].

[27] L. Di Luzio, R. Gröber, J. F. Kamenik and M. Nardecchia, *Accidental matter at the LHC*, *JHEP* **07** (2015) 074 [1504.00359].

[28] K. Griest and M. Kamionkowski, *Unitarity Limits on the Mass and Radius of Dark Matter Particles*, *Phys. Rev. Lett.* **64** (1990) 615.

[29] B. Ostdiek, *Constraining the minimal dark matter fiveplet with LHC searches*, **92** (2015) 055008 [1506.03445].

[30] L. Di Luzio, R. Gröber and G. Panico, *Probing new electroweak states via precision measurements at the LHC and future colliders*, *JHEP* **01** (2019) 011 [1810.10993].

[31] J. Hisano, K. Ishiwata and N. Nagata, *QCD Effects on Direct Detection of Wino Dark Matter*, *JHEP* **06** (2015) 097 [1504.00915].

[32] J. Hisano, K. Ishiwata, N. Nagata and T. Takesako, *Direct Detection of Electroweak-Interacting Dark Matter*, *JHEP* **07** (2011) 005 [1104.0228].

[33] R. J. Hill and M. P. Solon, *WIMP-nucleon scattering with heavy WIMP effective theory*, *Phys. Rev. Lett.* **112** (2014) 211602 [1309.4092].

[34] M. Cirelli, T. Hambye, P. Panci, F. Sala and M. Taoso, *Gamma ray tests of Minimal Dark Matter*, *JCAP* **10** (2015) 026 [1507.05519].

[35] E. Del Nobile, M. Nardecchia and P. Panci, *Millicharge or Decay: A Critical Take on Minimal Dark Matter*, *JCAP* **04** (2016) 048 [1512.05353].

[36] J. Harz and K. Petraki, *Radiative bound-state formation in unbroken perturbative non-Abelian theories and implications for dark matter*, *JHEP* **07** (2018) 096 [1805.01200].

[37] B. von Harling and K. Petraki, *Bound-state formation for thermal relic dark matter and unitarity*, *JCAP* **12** (2014) 033 [1407.7874].

[38] J. P. Delahaye, M. Diemoz, K. Long, B. Mansoulié, N. Pastrone, L. Rivkin, D. Schulte, A. Skrinsky and A. Wulzer, *Muon Colliders*, 1901.06150.

[39] ALEGRO Collaboration, E. Adli et al., *Towards an Advanced Linear International Collider*, 1901.10370.

[40] M. Schumann, L. Baudis, L. Bütikofer, A. Kish and M. Selvi, *Dark matter sensitivity of multi-ton liquid xenon detectors*, *JCAP* **10** (2015) 016 [1506.08309].

[41] DARWIN Collaboration, J. Aalbers et al., *DARWIN: towards the ultimate dark matter detector*, *JCAP* **11** (2016) 017 [1606.07001].

[42] V. Lefranc, E. Moulin, P. Panci, F. Sala and J. Silk, *Dark Matter in γ lines: Galactic Center vs dwarf galaxies*, *JCAP* **09** (2016) 043 [1608.00786].

[43] CTA Collaboration, A. Acharyya et al., *Sensitivity of the Cherenkov Telescope Array to a dark matter signal from the Galactic centre*, *JCAP* **01** (2021) 057 [2007.16129].

[44] H. Silverwood, C. Weniger, P. Scott and G. Bertone, *A realistic assessment of the CTA sensitivity to dark matter annihilation*, *JCAP* **03** (2015) 055 [1408.4131].

[45] V. Lefranc, E. Moulin, P. Panci and J. Silk, *Prospects for Annihilating Dark Matter in the inner Galactic halo by the Cherenkov Telescope Array*, *Phys. Rev. D* **91** (2015) 122003 [1502.05064].

[46] A. Drukier and L. Stodolsky, *Principles and Applications of a Neutral Current Detector for Neutrino Physics and Astronomy*, *Phys. Rev. D* **30** (1984) 2295.

[47] P. F. Smith and J. D. Lewin, *COHERENT INTERACTION OF GALACTIC NEUTRINOS WITH MATERIAL TARGETS*, *Phys. Lett. B* **127** (1983) 185.

[48] M. W. Goodman and E. Witten, *Detectability of Certain Dark Matter Candidates*, *Phys. Rev. D* **31** (1985) 3059.

[49] A. K. Drukier, K. Freese and D. N. Spergel, *Detecting Cold Dark Matter Candidates*, *Phys. Rev. D* **33** (1986) 3495.

[50] J. Aalbers et al., *A Next-Generation Liquid Xenon Observatory for Dark Matter and Neutrino Physics*, 2203.02309.

[51] G. J. Alner et al., *First limits on WIMP nuclear recoil signals in ZEPLIN-II: A two phase xenon detector for dark matter detection*, *Astropart. Phys.* **28** (2007) 287 [astro-ph/0701858].

[52] XENON Collaboration, E. Aprile et al., *Dark Matter Search Results from a One Ton-Year Exposure of XENON1T*, *Phys. Rev. Lett.* **121** (2018) 111302 [1805.12562].

[53] PandaX Collaboration, Y. Meng et al., *Dark Matter Search Results from the PandaX-4T Commissioning Run*, 2107.13438.

[54] B. J. Mount et al., *LUX-ZEPLIN (LZ) Technical Design Report*, 1703.09144.

[55] XENON Collaboration, E. Aprile et al., *Projected WIMP sensitivity of the XENONnT dark matter experiment*, *JCAP* **11** (2020) 031 [2007.08796].

[56] J. Billard, L. Strigari and E. Figueroa-Feliciano, *Implication of neutrino backgrounds on the reach of next generation dark matter direct detection experiments*, *Phys. Rev. D* **89** (2014) 023524 [1307.5458].

[57] *High-Luminosity Large Hadron Collider (HL-LHC): Technical Design Report V. 0.1*, .

[58] FCC Collaboration, A. Abada et al., *FCC-ee: The Lepton Collider: Future Circular Collider Conceptual Design Report Volume 2*, *Eur. Phys. J. ST* **228** (2019) 261.

[59] CEPC Study Group Collaboration, *CEPC Conceptual Design Report: Volume 1 - Accelerator*, 1809.00285.

[60] P. Lebrun, L. Linssen, A. Lucaci-Timoce, D. Schulte, F. Simon, S. Stapnes, N. Toge, H. Weerts and J. Wells, *The CLIC Programme: Towards a Staged e+e- Linear Collider Exploring the Terascale : CLIC Conceptual Design Report*, 1209.2543.

[61] CLIC, CLICDP Collaboration, M. J. Boland et al., *Updated baseline for a staged Compact Linear Collider*, 1608.07537.

[62] *The International Linear Collider Technical Design Report - Volume 1: Executive Summary*, 1306.6327.

[63] *The International Linear Collider Technical Design Report - Volume 3.II: Accelerator Baseline Design*, 1306.6328.

[64] FCC Collaboration, A. Abada et al., *FCC-hh: The Hadron Collider: Future Circular Collider Conceptual Design Report Volume 3*, *Eur. Phys. J. ST* **228** (2019) 755.

[65] A. Costantini, F. De Lillo, F. Maltoni, L. Mantani, O. Mattelaer, R. Ruiz and X. Zhao, *Vector boson fusion at multi-TeV muon colliders*, *JHEP* **09** (2020) 080 [2005.10289].

[66] H. Al Ali et al., *The Muon Smasher's Guide*, 2103.14043.

[67] C. Aime et al., *Muon Collider Physics Summary*, 2203.07256.

[68] R. Capdevilla, F. Meloni, R. Simoniello and J. Zurita, *Hunting wino and higgsino dark matter at the muon collider with disappearing tracks*, 2102.11292.

[69] M. Cirelli, G. Corcella, A. Hektor, G. Hutsi, M. Kadastik, P. Panci, M. Raidal, F. Sala and A. Strumia, *PPPC 4 DM ID: A Poor Particle Physicist Cookbook for Dark Matter Indirect Detection*, *JCAP* **03** (2011) 051 [1012.4515]. [Erratum: JCAP 10, E01 (2012)].

[70] P. Picozza et al., *PAMELA: A Payload for Antimatter Matter Exploration and Light-nuclei Astrophysics*, *Astropart. Phys.* **27** (2007) 296 [astro-ph/0608697].

[71] AMS 02 Collaboration, R. Battiston, *The antimatter spectrometer (AMS-02): A particle physics detector in space*, *Nucl. Instrum. Meth. A* **588** (2008) 227.

[72] FERMI-LAT Collaboration, M. Ackermann et al., *Updated search for spectral lines from Galactic dark matter interactions with pass 8 data from the Fermi Large Area Telescope*, *Phys. Rev. D* **91** (2015) 122002 [1506.00013].

[73] HESS Collaboration, H. Abdalla et al., *Searches for gamma-ray lines and 'pure WIMP' spectra from Dark Matter annihilations in dwarf galaxies with H.E.S.S*, *JCAP* **11** (2018) 037 [1810.00995].

[74] J. Aleksić et al., *Performance of the MAGIC stereo system obtained with Crab Nebula data*, *Astroparticle Physics* **35** (2012) 435 [1108.1477].

[75] J. Holder et al., *Status of the VERITAS Observatory*, *AIP Conf. Proc.* **1085** (2009) 657 [0810.0474].

[76] L. Rinchiuso, N. L. Rodd, I. Moult, E. Moulin, M. Baumgart, T. Cohen, T. R. Slatyer, I. W. Stewart and V. Vaidya, *Hunting for Heavy Winos in the Galactic Center*, *Phys. Rev. D* **98** (2018) 123014 [1808.04388].

[77] V. Lefranc, G. A. Mamon and P. Panci, *Prospects for annihilating Dark Matter towards Milky Way's dwarf galaxies by the Cherenkov Telescope Array*, *JCAP* **09** (2016) 021 [1605.02793].

[78] P. Ullio and M. Valli, *A critical reassessment of particle Dark Matter limits from dwarf satellites*, *JCAP* **07** (2016) 025 [1603.07721].

[79] F. Iocco, M. Pato and G. Bertone, *Evidence for dark matter in the inner Milky Way*, *Nature Phys.* **11** (2015) 245 [1502.03821].

[80] C. Wegg, O. Gerhard and M. Portail, *MOA-II Galactic microlensing constraints: the inner Milky Way has a low dark matter fraction and a near maximal disc*, *mnras* **463** (2016) 557 [1607.06462].

[81] M. Pato, F. Iocco and G. Bertone, *Dynamical constraints on the dark matter distribution in the Milky Way*, *JCAP* **12** (2015) 001 [1504.06324].

[82] Y. Huang, X. W. Liu, H. B. Yuan, M. S. Xiang, H. W. Zhang, B. Q. Chen, J. J. Ren, C. Wang, Y. Zhang, Y. H. Hou, Y. F. Wang and Z. H. Cao, *The Milky Way's rotation curve out to 100 kpc and its constraint on the Galactic mass distribution*, *mnras* **463** (2016) 2623 [1604.01216].

[83] S. Bottaro, D. Buttazzo, M. Costa, R. Franceschini, P. Panci, D. Redigolo and L. Vittorio, *Closing the window on WIMP Dark Matter*, *Eur. Phys. J. C* **82** (2022) 31 [2107.09688].

[84] S. Bottaro, A. Strumia and N. Vignaroli, *Minimal Dark Matter bound states at future colliders*, *JHEP* **06** (2021) 143 [2103.12766].

[85] S. Bottaro, D. Buttazzo, M. Costa, R. Franceschini, P. Panci, D. Redigolo and L. Vittorio, *The last Complex WIMPs standing*, 2205.04486.

[86] T. Hambye, F. S. Ling, L. Lopez Honorez and J. Rocher, *Scalar Multiplet Dark Matter*, *JHEP* **07** (2009) 090 [0903.4010]. [Erratum: JHEP 05, 066 (2010)].

[87] J. Hisano, S. Matsumoto and M. M. Nojiri, *Explosive dark matter annihilation*, *Phys. Rev. Lett.* **92** (2004) 031303 [hep-ph/0307216].

[88] J. Hisano, S. Matsumoto, M. Nagai, O. Saito and M. Senami, *Non-perturbative effect on thermal relic abundance of dark matter*, *Phys. Lett. B* **646** (2007) 34 [hep-ph/0610249].

[89] N. Arkani-Hamed, D. P. Finkbeiner, T. R. Slatyer and N. Weiner, *A Theory of Dark Matter*, *Phys. Rev. D* **79** (2009) 015014 [0810.0713].

[90] S. Cassel, *Sommerfeld factor for arbitrary partial wave processes*, *J. Phys. G* **37** (2010) 105009 [0903.5307].

[91] M. Cirelli, P. Panci, K. Petraki, F. Sala and M. Taoso, *Dark Matter's secret liaisons: phenomenology of a dark U(1) sector with bound states*, *JCAP* **05** (2017) 036 [1612.07295].

[92] T. Han, Z. Liu, L.-T. Wang and X. Wang, *WIMPs at High Energy Muon Colliders*, *Phys. Rev. D* **103** (2021) 075004 [2009.11287].

[93] S. Bottaro, D. Buttazzo, M. Costa, R. Franceschini, P. Panci, D. Redigolo and L. Vittorio, *Indirect detection prospects for heavy WIMPs*, in preparation.

[94] T. Cohen, K. Murase, N. L. Rodd, B. R. Safdi and Y. Soreq, *γ -ray Constraints on Decaying Dark Matter and Implications for IceCube*, *Phys. Rev. Lett.* **119** (2017) 021102 [1612.05638].

[95] H.-C. Cheng, B. A. Dobrescu and K. T. Matchev, *Generic and chiral extensions of the supersymmetric standard model*, *Nucl. Phys. B* **543** (1999) 47 [hep-ph/9811316].

[96] J. L. Feng, T. Moroi, L. Randall, M. Strassler and S.-f. Su, *Discovering supersymmetry at the Tevatron in wino LSP scenarios*, *Phys. Rev. Lett.* **83** (1999) 1731 [hep-ph/9904250].

[97] T. Gherghetta, G. F. Giudice and J. D. Wells, *Phenomenological consequences of supersymmetry with anomaly induced masses*, *Nucl. Phys. B* **559** (1999) 27 [hep-ph/9904378].

[98] M. Ibe, S. Matsumoto and R. Sato, *Mass Splitting between Charged and Neutral Winos at Two-Loop Level*, *Phys. Lett. B* **721** (2013) 252 [1212.5989].

[99] J. McKay and P. Scott, *Two-loop mass splittings in electroweak multiplets: winos and minimal dark matter*, *Phys. Rev. D* **97** (2018) 055049 [1712.00968].

[100] M. Low and L.-T. Wang, *Neutralino dark matter at 14 TeV and 100 TeV*, *JHEP* **08** (2014) 161 [1404.0682].

[101] M. Cirelli, F. Sala and M. Taoso, *Wino-like Minimal Dark Matter and future colliders*, *JHEP* **10** (2014) 033 [1407.7058]. [Erratum: JHEP 01, 041 (2015)].

[102] T. Banks and N. Seiberg, *Symmetries and Strings in Field Theory and Gravity*, *Phys. Rev. D* **83** (2011) 084019 [1011.5120].

[103] B. Audren, J. Lesgourgues, G. Mangano, P. D. Serpico and T. Tram, *Strongest model-independent bound on the lifetime of Dark Matter*, *JCAP* **12** (2014) 028 [1407.2418].

[104] E. Aubourg et al., *Cosmological implications of baryon acoustic oscillation measurements*, *Phys. Rev. D* **92** (2015) 123516 [1411.1074].

[105] S. Ando and K. Ishiwata, *Constraints on decaying dark matter from the extragalactic gamma-ray background*, *JCAP* **05** (2015) 024 [1502.02007].

[106] M. Cirelli, E. Moulin, P. Panci, P. D. Serpico and A. Viana, *Gamma ray constraints on Decaying Dark Matter*, *Phys. Rev. D* **86** (2012) 083506 [1205.5283].

[107] J. Smirnov and J. F. Beacom, *TeV-Scale Thermal WIMPs: Unitarity and its Consequences*, *Phys. Rev. D* **100** (2019) 043029 [1904.11503].

[108] N. Cabibbo and R. Gatto, *Electron Positron Colliding Beam Experiments*, *Phys. Rev.* **124** (1961) 1577.

[109] N. Cabibbo, G. Karl and L. Wolfenstein, *A New Unitarity Bound on e+ e- Annihilation*, *Phys. Lett. B* **51** (1974) 387.

[110] L. D. Landau, *Quantum Mechanics: Non-Relativistic Theory*, vol. v.3 of *Course of Theoretical Physics*. Butterworth-Heinemann, Oxford, 1991.

[111] S. Bottaro and D. Redigolo, *The dark matter unitarity bound at NLO*, to appear.

[112] M. Beneke, R. Szafron and K. Urban, *Sommerfeld-corrected relic abundance of wino dark matter with NLO electroweak potentials*, *JHEP* **02** (2021) 020 [2009.00640].

[113] K. Urban, *NLO electroweak potentials for minimal dark matter and beyond*, *JHEP* **10** (2021) 136 [2108.07285].

[114] M. Low and L.-T. Wang, *Neutralino dark matter at 100 tev*, 1404.0682v1.

[115] European Strategy for Particle Physics Preparatory Group, *Physics Briefing Book*, 1910.11775v2. Physics Briefing Book - Input for the European Strategy for Particle Physics Update 2020.

[116] K. Harigaya, K. Ichikawa, A. Kundu, S. Matsumoto and S. Shirai, *Indirect probe of electroweak-interacting particles at future lepton colliders*, *Journal of High Energy Physics* **9** (2015) 105 [1504.03402].

[117] M. Boscolo, J.-P. Delahaye and M. Palmer, *The future prospects of muon colliders and neutrino factories*, *Rev. Accel. Sci. Tech.* **10** (2019) 189 [1808.01858].

[118] R. B. Palmer, *Muon colliders*, *Reviews of Accelerator Science and Technology* **07** (2014) 137.

[119] International Muon Collider Design Study.

[120] P. J. Fox, R. Harnik, J. Kopp and Y. Tsai, *LEP Shines Light on Dark Matter*, *Phys. Rev. D* **84** (2011) 014028 [1103.0240].

[121] C. Bartels, M. Berggren and J. List, *Characterising WIMPs at a future e^+e^- Linear Collider*, *Eur. Phys. J. C* **72** (2012) 2213 [1206.6639].

[122] J. de Blas et al., *The CLIC Potential for New Physics*, 1812.02093.

[123] J. Alwall, M. Herquet, F. Maltoni, O. Mattelaer and T. Stelzer, *MadGraph 5 : Going Beyond*, *JHEP* **06** (2011) 128 [1106.0522].

[124] J. Alwall, R. Frederix, S. Frixione, V. Hirschi, F. Maltoni, O. Mattelaer, H. S. Shao, T. Stelzer, P. Torrielli and M. Zaro, *The automated computation of tree-level and next-to-leading order differential cross sections, and their matching to parton shower simulations*, *JHEP* **07** (2014) 079 [1405.0301].

[125] U. Schnoor, *Long-lived particle reconstruction at clic*, *Linear Collider Workshop 2019* .

[126] Erica Brondolin, *Disappearing tracks at CLIC*, *LLP workshop 2020* .

[127] T. Katayose, S. Matsumoto and S. Shirai, *Non-perturbative Effects on Electroweakly Interacting Massive Particles at Hadron Collider*, *Phys. Rev. D* **103** (2021) 095017 [2011.14784].

[128] W. Shepherd, T. M. P. Tait and G. Zaharijas, *Bound states of weakly interacting dark matter*, *Phys. Rev. D* **79** (2009) 055022 [0901.2125].

[129] M. Greco, T. Han and Z. Liu, *ISR effects for resonant Higgs production at future lepton colliders*, *Phys. Lett. B* **763** (2016) 409 [1607.03210].

[130] S. Jadach, B. F. L. Ward and Z. Was, *Coherent exclusive exponentiation for precision Monte Carlo calculations*, *Phys. Rev. D* **63** (2001) 113009 [hep-ph/0006359].

[131] K. Hayashi, K. Ichikawa, S. Matsumoto, M. Ibe, M. N. Ishigaki and H. Sugai, *Dark matter annihilation and decay from non-spherical dark halos in galactic dwarf satellites*, *Mon. Not. Roy. Astron. Soc.* **461** (2016) 2914 [1603.08046].

[132] M. Baumgart, T. Cohen, I. Moult, N. L. Rodd, T. R. Slatyer, M. P. Solon, I. W. Stewart and V. Vaidya, *Resummed Photon Spectra for WIMP Annihilation*, *JHEP* **03** (2018) 117 [1712.07656].

[133] A. Hryczuk and R. Iengo, *The one-loop and Sommerfeld electroweak corrections to the Wino dark matter annihilation*, *JHEP* **01** (2012) 163 [1111.2916]. [Erratum: JHEP 06, 137 (2012)].

[134] G. Ovanesyan, T. R. Slatyer and I. W. Stewart, *Heavy Dark Matter Annihilation from Effective Field Theory*, *Phys. Rev. Lett.* **114** (2015) 211302 [1409.8294].

[135] M. Baumgart, I. Z. Rothstein and V. Vaidya, *Constraints on Galactic Wino Densities from Gamma Ray Lines*, *JHEP* **04** (2015) 106 [1412.8698].

[136] M. Baumgart and V. Vaidya, *Semi-inclusive wino and higgsino annihilation to LL'*, *JHEP* **03** (2016) 213 [1510.02470].

[137] G. Ovanesyan, N. L. Rodd, T. R. Slatyer and I. W. Stewart, *One-loop correction to heavy dark matter annihilation*, *Phys. Rev. D* **95** (2017) 055001 [1612.04814]. [Erratum: Phys.Rev.D 100, 119901 (2019)].

[138] HESS Collaboration, H. Abdalla et al., *Searches for gamma-ray lines and 'pure WIMP' spectra from Dark Matter annihilations in dwarf galaxies with H.E.S.S*, *JCAP* **11** (2018) 037 [1810.00995].

[139] C. Garcia-Cely, A. Ibarra, A. S. Lamperstorfer and M. H. G. Tytgat, *Gamma-rays from Heavy Minimal Dark Matter*, *JCAP* **10** (2015) 058 [1507.05536].

[140] R. Mahbubani, M. Redi and A. Tesi, *Indirect detection of composite asymmetric dark matter*, *Phys. Rev. D* **101** (2020) 103037 [1908.00538].

[141] J. Hisano, S. Matsumoto, M. M. Nojiri and O. Saito, *Direct detection of the Wino and Higgsino-like neutralino dark matters at one-loop level*, *Phys. Rev. D* **71** (2005) 015007 [hep-ph/0407168].

[142] J. Hisano, K. Ishiwata and N. Nagata, *A complete calculation for direct detection of Wino dark matter*, *Phys. Lett. B* **690** (2010) 311 [1004.4090].

[143] M. Cirelli, E. Del Nobile and P. Panci, *Tools for model-independent bounds in direct dark matter searches*, *JCAP* **10** (2013) 019 [1307.5955].

[144] Flavour Lattice Averaging Group Collaboration, S. Aoki et al., *FLAG Review 2019: Flavour Lattice Averaging Group (FLAG)*, *Eur. Phys. J. C* **80** (2020) 113 [1902.08191].

[145] C. Alexandrou, V. Drach, K. Jansen, C. Kallidonis and G. Koutsou, *Baryon spectrum with $N_f = 2 + 1 + 1$ twisted mass fermions*, *Phys. Rev. D* **90** (2014) 074501 [1406.4310].

[146] MILC Collaboration, W. Freeman and D. Toussaint, *Intrinsic strangeness and charm of the nucleon using improved staggered fermions*, *Phys. Rev. D* **88** (2013) 054503 [1204.3866].

[147] T. Katayose, S. Matsumoto, S. Shirai and Y. Watanabe, *Thermal Real Scalar Triplet Dark Matter*, 2105.07650.

[148] J. Bramante, P. J. Fox, G. D. Kribs and A. Martin, *Inelastic frontier: Discovering dark matter at high recoil energy*, *Phys. Rev. D* **94** (2016) 115026 [1608.02662].

[149] N. Song, S. Nagorny and A. C. Vincent, *Pushing the frontier of WIMPy inelastic dark matter: Journey to the end of the periodic table*, *Phys. Rev. D* **104** (2021) 103032 [2104.09517].

[150] C. A. J. O'Hare, *New Definition of the Neutrino Floor for Direct Dark Matter Searches*, *Phys. Rev. Lett.* **127** (2021) 251802 [2109.03116].

[151] Jindariani, Sergo et al., *Promising Technologies and R&D Directions for the Future Muon Collider Detectors*, 2203.07224v1.

[152] XENON Collaboration, E. Aprile et al., *Dark Matter Search Results from a One Ton-Year Exposure of XENON1T*, *Phys. Rev. Lett.* **121** (2018) 111302 [1805.12562].

[153] PICO Collaboration, C. Amole et al., *Dark matter search results from the PICO-60 CF_3I bubble chamber*, *Phys. Rev. D* **93** (2016) 052014 [1510.07754].

[154] CRESST Collaboration, G. Angloher et al., *Results on light dark matter particles with a low-threshold CRESST-II detector*, *Eur. Phys. J. C* **76** (2016) 25 [1509.01515].

[155] A. Münster et al., *Radiopurity of CaWO4 crystals for direct dark matter search with CRESST and EURECA*, *JCAP* **05** (2014) 018 [1403.5114].

[156] J. W. Beeman et al., *New experimental limits on the alpha decays of lead isotopes*, *Eur. Phys. J. A* **49** (2013) 50 [1212.2422].

[157] B. Lehnert, H. Ramani, M. Hult, G. Lutter, M. Pospelov, S. Rajendran and K. Zuber, *Search for Dark Matter Induced Deexcitation of $^{180}Ta^{m}$*, *Phys. Rev. Lett.* **124** (2020) 181802 [1911.07865].

[158] B. Broerman, M. Laubenstein, S. Nagorny, N. Song and A. C. Vincent, *A search for rare and induced nuclear decays in hafnium*, *Nucl. Phys. A* **1012** (2021) 122212 [2012.08339].

[159] P. Belli et al., *Search for α decay of naturally occurring osmium nuclides accompanied by γ quanta*, *Phys. Rev. C* **102** (2020) 024605 [2009.01508].

[160] H. E. Haber and D. Wyler, *RADIATIVE NEUTRALINO DECAY*, *Nucl. Phys. B* **323** (1989) 267.

[161] T. Binder, A. Filimonova, K. Petraki and G. White, *Saha equilibrium for metastable bound states and dark matter freeze-out*, 2112.00042.

[162] CMS Collaboration, V. Khachatryan et al., *Search for long-lived charged particles in proton-proton collisions at $\sqrt{s} = 13$ TeV*, *Phys. Rev. D* **94** (2016) 112004 [1609.08382].

[163] ATLAS Collaboration, M. Aaboud et al., *Search for heavy charged long-lived particles in the ATLAS detector in 36.1 fb^{-1} of proton-proton collision data at $\sqrt{s} = 13$ TeV*, *Phys. Rev. D* **99** (2019) 092007 [1902.01636].

[164] G. Arcadi, A. Djouadi and M. Raidal, *Dark Matter through the Higgs portal*, *Phys. Rept.* **842** (2020) 1 [1903.03616].

[165] M. Farina, G. Panico, D. Pappadopulo, J. T. Ruderman, R. Torre and A. Wulzer, *Energy helps accuracy: electroweak precision tests at hadron colliders*, *Phys. Lett. B* **772** (2017) 210 [1609.08157].

[166] M. E. Peskin and T. Takeuchi, *Estimation of oblique electroweak corrections*, *Phys. Rev. D* **46** (1992) 381.

[167] R. Barbieri, A. Pomarol, R. Rattazzi and A. Strumia, *Electroweak symmetry breaking after LEP-1 and LEP-2*, *Nucl. Phys. B* **703** (2004) 127 [hep-ph/0405040].

[168] CMS Collaboration, A. Tumasyan et al., *Search for new physics in the lepton plus missing transverse momentum final state in proton-proton collisions at* $\sqrt{s}$ *= 13 TeV*, 2202.06075.

[169] A. Strumia, *Interpreting electroweak precision data including the W-mass CDF anomaly*, 2204.04191.

[170] S. Chen, A. Glioti, R. Rattazzi, L. Ricci and A. Wulzer, *Learning from Radiation at a Very High Energy Lepton Collider*, 2202.10509.

[171] R. Franceschini and X. Zhao, *In preparation*, .

[172] L. Lavoura and L.-F. Li, *Making the small oblique parameters large*, *Phys. Rev. D* **49** (1994) 1409 [hep-ph/9309262].

[173] J. Fan, M. Reece and L.-T. Wang, *Possible Futures of Electroweak Precision: ILC, FCC-ee, and CEPC*, *JHEP* **09** (2015) 196 [1411.1054].

[174] D. Buttazzo, R. Franceschini and A. Wulzer, *Two Paths Towards Precision at a Very High Energy Lepton Collider*, *JHEP* **05** (2021) 219 [2012.11555].

[175] CDF Collaboration, T. Aaltonen et al., *High-precision measurement of the W boson mass with the CDF II detector*, *Science* **376** (2022) 170.

[176] G. Panico, A. Pomarol and M. Riembau, *EFT approach to the electron Electric Dipole Moment at the two-loop level*, *JHEP* **04** (2019) 090 [1810.09413].

[177] C. Cesarotti, Q. Lu, Y. Nakai, A. Parikh and M. Reece, *Interpreting the Electron EDM Constraint*, *JHEP* **05** (2019) 059 [1810.07736].

[178] ACME Collaboration, V. Andreev et al., *Improved limit on the electric dipole moment of the electron*, *Nature* **562** (2018) 355.

[179] R. Alarcon et al., *Electric dipole moments and the search for new physics*, in *2022 Snowmass Summer Study*, 3, 2022, 2203.08103.

[180] Y. Cui, L. Randall and B. Shuve, *A WIMPy Baryogenesis Miracle*, *JHEP* **04** (2012) 075 [1112.2704].

[181] Y. Cui, *A Review of WIMP Baryogenesis Mechanisms*, *Mod. Phys. Lett. A* **30** (2015) 1530028 [1510.04298].

[182] L. Rinchiuso, O. Macias, E. Moulin, N. L. Rodd and T. R. Slatyer, *Prospects for detecting heavy WIMP dark matter with the Cherenkov Telescope Array: The Wino and Higgsino*, *Phys. Rev. D* **103** (2021) 023011 [2008.00692].

[183] M. Baryakhtar, J. Bramante, S. W. Li, T. Linden and N. Raj, *Dark Kinetic Heating of Neutron Stars and An Infrared Window On WIMPs, SIMPs, and Pure Higgsinos*, *Phys. Rev. Lett.* **119** (2017) 131801 [1704.01577].

[184] N. F. Bell, G. Busoni, S. Robles and M. Virgato, *Improved Treatment of Dark Matter Capture in Neutron Stars*, *JCAP* **09** (2020) 028 [2004.14888].

[185] N. F. Bell, G. Busoni, M. E. Ramirez-Quezada, S. Robles and M. Virgato, *Improved treatment of dark matter capture in white dwarfs*, *JCAP* **10** (2021) 083 [2104.14367].

[186] J. P. Gardner et al., *The James Webb Space Telescope*, *Space Sci. Rev.* **123** (2006) 485 [astro-ph/0606175].

[187] R. Krall and M. Reece, *Last Electroweak WIMP Standing: Pseudo-Dirac Higgsino Status and Compact Stars as Future Probes*, *Chin. Phys. C* **42** (2018) 043105 [1705.04843].

[188] T. Han, Y. Ma and K. Xie, *High energy leptonic collisions and electroweak parton distribution functions*, *Phys. Rev. D* **103** (2021) L031301 [2007.14300].

[189] Y. Kats and M. D. Schwartz, *Annihilation decays of bound states at the LHC*, *JHEP* **04** (2010) 016 [0912.0526].

[190] R. Mahbubani, M. Redi and A. Tesi, *Dark Nucleosynthesis: Cross-sections and Astrophysical Signals*, *JCAP* **02** (2021) 039 [2007.07231].

[191] M. Cirelli, E. Del Nobile and P. Panci, *Tools for model-independent bounds in direct dark matter searches*, *JCAP* **10** (2013) 019 [1307.5955].

[192] M. Freytsis and Z. Ligeti, *On dark matter models with uniquely spin-dependent detection possibilities*, *Phys. Rev. D* **83** (2011) 115009 [1012.5317].